RECENT ADVANCES IN PROMOTERS FOR GAS HYDRATE FORMATION

EDITED BY: Fei Wang, Amadeu K. Sum, Bei Liu and Nicolas Von Solms
PUBLISHED IN: Frontiers in Chemistry

frontiers Research Topics

ISSN 1664-8714
ISBN 978-2-88971-132-1
DOI 10.3389/978-2-88971-132-1

About Frontiers

Frontiers is more than just an open-access publisher of scholarly articles: it is a pioneering approach to the world of academia, radically improving the way scholarly research is managed. The grand vision of Frontiers is a world where all people have an equal opportunity to seek, share and generate knowledge. Frontiers provides immediate and permanent online open access to all its publications, but this alone is not enough to realize our grand goals.

Frontiers Journal Series

The Frontiers Journal Series is a multi-tier and interdisciplinary set of open-access, online journals, promising a paradigm shift from the current review, selection and dissemination processes in academic publishing. All Frontiers journals are driven by researchers for researchers; therefore, they constitute a service to the scholarly community. At the same time, the Frontiers Journal Series operates on a revolutionary invention, the tiered publishing system, initially addressing specific communities of scholars, and gradually climbing up to broader public understanding, thus serving the interests of the lay society, too.

Dedication to Quality

Each Frontiers article is a landmark of the highest quality, thanks to genuinely collaborative interactions between authors and review editors, who include some of the world's best academicians. Research must be certified by peers before entering a stream of knowledge that may eventually reach the public - and shape society; therefore, Frontiers only applies the most rigorous and unbiased reviews.
Frontiers revolutionizes research publishing by freely delivering the most outstanding research, evaluated with no bias from both the academic and social point of view. By applying the most advanced information technologies, Frontiers is catapulting scholarly publishing into a new generation.

What are Frontiers Research Topics?

Frontiers Research Topics are very popular trademarks of the Frontiers Journals Series: they are collections of at least ten articles, all centered on a particular subject. With their unique mix of varied contributions from Original Research to Review Articles, Frontiers Research Topics unify the most influential researchers, the latest key findings and historical advances in a hot research area! Find out more on how to host your own Frontiers Research Topic or contribute to one as an author by contacting the Frontiers Editorial Office: frontiersin.org/about/contact

RECENT ADVANCES IN PROMOTERS FOR GAS HYDRATE FORMATION

Topic Editors:
Fei Wang, Qingdao University of Science and Technology, China
Amadeu K. Sum, Colorado School of Mines, United States
Bei Liu, China University of Petroleum, China
Nicolas Von Solms, Technical University of Denmark, Denmark

Citation: Wang, F., Sum, A. K., Liu, B., Von Solms N., eds. (2021). Recent Advances in Promoters for Gas Hydrate Formation. Lausanne: Frontiers Media SA.
doi: 10.3389/978-2-88971-132-1

Table of Contents

frontiers in Chemistry

EDITORIAL
published: 04 June 2021
doi: 10.3389/fchem.2021.708269

Editorial: Recent Advances in Promoters for Gas Hydrate Formation

Fei Wang[1]*, *Amadeu K. Sum*[2] *and Bei Liu*[3]

[1]Qingdao University of Science and Technology, Qingdao, China, [2]Colorado School of Mines, Golden, CO, United States, [3]China University of Petroleum, Beijing, China

Keywords: gas hydrates, promoters, kinetics, thermodynamics, carbon material

Editorial on the Research Topic

Recent Advances in Promoters for Gas Hydrate Formation

Gas hydrates have been endowed with great potential in gas storage & transportation (e.g. methane and hydrogen), gas separation (e.g. CO_2 capture), desalination, cold and thermal energy storage, etc. Achieving the rapid hydrate formation is critical for utilizing the hydrate technology, which has been being the research focus since the proposition of this technology. During the past 2 decades, using additives to promote hydrate formation has been confirmed as an efficient method to push forward the application of hydrate technology, usually consisting of kinetic promoters (e.g. surfactants and nanofluids) and thermodynamic promoters (e.g. cyclopentane and tetrahydrofuran). However, more work is necessary to finally bring the hydrate technology from lab-scale to industrial application due to the defects of the current promoters, such as, the foam generation caused by surfactants, the poor stability of nanofluids, etc. On this account, the current research topic is focused on gas hydrate promoters, including both the summaries on the current promoters and the up to date development on novel promoters.

This research topic contains four mini review and five original research articles, covering both kinetic and thermodynamic promoters. Carbon-based materials, including activated carbon, graphite, graphene, carbon nanotube, etc., have been successfully adopted as kinetic promoters for gas hydrate formation. In the mini review by Song et al., the promotion efficiency of above-mentioned materials to gas hydrate formation was summarized and evaluated, in which, the carbon-based materials were applied as three types: porous carbon materials as packed beds, carbon-based particles in suspensions, and carbon-based nanoparticles in nanofluids. Based on the evaluation, porous packed bed (e.g. activated carbon) could promote gas hydrate formation by providing a large gas/liquid interface, and particles in suspension (e.g. activated carbon and carbon nanotubes) and nanofluids (e.g. water-soluble oxidized carbon nanotubes) could contribute to heat and mass transfer during hydrate formation. Among the common carbon-based materials, graphene is the one with the most attention in various fields. In the mini review by Sun et al., graphene-based materials adopted as suspension or nanofluids for promoting gas hydrate formation were specially summarized, including graphene, oxidized/sulfonated graphene, surfactant-stabilized graphene, and graphene-carried metal nanoparticles. No matter which form graphene was used, the hydrate nucleation could be promoted by the presence of numerous nucleation sites and the heat transfer during hydrate formation could be enhanced by the high thermal conductivity of graphene. Activated carbon, due to the abundant pore structures, has also been widely used in promoting gas hydrate formation. Zhang et al., chose activated carbon as the research object and summarized the promotion mechanism of activated carbon as porous packed bed to gas hydrate formation, in which, the hydrate nucleation sites provided by the microbulges on activated carbon surface and the two-way convection of water and methane in micropores of activated carbon were considered as the main reasons of the high hydrate nucleation and growth kinetics. Chen et al.used another porous material, ZIF-8 (2-methylimidazole

Edited and reviewed by:
Moyuan Cao,
Tianjin University, China

***Correspondence:**
Fei Wang
elliot_wang@qust.edu.cn

Specialty section:
This article was submitted to Physical Chemistry and Chemical Physics, a section of the journal Frontiers in Chemistry

Received: *11 May 2021*
Accepted: *26 May 2021*
Published: *04 June 2021*

Citation:
Wang F, Sum AK and Liu B (2021) Editorial: Recent Advances in Promoters for Gas Hydrate Formation. Front. Chem. 9:708269. doi: 10.3389/fchem.2021.708269

zinc salt), as both slurry and packed bed for methane hydrate formation and proposed the adsorption-hydration sequence method for high-efficiency methane storage with ZIF-8 slurry as the medium. Moreover, with the increasing severity of environmental problems, environment-friendly materials for gas hydrate formation have attracted more and more attention. Zhang et al. contributed the mini review containing the biomaterials that have been reported with efficient promotion to gas hydrate formation, such as, lignosulfonates, amino acids, biosurfactants, and biological porous structures, among which, amino acids, with the high species diversity, attracted the most attention and exhibited the best prospects. Besides the studies with chemicals as kinetic promoters as mentioned above, Uchida et al. reported the propane hydrate formation with nanobubble-containing water and we can also view it as using nanobubbles as kinetic promoters, which was approved as a novel technology to kinetically enhance hydrate formation.

Besides kinetic promoters, thermodynamic accelerating agents are also focused in this research topic. Miyamoto et al., with the aim of using hydrates as phase change materials for thermal storage, adopted tetrabutylphosphonium oxalate (TBPOx) as the hydrate former for semiclathrate hydrate formation and determined the phase equilibrium temperature and the dissociation heat, via which, TBPOx were confirmed as an excellent hydrate former for hydrate-based thermal storage. Seol et al. introduced three large guest molecules, oxabicyclic compounds, as the thermodynamic promoters for methane hydrate formation. Via spectroscopic investigation and equilibrium measurements, the authors declared the great potential of the three large guest molecules as alternates to conventional promoters. Nguyen et al. reported the hydrogen hydrate formation supported by both tetrahydrofuran (THF) and perchloric acid ($HClO_4$), and found that the co-inclusion of $HClO_4$ into the THF hydrates efficiently enhanced the insertion of hydrogen molecules into the hydrate cages, producing great application potential in hydrate-based hydrogen storage.

AUTHOR CONTRIBUTIONS

FW contributed to the writing of the main text. All authors revised and approved the Editorial.

Conflict of Interest: The authors declare that the research was conducted in the absence of any commercial or financial relationships that could be construed as a potential conflict of interest.

frontiers in Chemistry

ORIGINAL RESEARCH
published: 21 April 2020
doi: 10.3389/fchem.2020.00294

Adsorption-Hydration Sequence Method for Methane Storage in Porous Material Slurry

Jun-Li Chen, Peng Xiao, De-Xin Zhang, Guang-Jin Chen*, Chang-Yu Sun, Qing-Lan Ma, Ming-Ke Yang and En-Bao Zou*

State Key Laboratory of Heavy Oil Processing, China University of Petroleum, Beijing, China

Porous materials are deemed to be capable for promoting hydrate formation, while for the purpose of hydrate-based gas storage, those systems containing porous materials often cannot meet the requirement of high storage density. To increase the storage density, an adsorption-hydration sequence method was designed and systematically examined in this study. Methane storage and release in ZIF-8 slurries and fixed beds were investigated. The ZIF-8 retained 98.62%, while the activated carbon lost 62.17% of their adsorption capacities in slurry. In ZIF-8 fixed beds, methane storage density of 127.41 V/V_{bed} was acquired, while the gas loss during depressurization accounted for 21.50% of the gas uptake. In the ZIF-8 slurry, the storage density was effectively increased with the adsorption-hydration sequence method, and the gas loss during depressurization was much smaller than that in fixed beds. In the slurry, the gas uptake and gas loss decreased with the decrease of the chilling temperature. The largest gas uptake and storage density of 78.84 mmol and 133.59 V/V_{bed} were acquired in the slurry with ZIF-8 content of 40 wt.% at 268.15 K, meanwhile, the gas loss just accounted for 14.04% of the gas uptake. Self-preservation effect was observed in the slurry, and the temperature for the slowest gas release was found to be 263.15 K, while the release ratio at 10 h reached to 43.42%. By increasing the back pressure, the gas release rate could be effectively controlled. The gas release ratio at 1.1 MPa at 10 h was just 11.08%. The results showed that the application of adsorption-hydration sequence method in ZIF-8 slurry is a prospective manner for gas transportation.

Keywords: methane hydrate, formation improvement, ZIF-8, slurry, gas storage

OPEN ACCESS

Edited by:
Fei Wang,
Qingdao University of Science and Technology, China

Reviewed by:
Jiafei Zhao,
Dalian University of Technology, China
Sugata Chowdhury,
National Institute of Standards and Technology (NIST), United States

****Correspondence:***
Peng Xiao
xpmail@yeah.net
Guang-Jin Chen
gjchen@cup.edu.cn

Specialty section:
This article was submitted to Physical Chemistry and Chemical Physics, a section of the journal Frontiers in Chemistry

Received: *27 December 2019*
Accepted: *25 March 2020*
Published: *21 April 2020*

Citation:
Chen J-L, Xiao P, Zhang D-X, Chen G-J, Sun C-Y, Ma Q-L, Yang M-K and Zou E-B (2020) Adsorption-Hydration Sequence Method for Methane Storage in Porous Material Slurry. Front. Chem. 8:294. doi: 10.3389/fchem.2020.00294

INTRODUCTION

Gas hydrates are non-stoichiometric crystalline compounds formed when gas molecules with suitable size are trapped in polyhedral cavities of hydrogen-bonded water molecules under low temperature and high pressure. Natural gas hydrate extensively exists in the permafrost and the marine sediments and it is considered the largest hydrocarbon resource on earth. Gas hydrates are also being studied as alternative methods for industrial gas separation and carbon capture (Xu et al., 2012; Cai et al., 2017), water purification (Song et al., 2016; He et al., 2018; Dong et al., 2019), cold storage (Dufour et al., 2017) and food industry (Li et al., 2015). Meanwhile, because of its large gas storage capacity (up to 180 volume of gas per volume of hydrate) (Sloan, 2003), nonexplosive nature and mild storage condition (−5°C at 1 atm) (Stern et al., 2001), gas hydrate is also a potential

way to transport natural gas. For the small gas fields and sporadic transportation, transporting natural gas via hydrate is superior to LNG and pipeline because of the investment flexibility, and it could displace the CNG because of its safety. However, there exists two impediments in the practical application of hydrate-based gas transportation: the slow formation kinetics and the low storage capacity.

In order to solve these two fundamental problems, chemical methods of adding kinetic (Zhong and Rogers, 2000; Wang et al., 2015) or thermodynamic additives (Kim et al., 2015; Liao et al., 2015) and physical methods including stirring (Hao et al., 2007; Veluswamy et al., 2017), bubbling (Luo et al., 2007; Lv et al., 2012), spraying (Fukumoto et al., 2001; Fujita et al., 2009) have been studied, and the hydrate formation could be accelerated by these methods to varying degrees. However, some drawbacks hinder the practical application of these methods: the typical kinetic additive, sodium dodecyl sulfate (SDS), triggers the capillary effect so that give fast formation kinetics (Gayet et al., 2005), at the same time, it leads to climbing wall growth and porous morphology (Zhong and Rogers, 2000; Gayet et al., 2005; Mandal and Laik, 2008), which would remarkably reduce the apparent storage density of the hydrate; the thermodynamic additives occupy some cages of hydrate (Kim et al., 2015), decreasing the theoretical storage capacity; for physical methods, the viscosity increase accompanied by aggregation of hydrate particles results in high energy consumption of stirring (Fidel-Dufour et al., 2006; Mori, 2015); the hard-to-broken hydrate shells occupy the gas space, hindering the further formation in bubbling column (Luo et al., 2007); the heat transfer restricts the formation rate in spraying reactor (Matsuda et al., 2006).

Porous materials also have been used for improving hydrate formation. The typical application includes forming fixed bed and particle suspension. In water-contained fixed bed, the extensive contact area on packing material intensifies the hydrate formation. Porous media including silica sand (Linga et al., 2012; Babu et al., 2013; Yang et al., 2016), silica gel (Dicharry et al., 2013; Kumar et al., 2015), glass beads (Yang et al., 2015) have been proved to be effective in improving hydrate formation. Linga et al. (2012) studied methane hydrate formation in a fixed bed filled with sand and found that the hydrate formation was much faster than that in a stirred reactor, and the gas uptake reached to 193.13 V/V_{water}. Some research revealed that porous materials including activated carbon (Yan et al., 2005; Zhou et al., 2005; Siangsai et al., 2015) and MOFs (Mu et al., 2012; Casco et al., 2016) also have significant effect on hydrate formation. Babu et al. (2013) studied the morphology of methane hydrate formation in activated carbon. The hydrate formed in the interstitial pore space between the particles, thus, they concluded that the pore space plays an important role in hydrate formation. Porous materials could promote hydrate formation, in turn, hydrate formation could increase the gas storage capacity of the fixed bed. Zhou et al. (2005) found that the sorption amount of methane on wet activated carbon increased with the increase of water content, and when the water content $R_w = 2.92$, the sorption amount was 3.75 times higher than that on dry carbon because of the hydrate formation. Similarly, Yan et al. (2005) acquired a gas uptake of 140 V/V_{bed} in moist carbon. Mu et al. (2012) suggested that by adding some water in ZIF-8 fixed bed, the storage capacity could be raised by more than 56%. All of these fixed beds are in favor of hydrate formation, however, from the perspective of gas transportation, a contradiction exists between the hydrate formation and storage density. Generally, hydrate formation is well promoted only when water content is small. Chari et al. (2013a) measured the storage capacity of a silica-water system with water content from 20 to 1 g/g_{silica}, and found that the methane conversion monotonically increased from 6.14 to 67.82%, which suggested that the small water content is in favor of hydrate formation. However, the small water content could result three problems: (1) the gas fixed on porous materials by Van Der Waals force is easy to desorb during depressurization; (2) a large amount of porous media in fixed bed increases the apparent volume, so that decreases the storage density; (3) the scattered and small hydrate particles are easy to dissociate (Takeya et al., 2005). Therefore, to increase the feasibility of gas storage and transportation via hydrate formation in fixed bed, the water content needs to be increased. However, increasing water content would cause some problems.

Some studies suggest that in water dominated systems like suspension and slurry, solid particles have certain positive effects on hydrate formation. Zhou et al. (2014) found that by adding 0.4% graphite nanoparticle into the water, the induction time of CO_2 hydrate decreased by 80.8% and the CO_2 consumption increased by 12.8%. Kim et al. (2011) indicated that the multi-walled carbon nanotubes could accelerate hydrate formation. Pasieka et al. (2013) found that both the hydrophobic and hydrophilic multi-wall carbon nanotubes enhanced the hydrate formation. Similarly, porous materials also promote hydrate formation in suspension. Govindaraj et al. (2015) compared the effects of activated carbon and nano-silica on methane hydrate formation in suspension, and concluded that the effect of activated carbon is more pronounced. Wang et al. (2012) found that 0.01% ZIF-61 could accelerate the nucleation of tetrahydrofuran hydrate. Casco et al. (2016) compared the effects of MOFs with hydrophobic nature (ZIF-8) and hydrophilic nature [MIL-100(Fe)] on methane hydrate formation, and they found that the ZIF-8 caused a higher hydrate yield.

Hydrate formation in these suspensions could be enhanced in some extent, however, the solid particles mainly act as the nucleation center. In the process of transition from fixed bed to suspension by increasing water content, once the water content exceeds a certain value, the storage capacity of the fixed bed decreases rapidly (Yan et al., 2005), resulting low gas storage capacity in suspension. The highest storage capacity in the suspension of multi-walled carbon nanotubes was about 11.94 V/V_w at 10 h in Kim et al. (2011) work. The average water conversion was only 19.3% after 24 h in Govindaraj et al. (2015) study. Thus, simply increasing the water content could not resolve the contradiction between hydrate formation and storage density.

Besides the hydrate formation kinetics and gas storage density, hydrate dissociation is also a key factor to assess if the system is suitable for gas storage and transportation. Generally, hydrate dissociation rate decreases with the increase of pressure (Circone et al., 2004), while it does not simply decreases with the decrease

of temperature because of the self-preservation effect (Stern et al., 2003), which could create a trough on the curve of dissociation rate near the ice point, and it is considered to be the basis of hydrate transportation. Hydrate dissociation also relates to other factors. Takeya et al. (2005) indicated that larger hydrate particles are in favor of decreasing hydrate dissociation. Liang et al. (2005) found that about 6% of hydrate dissociated in 10 h at 267.4 K and the presence of activated carbon increased the dissociation. Compared with the pure water, additive like SDS (Lin et al., 2004), treated nano-particles (Wang et al., 2016), Salt (Mimachi et al., 2016) also would increase the dissociation rate.

In order to resolve the contradiction between the hydrate formation and the gas storage density, some attempts have been made in our previous study (Xiao et al., 2019), and both the hydrate formation and storage density were improved in the fixed bed with high water content. However, the highest storage density was only 111.75 V/V_{bed}, and the gas release was too fast for gas transportation. In the current study, we are trying to find a manner to promote hydrate formation in slurry, so that to acquire high gas storage density and slow gas release rate simultaneously.

EXPERIMENTAL SECTION

Material

Methane with a purity of 99.99% was supplied by Beijing Haipu Gas Co., Ltd. Double distilled water was prepared in our laboratory. ZIF-8 was synthesized in our laboratory. Activated carbon with particle size of 100 mesh was purchased from Sigma-Aldrich.

Apparatus

The setup used in this study is shown in **Figure 1**. The main parts of the apparatus are a stainless-steel blind cell and a sapphire cell. The effective volume of the blind cell and the tubes connected on is 130.23 cm^3, and that of the sapphire cell is 61.90 cm^3. The evacuation tube is separated into two lines by V4 and V5. A water displacement device is connected on the V5 through a back-pressure valve V6, which is used to keep the pressure of sapphire cell constant in dissociation experiments, and the range of it is 0 ∼ 1.6 MPa. The displaced water is weighed with a balance and the mass data are recorded by the computer every 5 s. The blind cell and the sapphire cell are installed in an air bath to keep temperature constant, and the pressure of them are determined with two sensors with accuracy of 0.2% in the range of 0 ∼ 20 MPa.

Experimental Procedure

The formation experiment of methane hydrate followed an adsorption-hydration method. Ten gram of porous material/water mixture was loaded in the sapphire cell. When the low water content was adopted (fixed bed), the mixture was compacted with a PTFE rod. The sapphire cell was installed in the air bath, then the stirrer was switched on if the mixture is slurry state. The blind cell was purged by charging methane and vacuuming three times, then it was pressured to 11 MPa with methane. The sapphire cell was vacuumed to 0.003 MPa to desorb the gas adsorbed on the porous material. The temperature of the air bath was set to 293.15 K (T_{ad}) at first—such high temperature was chosen to avoid the hydrate formation during fast adsorption period. When the pressure of the blind cell kept constant for 30 min, the injection valve V2 was opened and the sapphire cell was charged by methane to about 7.8 MPa, then gas adsorption began. The high pressure could provide fast adsorption in the beginning and remain large driving force when the temperature decreases to the hydrate formation region. After the system reached adsorption equilibrium, the temperature of

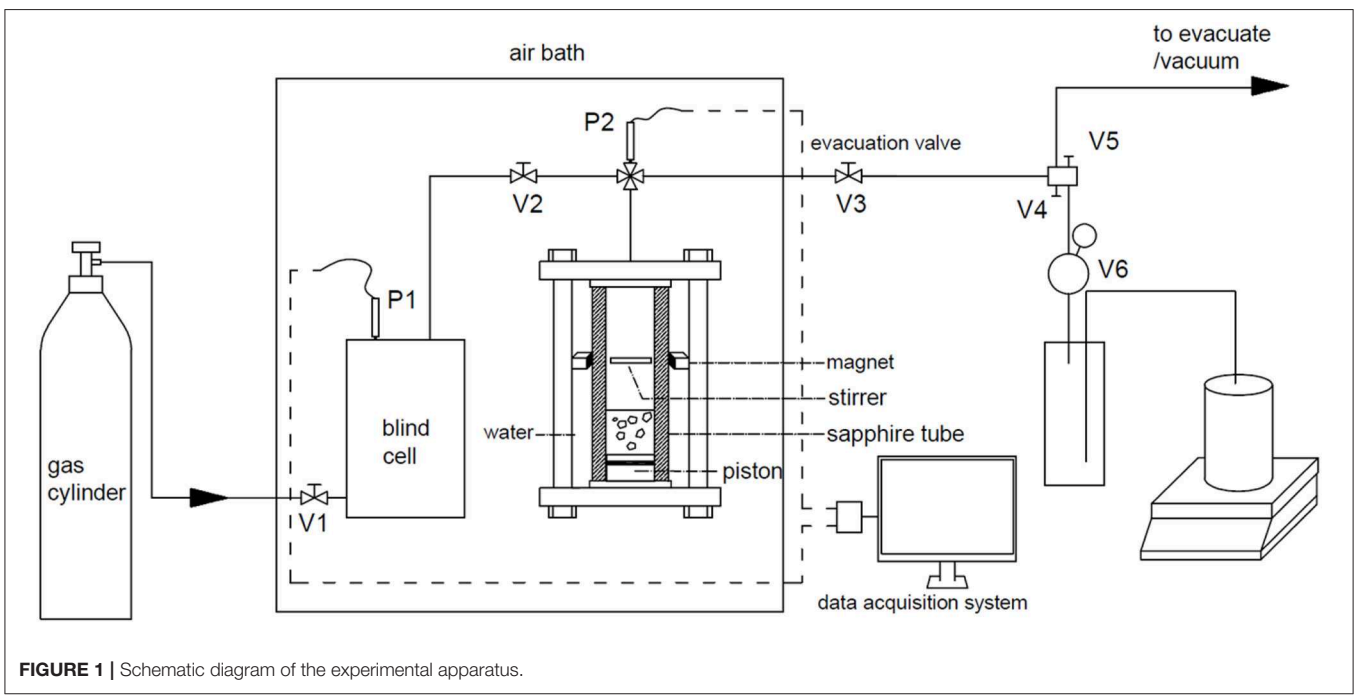

FIGURE 1 | Schematic diagram of the experimental apparatus.

the air bath was set to 278.15 K (T_{hd}) to allow hydrate formation and avoid the water freeze, once the hydrate formed the stirrer was switched off, and methane hydrate formed quiescently during the cooling process. When the decrease rate of reactor pressure lower than 1 kPa per min, the temperature (chilling temperature, T_d) was set to the values below ice point to freeze the hydrate, porous material and unconverted water, so that to retard the gas release. The chilling temperature was between 268.15 and 259.15 K, because the hydrate dissociation in pure water has been proved to be the slowest at 268.15 K (Stern et al., 2001). The chilling procedure lasted for at least 3 h, then the temperature in the reactor was believed to have reached the set value. The valves V3 and V4 were opened and the sapphire was rapidly depressurized to desired value $P_{b,d}$, then the V4 was closed and V5 and V6 were opened, and water in the tank was squeezed out by the released gas. The mass of the displaced water was measured by an online balance and was recorded for every 5 s. During the gas release procedure, the water tank was kept raising to ensure the water level was of the same height as the extremity of the drain pipe. The typical pressure curve is presented in **Figure 2**.

Calculation of the Methane Storage Capacity and Release Rate

The gas storage density was indicated by S_b, and it is calculated by

$$S_b = \frac{22.4 \times 10^{-3} N}{V_{bed}} \tag{1}$$

The V_{bed} represents the apparent volume of the frozen fixed bed, which is composed of hydrate, ice and porous material. It was calculated by

$$V_{bed} = V_0 + 0.25 V_w \tag{2}$$

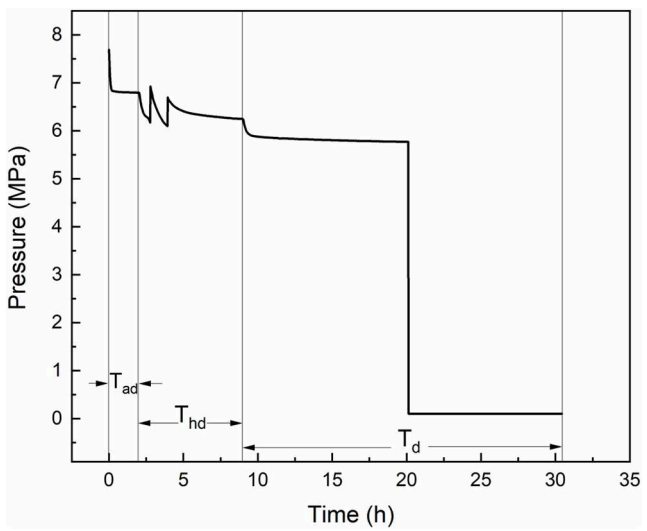

FIGURE 2 | Typical pressure change in the experiment ($P_{b,d}$ = 0.1 MPa).

where the V_0 refers to the initial volume of the slurry or the fixed bed, and it was measured directly. The V_w refers to the volume of water. The N in equation (1) refers to the number of moles of gas fixed in the frozen bed, and it was calculated by

$$N = \frac{P_{a,i} V_a}{Z_{a,i} R T_{ad}} - \frac{P_{a,d} V_a}{Z_{a,d} R T_{hd}} - \frac{P_{b,d} V_{gas}}{Z_{gas} R T_{hd}} \tag{3}$$

where the P and Z represent pressure and compressibility factor, respectively. The compressibility factor Z was calculated by Benedict-Webb-Rubin equation. The subscript a and b represent the blind cell and sapphire cell, respectively. Subscript i refers to the time point of gas injection from blind cell to sapphire, and the subscript d refers to the time point of depressurizing the sapphire cell to dissociation pressure. V_a refers to the effective volume of blind cell. V_{gas} represents the volume of free gas in the sapphire cell, and it was calculated by

$$V_{gas} = V_b - m\upsilon(1 - \varepsilon) - 1.25 V_w \tag{4}$$

where the V_b is the effective volume of the sapphire cell. m represents the mass of the porous material, and υ refers to the packing density of the compacted porous material, m^3/g. ε is the porosity of the compacted material, and it was measured to 0.38 in this study.

In the gas release experiment, the mole number of the collected gas N_{cg} was calculated by

$$N_{cg} = \frac{m_{wc}}{\rho_w} \times \frac{273.15}{T_{env}} \times \frac{1}{22.4 \times 10^3} \tag{5}$$

where the m_{wc} is the mass of water displaced by the released gas, and the ρ_w represents the density of water, g/cm^3. The T_{env} is the ambient temperature.

When depressurizing the reactor to desired dissociation pressure, some gas that had already fixed in the frozen bed escaped into the environment, and the escaped gas is called "gas loss" in this study. The number of moles of the gas loss was calculated by

$$\Delta N = N - N_{cg} \tag{6}$$

In the gas release stage, the release ratio R_r at time t is calculated by

$$R_{r,t} = \frac{N_{cg,t}}{N_{cg}} \tag{7}$$

where $N_{cg,t}$ refers to the mole number of collected gas at time t. The moment that the pressure of the reactor decreased to desired value was set to time *0*.

RESULTS AND DISCUSSION

Methane Storage Capacity

In the porous material contained hydrate formation system, both the gas adsorption and hydration contribute to the gas uptake. Though the existence of water weakens the gas adsorption, the gas adsorption remains an important factor for gas storage. It not only concerns the adsorption capacity, but also affects the hydration: adsorbed gas could be released from the porous material as pressure decrease caused by hydrate formation, and supplies gas from inside of the water. **Figure 3** compares the adsorption capacity of methane on a hydrophilic material (activated carbon) and a hydrophobic material (ZIF-8) at 293.15 K and 6.0 ± 0.2 MPa in slurry. The mass of the slurries and water were 10 g, and the mass ratios of the porous material to slurry were 20 wt.%. As shown, only 0.64 mmol of methane was absorbed in the water. The methane uptake in the ZIF-8 slurry and activated carbon slurry were 10.65 and 4.28 mmol, respectively, which were obviously higher than that in pure water. The adsorption capacities of methane on dry ZIF-8 and activated carbon were 5.14 and 4.98 mmol/g at 293.15 K and 6.0 MPa (measured with a RUBOTHERM Gravimetric Sorption Analyzer), respectively. Compared with dry material, the activated carbon lost almost 62.17% of the adsorption capacity in the slurry, while ZIF-8 retained 98.62% of adsorption capacity. Meanwhile, the ZIF-8 slurry reached the adsorption equilibrium within 8 min, which was obviously faster than the activated carbon slurry. The higher adsorption capacity and faster adsorption rate makes it a better porous material to form slurry. It could adsorb more gas before being frozen in the hydrate/ice, so that increase the storage capacity of the slurry. In the following experiments, the ZIF-8 was chosen as the porous particle in the slurry.

The results of hydrate formation and gas release experiments in ZIF-8 slurries/fixed beds are listed in **Table 1**. Both the adsorbed and hydrated gas are included in the "gas uptake" in the table because there was no a distinct boundary between the adsorption and hydration process as the adsorption was a dynamic process affected both by decreasing temperature and pressure. The dynamic process could be described as: The system reached adsorption equilibrium at 293.15 K at first, then the temperature was adjusted to 278.15 K, more gas was adsorbed on the porous materials because the gas adsorption is more pronounced at lower temperature. When hydrate started to form in the slurry, there existed a dramatic pressure drop, the already-existed adsorption equilibrium was broken, and some gas was released from the porous materials. When the chilling process was started, some gas would be re-adsorbed on porous materials, and the re-adsorption could be affected by the freeze of the fixed bed. The "collected gas" refers to the recovered gas from the hydrate and the ZIF-8, and it was calculated based on the amount of the displaced water and the environment temperature. The "gas loss" is the amount difference between the gas uptake and the collected gas, and it reflects the gas release during depressurization. The "apparent bed volume" is the bulk volume of the mixture of ZIF-8, ice and hydrate before depressurizing the reactor to desired pressure.

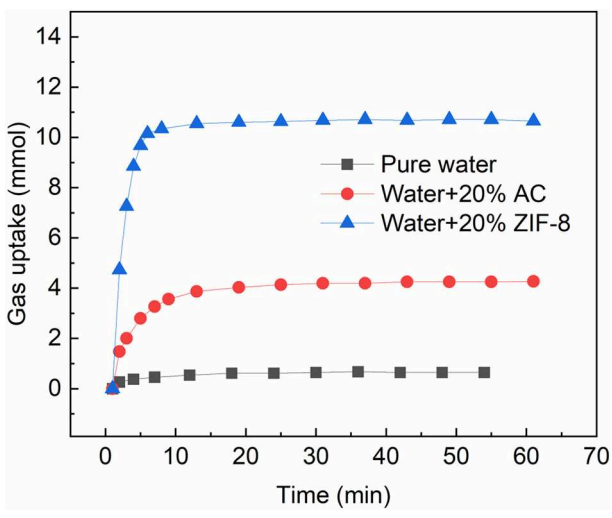

FIGURE 3 | Gas uptake of methane in ZIF-8 and activated carbon slurries at 293.15 K and 6.0 MPa.

In runs 1 ~ 6, the gas storage capacity in ZIF-8 slurry/fixed bed with different solid contents were investigated. The mixture of ZIF-8 and water was in slurry form when the solid content was lower than 40 wt.%, and it was in fixed bed form when the solid content was higher than 60 wt.%. As shown, the apparent bed volume did not monotonously increase with the increase of solid content though the ZIF-8 has a bigger bulk volume than water under the same mass. It decreased with the increase of solid content at first and reached the smallest volume of 13.22 cm^3 at solid content of 40 wt.%, then it increased with the increase of solid content. This phenomenon has been described by Mu et al., and they thought it was caused by the effect of water on ZIF-8 (Mu et al., 2012).

In the slurries (runs 1∼3), the stirrer was switched off once the hydrate appeared in the slurry, hence the hydrate formation was actually conducted under quiescent condition. Generally, when hydrate quiescently forms in a water dominated system, a rigid hydrate film would appear at the interface between water and gas, resulting low water conversion. In the fixed beds packed with hydrophilic materials and saturated with high water cut, the gas storage capacity also is very small because the adsorption was weakened significantly by the water, meanwhile, the conversion of water to hydrate is hindered by the large water content (Yan et al., 2005). However, in the runs 1 ~ 3, high storage capacities were achieved even in slurry, and when the solid content was 40 wt.%, the storage density reached to 107.51 V/V_{bed}. In many other researches that use porous materials to improve hydrate formation, the gas storage capacity was unsatisfactory: Kim et al. acquired the highest storage capacity of 13.44 V/V_{water} when 0.004 wt.% of multi-walled carbon nanotubes was added into water (Kim et al., 2011); Govindaraj et al. (2015) investigated the kinetics of hydrate formation in the activated carbon suspension (1.0 wt.%) at 275.15 K and 8 MPa and the highest gas storage capacity was 20.3 mmol/mol of water (25.26 V/V_{water}) at 24 h Chari et al. (2013b)acquired a storage capacity of 91.72 V/V_{water}

TABLE 1 | Experimental results of methane uptake and release in ZIF-8 slurries and fixed beds.

No.	T_d (K)	$P_{b,d}$ (MPa)	Solid content (wt.%)	Apparent bed volume (cm^3)	Gas uptake (mmol)	Storage density (V/V_{bed})	Collected gas (mmol)	Gas loss (mmol)
1	263.15	0.1	20	13.65	51.01	83.72	48.64	2.37
2	263.15	0.1	30	13.47	64.44	107.16	57.12	7.32
3	263.15	0.1	40	13.22	63.45	107.51	53.59	9.86
4	263.15	–	60	13.70	18.55	30.33	–	–
5	263.15	0.1	70	14.17	80.60	127.41	63.27	17.33
6	263.15	0.1	100	21.27	75.89	79.92	53.35	22.54
7	268.15	0.1	40	13.22	78.84	133.59	67.77	11.07
8	265.15	0.1	40	13.22	73.80	125.05	62.29	11.51
9	261.15	0.1	40	13.22	61.34	103.93	55.63	5.71
10	259.15	0.1	40	13.22	58.53	99.17	55.86	2.67
11	263.15	0.5	40	13.22	67.20	113.87	59.42	7.78
12	263.15	0.7	40	13.22	63.98	108.41	56.79	7.19
13	263.15	0.9	40	13.22	65.16	100.40	61.51	3.65
14	263.15	1.1	40	13.22	62.99	106.73	58.21	4.78

in nano silica suspensions (12.5 wt.%). The small gas storage capacity in these reports perhaps are mainly because the small dosage of the solid particles used in the suspension. In addition, Govindaraj et al. (2015) suggested that the hydrate formation was more favorable at higher particle concentration, thus Chari et al. (2013b) acquired the higher storage capacity than the other two research, and when they further increased the solid content to 25.0 wt.% (fixed bed), they acquired a much high storage capacity of 190.40 V/V_{water}. Compared with the hydrate formation from suspension/slurry in those works, the storage capacity in ZIF-8 slurry in this work was higher. The high solid content used in this work is one of the reasons for high storage density in the slurry, however, the hydrophobicity nature of the ZIF-8 cannot be neglected either. The effect of the hydrophobicity of ZIF-8 on the storage density could be explained as: the adsorption capacity of ZIF-8 was retained in the slurry because of the hydrophobicity; large amount of gas was adsorbed on ZIF-8 particles, and some of it desorbed during the hydrate formation, providing gas from inside of the slurry, which could alleviate the problem that the hydrate forms slowly in slurry.

In the fixed beds (runs 4∼6), no hydrate formation was observed at solid content of 60 wt.%. This was because the fixed bed was 100% saturated by the water, while the experiment was conducted quiescently. In such situation, the gas uptake of 18.55 mmol was almost contributed by adsorption. When the solid content increased to 70 wt.%, the water dispersion was improved in the fixed bed, and the gas uptake and storage density reached to 80.60 mmol and 127.41 V/V_{bed}, respectively, which were the highest in runs 1 ∼ 6. Compared with the solid content of 60 wt.%, the increased gas uptake was found to be mainly caused by hydrate formation in the fixed with solid content of 70 wt.%. In the dry bed, the gas uptake was slightly lower than that of the bed with solid content of 70 wt.%, however, the storage density was much lower because of the much bigger bulk volume of the dry ZIF-8.

By comparing the slurries and the fixed beds, it could be found that the highest storage density was acquired in the fixed bed with solid content of 70 wt.%. However, this does not mean that the fixed bed with small water content is the best solution for gas storage and transportation. In gas transportation, a low-pressure process could effectively decrease the potential risks and the equipment investment, while when depressurizing the system to a low pressure, some gas that have been fixed already could escape with the free gas. In runs 1∼6, the gas released monotonously increased with the increase of solid content. It was only 2.37 mmol in the slurry with solid content of 20 wt.%, while it reached to 22.54 mmol in dry bed, which accounted for 29.70% of the gas uptake. This was because in the fixed beds with high solid contents, a big part of the gas was fixed by adsorption, which was maintained by Van der Waals force, and the adsorbate was easy to be released when the adsorption equilibrium was broken.

As discussed above, satisfactory storage density could be acquired in slurry and the gas loss was much lower than that in the fixed bed, this suggests that the ZIF-8 slurry could be used for gas storage and transportation by following the adsorption-hydration sequence method. To further increase the storage density, the gas storage experiments in slurries with solid content of 40 wt.% were conducted under different chilling temperatures (runs 7∼10, 3). As shown in **Table 1**, the gas uptake decreased with the decrease of chilling temperature. Generally, gas adsorption is more pronounced under lower temperature. The low gas uptake acquired under lower temperature was mainly caused by the freeze of water—the water was easier to freeze under lower temperature, which would weaken the adsorption and hydration by hindering the gas transfer. The highest gas uptake of 133.59 V/V_{bed} was acquired at chilling temperature of 268.15 K, which was higher than that of the slurries and fixed beds at chilling temperatures of 263.15 K (runs 1∼6), suggesting the gas uptake could be further improved by adjusting the operation conditions. It was much higher than that

in the fixed beds in our previous work (Xiao et al., 2019) and in the suspensions (Kim et al., 2011; Chari et al., 2015). It was noted that in run 9, the gas uptake was 103.93 V/V_{bed}, which was slightly lower than that in runs 3, while the gas loss in run 9 was much lower. This was because the lower temperature decreased the dissociation rate of hydrate, leading to less escaped gas during depressurization. The phenomenon that lower temperature leads to smaller gas loss was especially obvious at temperature of 261.15 and 259.15 K when compared with that at 268.15 and 265.15 K.

Gas Release Rate

A typical hydrate-based gas transportation process includes hydrate formation, transportation and regasification, thus, the gas release rate during hydrate transportation is an important factor to evaluate the transportation method. In runs 1 ∼ 6, the gas release rate was investigated in different slurries and fixed beds. The amount of released gas and the gas release ratio over time are shown in **Figure 4**. Gas release test was not been conducted in run 4 because the gas uptake was too small. As it can be seen in **Figure 4A**, the gas release rate monotonously increased with the increase of solid content, and the gas released faster in fixed beds than that in slurries. This was because a big part of gas was fixed by adsorption in the fixed beds, while in the slurry, the adsorption was weakened by the existence of large amount of water, and a big part of gas was enclathrated in hydrate. In **Figure 4B** it could be found that in the dry ZIF-8, all of the gas released within 2 h. That was slower in the fixed bed with solid content of 70 wt.%, however, it was also much faster than that in the slurries. In the slurry with solid content of 20 wt.%, the gas release rate was the slowest, and just 16.9% of the gas released at 10.17 h. In Liang et al. (2005) work, 37% of the methane hydrate dissociated at 4.5 h and 264.4 K in the wet activated carbon fixed

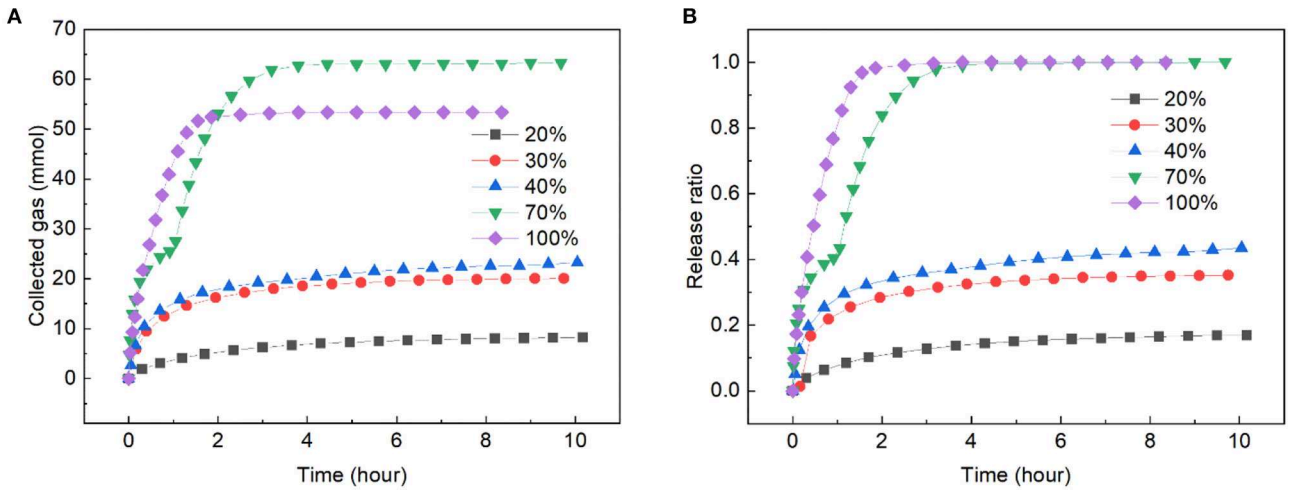

FIGURE 4 | Gas release rate in ZIF-8 slurries and fixed beds with different solid contents at 263.15 K and 0.1 MPa. **(A)** The change of collected gas with time. **(B)** The change of release ratio with time.

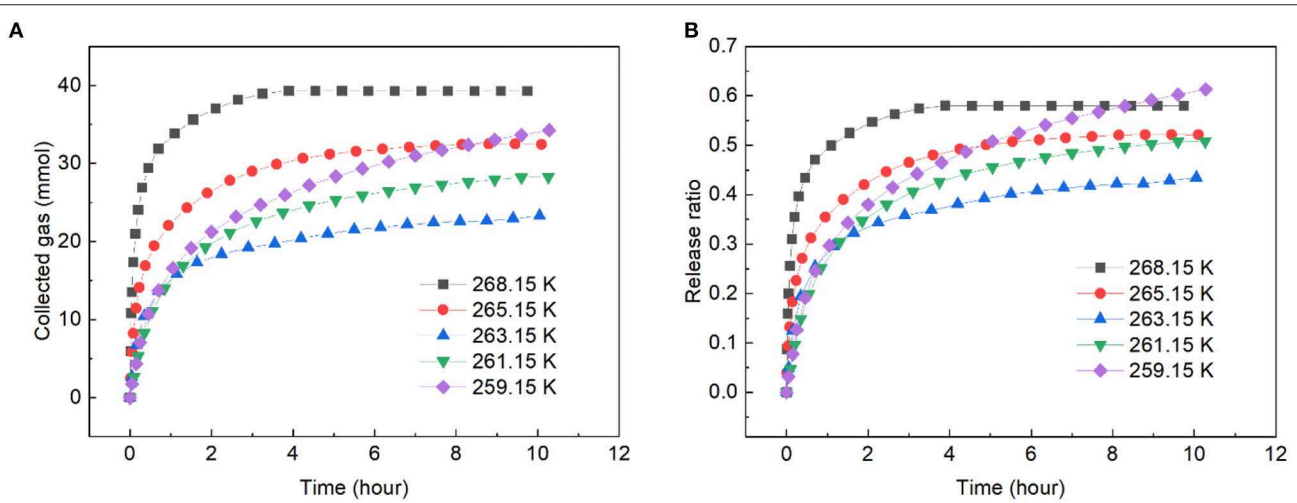

FIGURE 5 | Gas release rate in ZIF-8 slurry with solid content of 40 wt.% at different dissociation temperatures and 0.1 MPa. **(A)** The change of collected gas with time. **(B)** The change of release ratio with time.

bed. When compared with that, the ZIF-8 slurry displayed a slower hydrate dissociation rate than fixed bed.

There existed a very interesting phenomenon during gas releasing in the fixed bed with solid content of 70 wt.%. The curve of collected gas was divided into two parts by an inflection point. Before the point, the released gas was mainly provided by the dissociation of gas hydrate, and after the point it was mainly provided by desorption of the gas. This was because the gas release experiment was performed at 263.15 K, the ZIF-8 particles were wrapped in ice and gas hydrate, and the adsorbed gas was constrained inside the ice though the adsorption equilibrium had been broken after depressurizing the reactor to 0.1 MPa. With the progress of hydrate dissociation, the strength of the hydrate decreased because some water appeared during the conversion of hydrate to ice (Melnikov et al., 2009). Thus, when a certain amount of hydrate dissociated, the gas adsorbed on the ZIF-8 released rapidly, leading to a flection point on the curve.

Figure 5 presents the gas release from the slurry with solid content of 40 wt.% at different dissociation temperatures under 1 atm. As shown, an obvious self-preservation phenomenon appeared in the slurry. The slowest hydrate dissociation is typically occurred at 268.15 K in pure water. When ZIF-8 was added into the water, that point seemed to have shifted to a lower temperature. This was because the impurity of water and the small hydrate particle would increase the hydrate dissociation (Takeya et al., 2005), and in this study, the addition of ZIF-8 increased the impurity of water and porosity of hydrate. The phenomenon that the shift of the self-preservation temperature window has been reported by Prasad and Kiran (2019). The gas release was the fastest at 268.15 K and the slowest release occurred at 263.15 K. At 268.15 K, 57.98% of the gas released at 5 h, this was very close with that in the carbon fixed bed at 268.15 K in our previous work (Xiao et al., 2019). From **Figure 5B**, it was noted that at 263.15 K, 43.42% of the gas released at 10 h, which was faster than that in run 1, indicating that decreasing temperature perhaps is not a good choice to retard the gas release.

In order to decrease the gas release rate, reducing the driving force by increasing the pressure was adopted. **Figure 6** presents the gas release rate of the slurry with solid content of 40 wt.% at 263.15 K and under different pressures. As shown, the release rate decreased with the increase of pressure. At 0.1 MPa, 43.42% of the gas released at 10 h, while only 11.08% of the gas released at 1.1 MPa, which was close to the hydrate dissociation rate in pure water in Liang et al. (2005) work. and it was much slower than the hydrate dissociation in wet carbon bed in Liang et al. (2005) work and our previous work (Xiao et al., 2019). Notably, the gas released with a certain rate at 10 h under 0.1 MPa, while the release ratio of the gas increased very slow under pressure from 0.5 ∼ 1.1 MPa at 10 h, and the curves were almost plat after 7 h for these pressure, indicating that even after a long-time transportation under a suitable pressure, large amount of the gas could remain in the frozen bed, and low-pressure transportation vessels could be used in such transportation to reduce the cost.

CONCLUSIONS

An adsorption-hydration sequence method was adopted in water/porous material mixtures in the purpose of hydrate-based gas storage and transportation. The effect of solid content, temperature on the storage capacity, and the effect of solid content, temperature, pressure on the gas release rate were systemically investigated. 37.83 and 98.62% of the adsorption capacity of methane on dry materials remained in activated carbon and ZIF-8 slurries, respectively. In the ZIF-8 fixed beds, when solid content was 60 wt.%, no hydrate formed under quiescent condition. The highest storage density of 127.41 V/V_{bed} was achieved with solid content of 70 wt.%. By the adsorption-hydration sequence method, satisfactory storage capacity could be acquired even in slurries with solid contents of 20 ∼ 40 wt.%, and the highest storage density at 263.15 K reached to 107.51 V/V_{bed}. The gas loss during depressurization increased with the

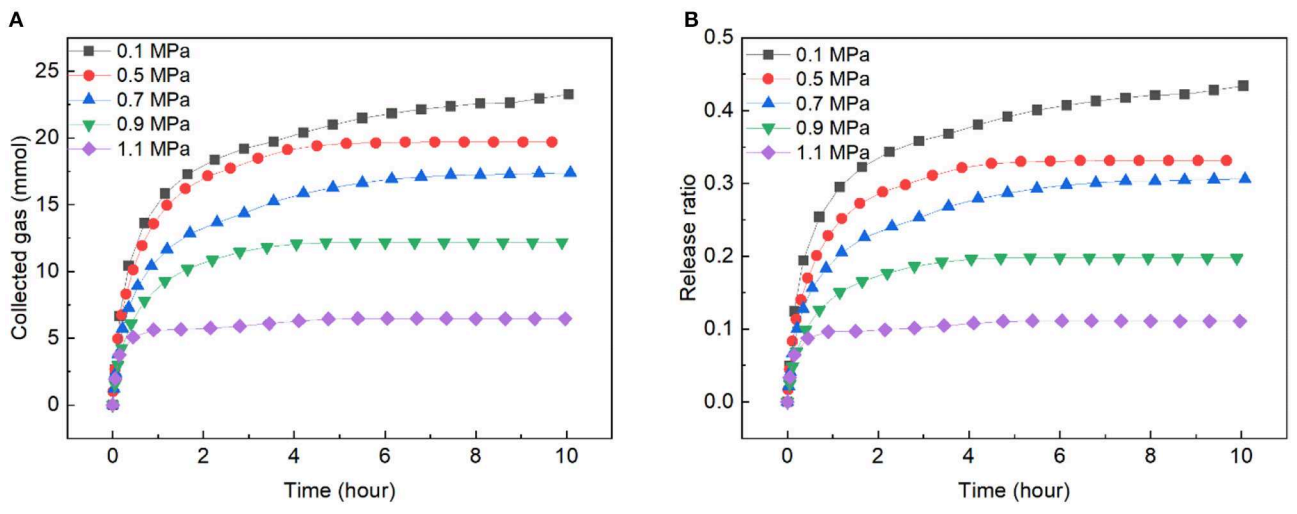

FIGURE 6 | Gas release rate in slurry with solid content of 40 wt.% at different pressures and 263.15 K. **(A)** The change of collected gas with time. **(B)** The change of release ratio with time.

increase of solid content, and 29.70% of the gas that had already stored in dry ZIF-8 escaped during depressurization. Though the storage density of the fixed bed was higher than that in the slurry, the much lower gas loss during depressurization makes the slurry a good choice for gas transportation. The storage density of the slurry monotonically decreased with the decrease of temperature because under lower temperature water was easier to freeze and then affected the hydrate formation.

In gas release experiments in the fixed beds and slurries, the release rate increased with the increase of solid content, and in dry ZIF-8, all of the gas released within 2 h. In the bed with solid content of 70 wt.%, a two-stage release phenomenon could be found because of the gas adsorption and hydration. To retard the gas release, decreasing the temperature did not acquire a satisfactory result. The self-preservation phenomenon could be found in the slurry, however, even at the temperature that provide the slowest gas release rate, 43.42% of the gas released within 10 h, suggesting under atmospheric pressure, adjusting the temperature could not effectively control the gas release. By increasing the pressure, the gas release was well retarded. The gas release rate decreased with the increase of the pressure. At 1.1 MPa, the release ratio was only 11.08% at 10 h, and from the approximately straight line of the release ratio, it could be inferred that the frozen bed could be stored for a long time. In short, with the adsorption-hydration sequence method, up to 133.59 V/V_{bed} of the storage density could be achieved, and by increasing the pressure to 1.1 MPa, 88.92% of the gas stored in the sample could be kept in the frozen bed, suggesting this method is of great potential for gas storage and transportation.

DATA AVAILABILITY STATEMENT

All datasets generated for this study are included in the article/supplementary material.

AUTHOR CONTRIBUTIONS

PX, G-JC, C-YS, and Q-LM designed the experiment, analyzed the data, and drafted the manuscript. J-LC conducted the experiment. D-XZ, M-KY, and E-BZ helped in preparing figures and calculating data. All authors contributed to the discussions and reviewed the manuscript.

FUNDING

This work was financially supported by the National Natural Science Foundation of China (Nos. 51676207, 21636009, 51576209), the National Key Research and Development Program of China (Nos. 2016YFC0304003, 2017YFC0307302), and the China Postdoctoral Science Foundation (Grant No. BX201902466).

REFERENCES

Babu, P., Yee, D., Linga, P., Palmer, A., Khoo, B. C., Tan, T. S., et al. (2013). Morphology of methane hydrate formation in porous media. *Energy Fuels* 27, 3364–3372. doi: 10.1021/ef4004818

Cai, J., Xu, C. G., Xia, Z. M., Chen, Z. Y., and Li, X. S. (2017). Hydrate-based methane separation from coal mine methane gas mixture by bubbling using the scale-up equipment. *Appl. Energy* 204, 1526–1534. doi: 10.1016/j.apenergy.2017.05.010

Casco, M. E., Rey, F., Jordá, J. L., Rudić, S., Fauth, F., Martínez-Escandell, M., et al. (2016). Paving the way for methane hydrate formation on metal–organic frameworks (MOFs). *Chem. Sci.* 7, 3658–3666. doi: 10.1039/c6sc00272b

Chari, V. D., Prasad, P. S. R., and Murthy, S. R. (2015). Hollow silica: a novel material for methane storage. *Oil Gas Sci. Technol.* 70, 1125–1132. doi: 10.2516/ogst/2014019

Chari, V. D., Raju, B., Prasad, P. S. R., and Rao, D. N. (2013a). Methane hydrates in spherical silica matrix: optimization of capillary water. *Energy Fuels* 27, 3679–3684. doi: 10.1021/ef400397x

Chari, V. D., Sharma, D. V. S. G. K., Prasad, P. S. R., and Murthy, S. R. (2013b). Methane hydrates formation and dissociation *in nano* silica suspension. *J. Nat. Gas Sci. Eng.* 11, 7–11. doi: 10.1016/j.jngse.2012.11.004

Circone, S., Stern, L. A., and Kirby, S. H. (2004). The effect of elevated methane pressure on methane hydrate dissociation. *Am. Mineral* 89, 1192–1201. doi: 10.2138/am-2004-8-905

Dicharry, C., Duchateau, C., Asbai, H., Broseta, D., and Torre, J. P. (2013). Carbon dioxide gas hydrate crystallization in porous silica gel particles partially saturated with a surfactant solution. *Chem. Eng. Sci.* 98, 88–97. doi: 10.1016/j.ces.2013.05.015

Dong, H. S., Zhang, L. X., Ling, Z., Zhao, J. F., and Song, Y. C. (2019). The controlling factors and ion exclusion mechanism of hydrate-based pollutant removal. *ACS Sustain. Chem. Eng.* 7, 7932–7940. doi: 10.1021/acssuschemeng.9b00651

Dufour, T., Hoang, H. M., Oignet, J., Osswald, V., Clain, P., Fournaison, L., et al. (2017). Impact of pressure on the dynamic behavior of CO2 hydrate slurry in a stirred tank reactor applied to cold thermal energy storage. *Appl. Energy* 204, 641–652. doi: 10.1016/j.apenergy.2017.07.098

Fidel-Dufour, A., Gruy, F., and Herri, J. M. (2006). Rheology of methane hydrate slurries during their crystallization in a water in dodecane emulsion under flowing. *Chem. Eng. Sci.* 61, 505–515. doi: 10.1016/j.ces.2005.07.001

Fujita, S., Watanabe, K., and Mori, Y. H. (2009). Clathrate-hydrate formation by water spraying onto a porous metal plate exuding a hydrophobic liquid coolant. *AlChE J.* 55, 1056–1064. doi: 10.1002/aic.11744

Fukumoto, K., Tobe, J., Ohmura, R., and Mori, Y. H. (2001). Hydrate formation using water spraying in a hydrophobic gas: a preliminary study. *AlChE J.* 47, 1899–1904. doi: 10.1002/aic.690470821

Gayet, P., Dicharry, C., Marion, G., Graciaa, A., Lachaise, J., and Nesterov, A. (2005). Experimental determination of methane hydrate dissociation curve up to 55MPa by using a small amount of surfactant as hydrate promoter. *Chem. Eng. Sci.* 60, 5751–5758. doi: 10.1016/j.ces.2005.04.069

Govindaraj, V., Mech, D., Pandey, G., Nagarajan, R., and Sangwai, J. S. (2015). Kinetics of methane hydrate formation in the presence of activated carbon and nano-silica suspensions in pure water. *J. Nat. Gas Sci. Eng.* 26, 810–818. doi: 10.1016/j.jngse.2015.07.011

Hao, W. F., Wang, J. Q., Fan, S. S., and Hao, W. B. (2007). Study on methane hydration process in a semi-continuous stirred tank reactor. *Energy Convers. Manage.* 48, 954–960. doi: 10.1016/j.enconman.2006.08.007

He, T. B., Nair, S. K., Babu, P., Linga, P., and Karimi, I. A. (2018). A novel conceptual design of hydrate based desalination (HyDesal) process by utilizing LNG cold energy. *Appl. Energy* 222, 13–24. doi: 10.1016/j.apenergy.2018.04.006

Kim, N. J., Park, S. S., Kim, H. T., and Chun, W. (2011). A comparative study on the enhanced formation of methane hydrate using CM-95 and CM-100 MWCNTs. *Int. Commun. Heat Mass Transf.* 38, 31–36. doi: 10.1016/j.icheatmasstransfer.2010.10.002

Kim, S., Baek, I. H., You, J. K., and Seo, Y. (2015). Guest gas enclathration in tetra-n-butyl ammonium chloride (TBAC) semiclathrates: potential application

to natural gas storage and CO2 capture. *Appl. Energy* 140, 107–112. doi: 10.1016/j.apenergy.2014.11.076

Kumar, A., Sakpal, T., Linga, P., and Kumar, R. (2015). Enhanced carbon dioxide hydrate formation kinetics in a fixed bed reactor filled with metallic packing. *Chem. Eng. Sci*. 122, 78–85. doi: 10.1016/j.ces.2014.09.019

Li, S. F., Shen, Y. M., Liu, D. B., Fan, L. H., and Tan, Z. (2015). Concentrating orange juice through CO2 clathrate hydrate technology. *Chem. Eng. Res. Design* 93, 773–778. doi: 10.1016/j.cherd.2014.07.020

Liang, M. Y., Chen, G. J., Sun, C. Y., Yan, L. J., Liu, J., and Ma, Q. L. (2005). Experimental and modeling study on decomposition kinetics of methane hydrates in different media. *J. Phys. Chem. B* 109, 19034–19041. doi: 10.1021/jp0526851

Liao, Z. X., Guo, X. Q., Li, Q., Sun, Q., Li, J., Yang, L. Y., et al. (2015). Experimental and modeling study on the phase equilibria for hydrates of gas mixtures in TBAB solution. *Chem. Eng. Sci*. 137, 656–664. doi: 10.1016/j.ces.2015.07.019

Lin, W., Chen, G. J., Sun, C. Y., Guo, X. Q., Wu, Z. K., Liang, M. Y., et al. (2004). Effect of surfactant on the formation and dissociation kinetic behavior of methane hydrate. *Chem. Eng. Sci*. 59, 4449–4455. doi: 10.1016/j.ces.2004.07.010

Linga, P., Daraboina, N., Ripmeester, J. A., and Englezos, P. (2012). Enhanced rate of gas hydrate formation in a fixed bed column filled with sand compared to a stirred vessel. *Chem. Eng. Sci*. 68, 617–623. doi: 10.1016/j.ces.2011.10.030

Luo, Y. T., Zhu, J. H., Fan, S. S., and Chen, G. J. (2007). Study on the kinetics of hydrate formation in a bubble column. *Chem. Eng. Sci*. 62, 1000–1009. doi: 10.1016/j.ces.2006.11.004

Lv, Q. N., Li, X. S., Xu, C. G., and Chen, Z. Y. (2012). Experimental investigation of the formation of cyclopentane-methane hydrate in a novel and large-size bubble column reactor. *Ind. Eng. Chem. Res*. 51, 5967–5975. doi: 10.1021/ie202422c

Mandal, A., and Laik, S. (2008). Effect of the promoter on gas hydrate formation and dissociation. *Energy Fuels* 22, 2527–2532. doi: 10.1021/ef800240n

Matsuda, S., Tsuda, H., and Mori, Y. H. (2006). Hydrate formation using water spraying onto a cooled solid surface in a guest gas. *AlChE J*. 52, 2978–2987. doi: 10.1002/aic.10890

Melnikov, V. P., Nesterov, A. N., Reshetnikov, A. M., and Zavodovsky, A. G. (2009). Evidence of liquid water formation during methane hydrates dissociation below the ice point. *Chem. Eng. Sci*. 64, 1160–1166. doi: 10.1016/j.ces.2008.10.067

Mimachi, H., Takeya, S., Gotoh, Y., Yoneyama, A., Hyodo, K., Takeda, T., et al. (2016). Dissociation behaviors of methane hydrate formed from NaCl solutions. *Fluid Phase Equilib*. 413, 22–27. doi: 10.1016/j.fluid.2015.10.029

Mori, Y. H. (2015). On the scale-up of gas-hydrate-forming reactors: the case of gas-dispersion-type reactors. *Energies* 8, 1317–1335. doi: 10.3390/en8021317

Mu, L., Liu, B., Liu, H., Yang, Y. T., Sun, C. Y., and Chen, G. J. (2012). A novel method to improve the gas storage capacity of ZIF-8. *J. Mater. Chem*. 22, 12246–12252. doi: 10.1039/c2jm31541f

Pasieka, J., Coulombe, S., and Servio, P. (2013). Investigating the effects of hydrophobic and hydrophilic multi-wall carbon nanotubes on methane hydrate growth kinetics. *Chem. Eng. Sci*. 104, 998–1002. doi: 10.1016/j.ces.2013.10.037

Prasad, P. S. R., and Kiran, B. S. (2019). Self-preservation and Stability of Methane Hydrates in the Presence of NaCl. *Sci. Rep*. 9:5860. doi: 10.1038/s41598-019-42336-1

Siangsai, A., Rangsunvigit, P., Kitiyanan, B., Kulprathipanja, S., and Linga, P. (2015). Investigation on the roles of activated carbon particle sizes on methane hydrate formation and dissociation. *Chem. Eng. Sci*. 126, 383–389. doi: 10.1016/j.ces.2014.12.047

Sloan, E. D. Jr. (2003). Fundamental principles and applications of natural gas hydrates. *Nature* 426, 353–363. doi: 10.1038/nature02135

Song, Y. C., Dong, H. S., Yang, L., Yang, M. J., Li, Y. H., Ling, Z., et al. (2016). Hydrate-based heavy metal separation from aqueous solution. *Sci. Rep*. 6:21389. doi: 10.1038/srep21389

Stern, L. A., Circone, S., Kirby, S. H., and Durham, W. B. (2001). Anomalous preservation of pure methane hydrate at 1 atm. *J. Phys. Chem. B* 105, 1756–1762. doi: 10.1021/jp003061s

Stern, L. A., Circone, S., Kirby, S. H., and Durham, W. B. (2003). Temperature, pressure, and compositional effects on anomalous or "self" preservation of gas hydrates. *Can. J. Phys*. 81, 271–283. doi: 10.1139/p03-018

Takeya, S., Uchida, T., Nagao, J., Ohmura, R., Shimada, W., Kamata, Y., et al. (2005). Particle size effect of CH4 hydrate for self-preservation. *Chem. Eng. Sci*. 60, 1383–1387. doi: 10.1016/j.ces.2004.10.011

Veluswamy, H. P., Kumar, A., Kumar, R., and Linga, P. (2017). An innovative approach to enhance methane hydrate formation kinetics with leucine for energy storage application. *Appl. Energy* 188, 190–199. doi: 10.1016/j.apenergy.2016.12.002

Wang, F., Jia, Z. Z., Luo, S. J., Fu, S. F., Wang, L., Shi, X. S., et al. (2015). Effects of different anionic surfactants on methane hydrate formation. *Chem. Eng. Sci*. 137, 896–903. doi: 10.1016/j.ces.2015.07.021

Wang, F., Liu, G. Q., Meng, H. L., Guo, G., Luo, S. J., and Guo, R. B. (2016). Improved methane hydrate formation and dissociation with nanosphere-based fixed surfactants as promoters. *ACS Sustain. Chem. Eng*. 4, 2107–2113. doi: 10.1021/acssuschemeng.5b01557

Wang, Y. H., Lang, X. M., and Fan, S. S. (2012). Accelerated nucleation of tetrahydrofuran (THF) hydrate in presence of ZIF-61. *J. Nat. Gas Chem*. 21, 299–301. doi: 10.1016/S1003-9953(11)60367-8

Xiao, P., Yang, X. M., Li, W. Z., Cui, J. L., Sun, C. Y., Chen, G. J., et al. (2019). Improving methane hydrate formation in highly water-saturated fixed bed with diesel oil as gas channel. *Chem. Eng. J*. 368, 299–309. doi: 10.1016/j.cej.2019.02.139

Xu, C. G., Li, X. S., Lv, Q. N., Chen, Z. Y., and Cai, J. (2012). Hydrate-based CO2 (carbon dioxide) capture from IGCC (integrated gasification combined cycle) synthesis gas using bubble method with a set of visual equipment. *Energy* 44, 358–366. doi: 10.1016/j.energy.2012.06.021

Yan, L. J., Chen, G. J., Pang, W. X., and Liu, J. (2005). Experimental and modeling study on hydrate formation in wet activated carbon. *J. Phys. Chem. B* 109, 6025–6030. doi: 10.1021/jp045679y

Yang, M. J., Song, Y. C., Jiang, L. L., Liu, Y., and Wang, X. J. (2015). Behaviour of hydrate-based technology for H2/CO2 separation in glass beads. *Sep. Purif. Technol*. 141, 170–178. doi: 10.1016/j.seppur.2014.11.019

Yang, S. H. B., Babu, P., Chua, S. F. S., and Linga, P. (2016). Carbon dioxide hydrate kinetics in porous media with and without salts. *Appl. Energy* 162, 1131–1140. doi: 10.1016/j.apenergy.2014.11.052

Zhong, Y., and Rogers, R. E. (2000). Surfactant effects on gas hydrate formation. *Chem. Eng. Sci*. 55, 4175–4187. doi: 10.1016/S0009-2509(00)00072-5

Zhou, L., Liu, X., Sun, Y., Li, J., and Zhou, Y. (2005). Methane sorption in ordered mesoporous silica SBA-15 in the presence of water. *J. Phys. Chem. B* 109, 22710–22714. doi: 10.1021/jp0546002

Zhou, S. D., Yu, Y. S., Zhao, M. M., Wang, S. L., and Zhang, G. Z. (2014). Effect of graphite nanoparticles on promoting CO2 hydrate formation. *Energy Fuels* 28, 4694–4698. doi: 10.1021/ef5000886

Conflict of Interest: The authors declare that the research was conducted in the absence of any commercial or financial relationships that could be construed as a potential conflict of interest.

frontiers in Chemistry

ORIGINAL RESEARCH
published: 05 June 2020
doi: 10.3389/fchem.2020.00480

Contribution of Ultra-Fine Bubbles to Promoting Effect on Propane Hydrate Formation

Tsutomu Uchida[1], Hiroshi Miyoshi[2], Ren Sugibuchi[2], Akio Suzuta[2], Kenji Yamazaki[1] and Kazutoshi Gohara[1]*

[1] Faculty of Engineering, Hokkaido University, Sapporo, Japan, [2] Graduate School of Engineering, Hokkaido University, Sapporo, Japan

To investigate experimentally how ultra-fine bubbles (UFBs) may promote hydrate formation, we examined the formation of propane (C_3H_8) hydrate from UFB-infused water solution using two preparation methods. In one method, we used C_3H_8-hydrate dissociated water, and in the other, C_3H_8-UFB-included water prepared with a generator. In both solutions, the initial conditions had a UFB number density of up to 10^9 mL^{-1}. This number density decreased by only about a half when stored at room temperature for 2 days, indicating that enough amount of UFBs were stably present at least during the formation experiments. Compared to the case without UFBs, the nucleation probabilities within 50 h were ∼1.3 times higher with the UFBs, and the induction times, the time period required for the bulk hydrate formation, were significantly shortened. These results confirmed that UFB-containing water promotes C_3H_8-hydrate formation. Combined with the UFB-stability experiments, we conclude that a high number density of UFBs in water contributes to the hydrate promoting effect. Also, consistent with previous research, the present study on C_3H_8 hydrates showed that the promoting effect would occur even in water that had not experienced any hydrate structures. Applying these findings to the debate over the promoting (or "memory") effect of gas hydrates, we argue that the gas dissolution hypothesis is the more likely explanation for the effect.

Keywords: nanobubble, stability, number density, memory effect, propane, induction time

OPEN ACCESS

Edited by:
Amadeu K. Sum, Colorado School of Mines, United States

Reviewed by:
Jiafei Zhao, Dalian University of Technology, China
Alejandro Gil-Villegas, University of Guanajuato, Mexico

****Correspondence:***
Tsutomu Uchida
t-uchida@eng.hokudai.ac.jp

Specialty section:
This article was submitted to Physical Chemistry and Chemical Physics, a section of the journal Frontiers in Chemistry

Received: *26 March 2020*
Accepted: *08 May 2020*
Published: *05 June 2020*

Citation:
Uchida T, Miyoshi H, Sugibuchi R, Suzuta A, Yamazaki K and Gohara K (2020) Contribution of Ultra-Fine Bubbles to Promoting Effect on Propane Hydrate Formation. Front. Chem. 8:480. doi: 10.3389/fchem.2020.00480

INTRODUCTION

Gas hydrates that exist below the deep sea floor are both an unconventional natural gas resource and a potential source of greenhouse gas. In addition, gas-hydrate formation can be a nuisance when it starts to plug gas pipelines in cold regions. Such interests have stimulated much research and development on gas hydrates (Kvenvolden, 1988; Sloan, 2004; Sloan and Koh, 2007; Masuda et al., 2016). For example, with the gas pipeline issue, research has focused on suppressing the formation and growth of gas hydrate. However, as the hydrate form contains gas at relatively high density, gas hydrate is regarded as a promising medium for transporting and storing the gas (Gudmundsson and Borrehaug, 1996; Ida and Kohda, 2004; Horiguchi et al., 2011; Mimachi et al., 2014; Takeya et al., 2018).

Gas hydrate is formed by a reaction between water and the guest gas at low temperatures and high pressures. But the nucleation of gas-hydrate crystals requires a relatively large supercooling (or super-saturation). Such conditions necessitate additional energy for gas-hydrate formation and make it difficult to control the formation process. Thus, a key research goal is to find more efficient ways to form gas hydrates.

Propane (C_3H_8) is the main component of LPG and a component of natural gas. Its solubility in water (about 2.7×10^{-5} in mole fraction at 293.2 K; (The Chemical Society of Japan, 2004)) is similar to methane (CH_4). The formation of C_3H_8 hydrate via the reaction between C_3H_8 gas and pure water is difficult (Christiansen and Sloan, 1994; Giavarini et al., 2003). This difficulty has been understood as a consequence of the labile-cluster nucleation hypothesis, in particular, a difficulty in forming hexakaidecahedral ($5^{12}6^4$) cavities (Christiansen and Sloan, 1994).

At present, the "memory effect" is the most promising way to increase the efficiency of forming gas hydrate (Ripmeester and Alavi, 2016). Another way to promote C_3H_8-hydrate formation is by using "ice-melting water," which is water from just-melted ice Giavarini et al. (2003). Ida and Kohda (2004) investigated several such methods, arguing that the micro-bubble method was the most promising way. The mechanism by which this method works was argued to be the increase of gas-liquid interface. Zeng et al. (2006) confirmed the memory effect of C_3H_8 hydrate when they used the C_3H_8-hydrate melt water although they aimed to investigate the inhibition effect of anti-freeze proteins on the C_3H_8-hydrate formation.

The memory effect is a phenomenon in which once a formed crystal is dissociated into gas and water, and then reformed, the crystallization occurs with lower supercooling or supersaturation than when the crystal was initially formed. The mechanism is still under debate, and several hypotheses have been proposed. One hypothesis is the "water structuring hypothesis" that the fragments of hydrate-lattice structure remains in the dissociated water (Hwang et al., 1990; Parent and Bishnoi, 1996; Ohmura et al., 2003; Buchanan et al., 2005; Sloan and Koh, 2007; Sefidroodi et al., 2013). This is consistent with the concept that water has a dynamic structure, so it is considered to be a promising hypothesis. However, the existence of such "fragments" has not been established.

Another hypothesis is the "gas dissolution hypothesis" that comes from the requirement of a sufficient concentration of guest molecules in the liquid phase for hydrate to form (Rodger, 2000). Most guest molecules are hydrophobic, with relatively low solubility in water. In the crystalline gas hydrate, the gas concentration is hundreds of times its solubility in water, thus when the hydrate grows, a large amount of guest molecules must be supplied from the gas phase. For example, the mole fraction of C_3H_8 over H_2O in the hydrate structure is estimated to be about two thousand times that of the C_3H_8 solubility in water. This difficulty of acquiring enough guest molecules is considered to be a major barrier to crystallization. Uchida et al. (2016a,b); Uchida et al. (2017, 2020) demonstrated experimentally the presence of ultra-fine bubbles (UFBs) in hydrate-dissociated water. They argued that the UFBs are a source of guest molecules to the liquid phase, and they suggested that these UFBs produce the memory effect via the gas dissolution hypothesis.

UFBs are small gas bubbles $<1\,\mu$m (ISO 20408-1:2017, 2017). They have unique properties such as low buoyancy, high internal pressure, and a low rate of coalescence due to repulsive forces from their negative surface charges (ζ-potential) (Takahashi, 2005; Seddon et al., 2012; Oshita and Uchida, 2013). These properties allow UFBs to remain in the liquid for a long time. Usually, UFB-containing water is prepared with a fine-bubble generator. Our previous studies (Uchida et al., 2016a,b, 2017, 2020) have confirmed that gas hydrate dissociation produces a high concentration of UFBs in water. This phenomenon is also supported by molecular dynamic simulations (Yagasaki et al., 2014; Bagherzadeh et al., 2015).

The relationship between UFBs and the memory effect has been studied using CH_4, ethane (C_2H_6), and carbon dioxide (CO_2) hydrates (Uchida et al., 2016a,b, 2017, 2020). All of these hydrates have the same sI (structure-I) hydrate. Here we ask whether the UFBs have the same role in the memory effect of the sII (structure-II) hydrate by studying the effect experimentally using C_3H_8 gas. As UFBs used in the present study were much smaller than micro bubbles, our approach differs from the micro-bubble method proposed by Ida and Kohda (2004). Therefore, we also investigated the stability of C_3H_8-UFBs by their number density change with storage time at room temperature.

EXPERIMENTAL METHODS

Materials and UFB Measurements

As in our previous studies (Uchida et al., 2016b, 2020), three liquid samples were used for the experiments: pure water, C_3H_8-hydrate dissociated water, and C_3H_8-UFB-included water. Pure water here means ion-exchanged distilled water of resistivity about 15 MΩ cm. The C_3H_8-hydrate dissociated water was prepared by dissolving about 2.5 g of C_3H_8-hydrate crystal in about 50 mL of pure water at about 293 K. The source crystal for this sample was retrieved from our reaction vessel at about 200 K. The C_3H_8-UFB-included water was prepared with a micro-bubble generator (Aura Tec, Fukuoka, Japan, type OM4-MDG-045) by supplying C_3H_8 gas (99% in purity, Hokkaido Air Water, Hokkaido, Japan) at 0.25 MPa into 1 L of pure water maintained at 293 K by immersing the water-filled beaker into the temperature-controlled bath (Otsuka Electronics, Osaka, Japan, type NM-454L). To obtain sufficient UFBs, the circulating time was set for 1 h. These liquids were used for the C_3H_8-hydrate formation test more than 1 h after the complete disappearance of micro- or macroscopic bubbles. The pH value was measured with a pH sensor (Sato Keiryoki, Tokyo, Japan, type SK-620PHII).

The number and size distributions of UFBs in the solution were measured by both laser-light scattering (LS) and by freeze-fractured replica observation via transmission electron microscope (FFT). In the LS technique, an Ar-ion laser (Omnichrome, CA, USA, type 543-150 GS, $\lambda = 514.5$ nm, 5

Abbreviations: UFB, ultra-fine bubble (sub-micron sized); FFT, freeze-fractured replica observation via transmission electron microscope; LS, laser-light scattering; PTA, particle tracking analysis.

mW) light was introduced into an optical glass cell (Toshinriko, Tokyo, Japan, type PSK-3: about 1 cm^3) in which each liquid sample had been dispensed. The 90-degree light scattering image was recorded by CCD camera (Watec, Yamagata, Japan, type WAT-232S) from which we counted the bright spots in a unit volume (using Image J software). The average number density was estimated from 16 images for each sample. Preliminary experiments have confirmed that this method can measure UFBs with a diameter of larger than 300 nm and with the number density more than 10^6 mL^{-1} (Uchida et al., 2020).

The FFT method we used is described in detail in Uchida et al. (2016a,b,c); Uchida et al. (2020), so we describe it only briefly here. A small amount (<10 μL) of liquid sample was quickly frozen by immersing it into liquid nitrogen. The frozen sample was then set in the replication system (JEOL, Tokyo, Japan, type JFD-9010) and fractured under low temperature (about 150 K) and high vacuum ($<10^{-4}$ Pa) conditions to form a freshly fractured surface. On this surface, both platinum and carbon were deposited to form a thin film that replicates the roughness of the fractured surface. After transferring to a Cu-grid having 43 μm × 43 μm opening, we observed the fractured surface using a high-resolution transmission electron microscope (TEM: JEOL, JEM-2010, at 200 kV accelerating voltage). An imaging plate (Fujifilm, Tokyo, Japan, type FDL-UR-V) was used for acquiring the observed image. This method allows us to observe UFBs, and distinguish them from impurities (the former is a hemispherical hollow, the latter sticks up). To obtain the average value of the UFB distribution, we measured at least three independent replica-film samples for a specified liquid sample.

To overcome the limitation of the FFT measurement and to cover the wider size-ranged UFBs, we combine another measurement method. For observing the smaller UFBs, we used the commercially available particle tracking analysis (PTA) method (Quantum Design Japan, Tokyo, Japan, type NS500, λ = 635 nm). This system allowed us to obtain the particle size distributions and the average number density of UFBs having diameters of about 20–300 nm. The averaged values for the UFB distribution were estimated from at least six measurements for a specified liquid sample.

With the above methods, we measured the size and density of UFBs immediately after preparing the samples by storing the liquid sample in glass bottles (about 6.5 mL, without head space) at room temperature. The average number densities were measured by LS and PTA methods for 2 days. As mentioned in our previous studies (Uchida et al., 2016a,b,c), the number density measured by the FFT method would be affected by the quenching process. Thus, we avoid the quantitative comparison between results obtained by different methods in the present study.

C_3H_8-hydrate Formation and Evaluation of Promoting Effects

We used the same system as that in our previous study (Uchida et al., 2016a, 2020) for the C_3H_8-hydrate formation tests. Briefly, about 50 cm^3 of liquid sample was set in a batch-type reaction vessel (inner volume: 232.2 cm^3). To reduce formation of surface nanobubbles on the reaction vessel wall after introducing the liquid sample, the UFB-containing water was stored at room temperature for at least 1 h prior to its use in the experiments. The sample was free of visible bubbles. After the purge process, C_3H_8 gas was pressurized at a set value (about 0.45 MPa). The temperature of the vessel containing the sample was controlled by immersing in a cooling bath set at 273.9 ± 0.4 K. The C_3H_8-hydrate formation tests were started with a gentle agitation of about 300 rpm.

The promoting effect is defined as the decrease in length of the induction time of gas hydrate formation Δt compared to the control condition (with pure water in the present study). The induction time is the time from when the temperature in the vessel reaches the equilibrium value to the time when the temperature of the vessel increases suddenly due to the exothermic process of hydrate formation. The latter time is also recognized by the sudden pressure drop due to the consumption of C_3H_8 gas. If the hydrate did not form by 50 h, we stopped the experiment and defined it "not formed." As the nucleation process of gas hydrate is known to be stochastic, we evaluate the probability nucleation rate $P(t)$ from 11 repeated experiments. The curve fitting was done by OriginPro (OriginLab, ver. 9.0J). The strength of the promoting effect $<\Delta t_{ind}>$ is defined as the integration over time of $P_{UFB}(t) - P_{pw}(t)$, where $P_{UFB}(t)$ is the rate for the UFB-containing water, $P_{pw}(t)$ that for pure water.

For the statistical analysis, we estimate the significance using the Tukey-Kramer test (MS Excel 2010 and BellCurve) for at least 95% confidence ($p < 0.05$).

RESULTS AND DISCUSSION

Distribution of UFBs in C_3H_8-hydrate Dissociated Water

Some of the liquid sample used for the hydrate-formation experiment was set aside for analyzing its size distribution of UFBs by the LS method, the PTA method, and the FFT method. **Figure 1** shows typical TEM images of C_3H_8 UFBs in the C_3H_8-hydrate dissociated water obtained by the FFT method. Consistent with this image, we found that most UFBs are spherical or oval, and that their size distributions had similarities to those observed in other hydrocarbon-gas UFBs (Uchida et al., 2016a,b).

We calculated the average particle size D and the number density N of C_3H_8 UFBs in each liquid sample. These quantities were calculated within 1 h of sample preparation and 1 day later. For example, results in **Table 1** show for the LS measurements that UFBs over 300 nm in diameter had a number density of 10.7 (± 4.2) $\times 10^8$ mL^{-1} in the C_3H_8-hydrate dissociated water, but had the slightly lower concentration of 8.1 (± 2.7) $\times 10^8$ mL^{-1} in the C_3H_8-UFB-included water. These values are considered to be appropriate by the comparison to those obtained by the PTA method, although they are smaller than those obtained by other methods. Overall, there is little difference in number density between the UFB-included and the hydrate-dissociated samples. Thus, the C_3H_8 UFBs generated by the hydrate dissociation appear to roughly stabilize at the same

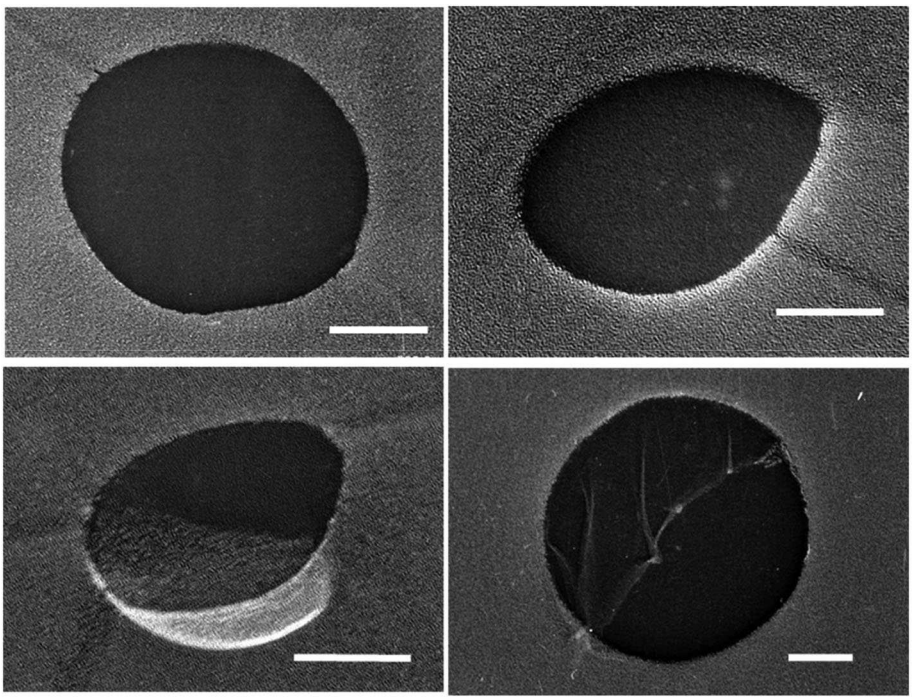

FIGURE 1 | Typical TEM images of UFBs in C_3H_8-hydrate dissociation water by the freeze-fracture replica (FFT) method. Scale bars show 100 nm.

TABLE 1 | Average diameter *D* and number density *N* of UFBs in samples measured by LS, PTA, and FFT methods.

	***D* [nm]**	***N* [$\times 10^8$ mL^{-1}]**
C_3H_8-UFB-included water	> 300 (LS) 100 ± 20 →124 ± 28 (PTA)	8.1 ± 2.7 →6.5 ± 2.6 (LS) 0.77 ± 0.07→ 0.55 ± 0.11 (PTA)
C_3H_8-hydrate dissociated water	385 ± 283→ 746 ± 401 (FFT)* > 300 (LS) 133 ± 11→ 141 ± 14 (PTA) pH: 6.7	6.4 ± 2.1→ 7.4 ± 3.2 (FFT) 10.7 ± 4.2→ 6.8 ± 4.1 (LS) 2.1 ± 1.3 →1.7 ± 0.8 (PTA)*
Pure water	N.A.	N.A.

Arrows show the change between the value within 1 h of sample preparation and that after about 24 h at room temperature. Asterisks mark those with a significant difference ($p < 0.05$). N.A. means that sufficient number of UFBs were not measured in liquid samples.

number density as that prepared by the UFB generator. N.A. in **Table 1** means that sufficient number of UFBs were not measured in liquid pure water.

This conclusion is consistent with findings from other hydrocarbon-gas hydrates (CH_4: Uchida et al., 2016a; C_2H_6: Uchida et al., 2016b), although the number densities are larger than those from CO_2-hydrate dissociated water (Uchida et al., 2020). In our previous study (Uchida et al., 2016c, 2020), we suggested that the UFB density might respond to the solubility and pH. Thus, we expect such similarity with other hydrocarbons because the solubility of C_3H_8 gas in water is similar to that of CH_4 and because the pH value of the dissociated water is around seven (**Table 1**). In addition, the higher number density of UFBs in this case compared to the CO_2-hydrate case is consistent with the higher pH conditions (Uchida et al., 2020).

Figure 2 shows how the number densities decreased with time over 2 days. The values are normalized by the initial number density (averaged data, within 1 h of generation). Each error bar shows the standard deviation. The relatively large UFBs (larger than 300 nm) in the C_3H_8-hydrate dissociated water decrease in proportion to the storage time (**Figure 2A**), decreasing over 50% after 50 h. In contrast, these larger UFBs in the UFB-included water decrease initially by about 10%, within a few hours of generation, but then decreased much more slowly, decreasing another 10% over 50 h. Thus, after 50 h, the residual ratio is about 0.8, about twice that of the C_3H_8-hydrate dissociated water. Assuming a linear decrease with time, the decrease rates of UFBs in the UFB-included water and in the C_3H_8-hydrate dissociated water are about -0.08×10^6 mL^{-1} h^{-1} and -1.33×10^6 mL^{-1} h^{-1}, respectively. That is, the difference in the decrease rates is over an order of magnitude.

For the smaller UFBs, the number densities decrease as shown in **Figure 2B**. Despite the initial number densities differing significantly (**Table 1**), the residual ratios of UFBs around 100 nm in diameter are nearly equal after about 50 h. Specifically, their linear rates of decrease are about -0.50×10^6 mL^{-1} h^{-1} for the UFB-included samples and -0.62×10^6 mL^{-1} h^{-1} for the hydrate-dissociated samples. Therefore, for both the larger and smaller UFBs, the number in the hydrate-dissociated water tends

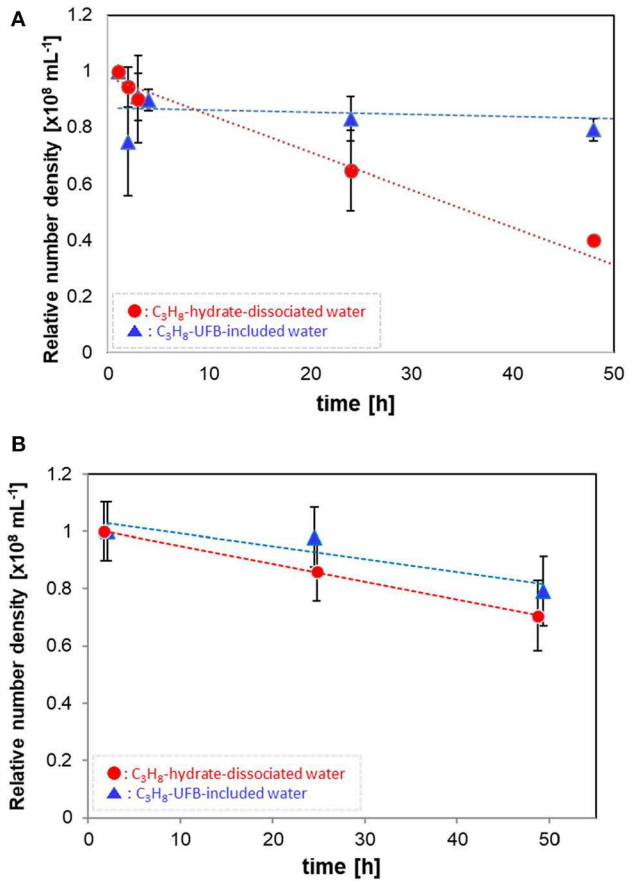

FIGURE 2 | Number densities of C_3H_8 UFBs in the water samples normalized by the initial value. **(A)** Measured by the LS method ($D > 300$ nm). **(B)** Measured by the PTA method ($D \sim 100$ nm).

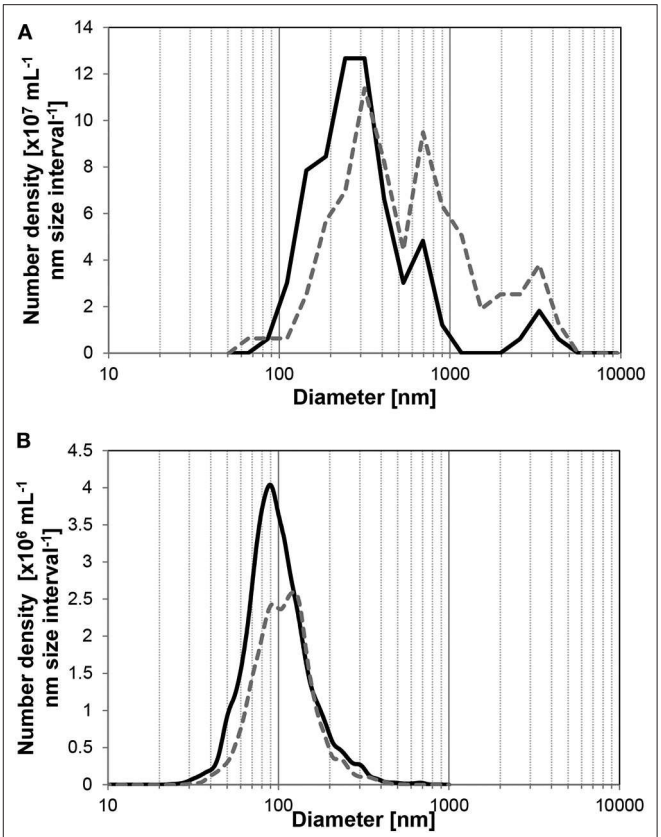

FIGURE 3 | Average size distributions of UFBs in C_3H_8-hydrate dissociated water. Solid line is the initial distribution, dashed line is that after 1 day. **(A)** By FFT observations ($n > 4$). **(B)** By PTA measurements ($n > 6$).

to decrease faster than that in the UFB-included water, at least over the size range observed here.

The size distribution of UFBs also changed with time. To observe the size distribution of UFBs in wider range, we must combine the different measurement methods here. As shown in **Figure 3**, the FFT measurement covers the larger UFBs whereas the PTA measurement covers smaller ones which slightly overlaps at the range about 100 nm. The FFT measurements of larger UFBs in the hydrate-dissociated samples in **Figure 3A** shows that the distribution shifts to larger sizes over time. Similarly, the size distribution from the PTA measurements show a shift to larger sizes (**Figure 3B**). This shift is small, and arises from a preferential decrease in the UFBs smaller than 100 nm. These data suggest that the initial distribution has a large distribution of sizes, from several tens of nanometers to several micrometers, but that after 1 day or more, the average value increases due to the disappearance of small UFBs or the growth of UFBs into micro-bubbles. These trends in average diameter and number density suggest Ostwald ripening, in which small UFBs dissolved and large UFBs grew, with the largest UFBs disappearing during the storage period due to their increase in buoyancy. But regardless of these processes, the number density remained of order 10^8 mL^{-1} in the C_3H_8-hydrate dissociated water during a 2-day storage period.

For the larger UFBs (over 300 nm diameter), the difference in lifespans (residual ratio) between that in the UFB-included water and that in the C_3H_8-hydrate dissociated water is likely due to the difference in the UFB-generation methods. As the UFB-included water was prepared with 1-h aeration during the UFB generation, the C_3H_8 concentration in the water should be sufficiently saturated. However, the C_3H_8-hydrate dissociated water is prepared by dissolving several crystalline pieces in pure water. Thus, the solution might not initially be saturated. UFBs are stable in water supersaturated with the source gas (Uchida et al., 2016c). Therefore, the residual ratio of UFBs in the C_3H_8-hydrate dissociated water would be lower than in C_3H_8-UFB-included water because most of the UFBs initially formed during hydrate dissociation soon dissolve into the water. UFBs larger than 300 nm tend to dissolve preferentially in the smaller supersaturated solution (e.g., in C_3H_8-hydrate dissociated water), whereas UFBs smaller than 100 nm preferentially dissolve in the sufficiently supersaturated solution (e.g., in C_3H_8-UFB included water).

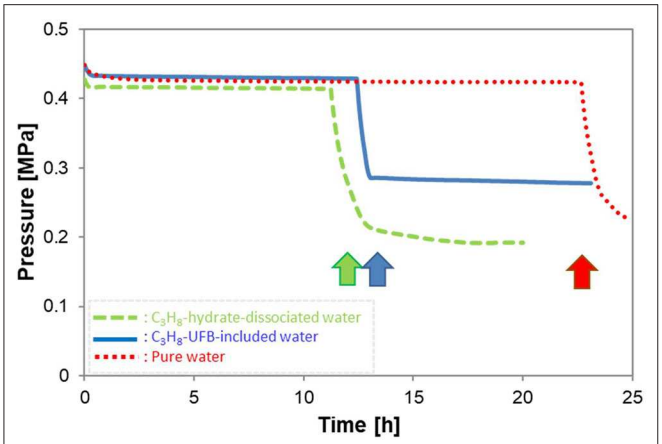

FIGURE 4 | Typical pressure profiles during hydrate formation with three kinds of solutions. Arrows show the hydrate formation point, giving the induction time.

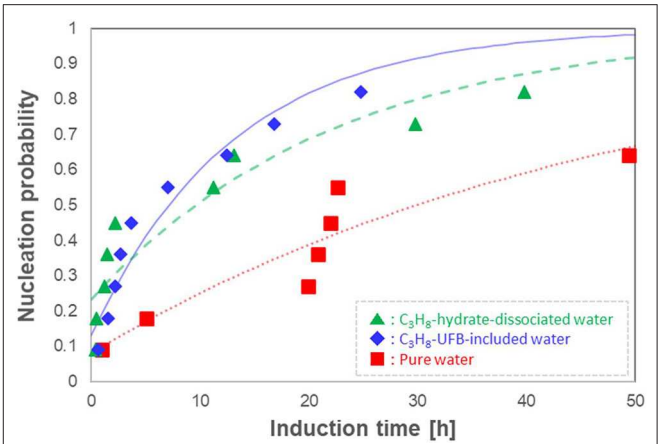

FIGURE 5 | Nucleation probability of C_3H_8 hydrate vs. induction time ($n = 11$). Each curve is a fit from Equation (1).

The total number density of C_3H_8 UFBs in the solution in which C_3H_8 hydrate has just dissociated is estimated to be of order $10^9 \sim 10^{10}$ mL^{-1}. So, the use of C_3H_8-hydrate dissociated water, as done in other memory-effect experiments (such as (Zeng et al., 2006)), should have a sufficient initial supply of C_3H_8. The lifespan of UFBs in such dissociated water should be as long as that observed in the UFB-included water prepared by the UFB generator.

Induction Time Measurements of C_3H_8 Hydrates

Figure 4 shows typical pressure profiles in the vessel with formation of C_3H_8 hydrate under the conditions of $P = 0.45$ MPa and $T = 273.9$ K. All three types of liquid samples are shown. After C_3H_8 gas was introduced into the vessel, its pressure decreased slightly due to the temperature drop from room temperature. In the figure, time zero is when the temperature and pressure of the vessel reached the equilibrium ones (about 278 K at 0.45 MPa). Thus, the subsequent pressure drop indicates C_3H_8-hydrate formation (shown by arrows), so the time of this sudden drop in pressure is the induction time. Simultaneously with the pressure drop, the temperature rose. But of every 8 experiments with hydrate formation, about 3 others did not produce hydrate within 50 h. When the latter occurred, we counted it as "non-generation."

Instead of the tens of minutes induction time of other gas hydrates (C_2H_6 hydrate: (Uchida et al., 2016b) and CO_2 hydrate: (Uchida et al., 2020)), the C_3H_8-hydrate formation required tens of hours (**Figure 4**). The longer induction time indicates that C_3H_8 hydrate has a larger energy barrier for crystal formation than other gas hydrates. As a consequence, the promoting effect for C_3H_8 hydrate has greater importance for controlling the hydrate-formation processes. **Figure 4** also shows induction times are nearly halved in the C_3H_8-hydrate dissociated water and C_3H_8-UFB-included water over that in pure water. This result shows a strong promoting effect from using C_3H_8 UFBs.

Given the stochastic behavior of crystal formation, we repeated the induction-time measurements 11 times under the same conditions, determining the probability distributions as done in Sowa and Maeda (2015). We show the resulting induction time series in **Figure 5** as probability nucleation rate curves. This figure shows that both nucleation rate curves of the C_3H_8-hydrate dissociated water (▲) and of the C_3H_8-UFB-included water (♦) are shifted to shorter induction times than that of pure water (■). Thus, both types of liquid samples containing C_3H_8 UFBs exhibit a promoting effect and follow nearly identical curves. In addition, the formation probability within 50 h was 0.8 in both C_3H_8-UFB containing solutions, about 1.3 times that found for pure water.

Concerning the relatively long induction times of C_3H_8-hydrate, the difficulty of formation had been explained by the labile-cluster nucleation hypothesis and assumed that it was in the "difficulty of producing $5^{12}6^4$ cavities" (Christiansen and Sloan, 1994; Sloan and Koh, 2007). Thus, if the memory effect of C_3H_8 hydrate is explained using the water structuring theory, the induction time with C_3H_8-hydrate dissociated water should be significantly shorter than that with UFB-included water, as the latter has not experienced any hydrate structure. However, the results show that both samples exhibit a similar promoting effect. We conclude that the presence of UFBs, which is a common feature of both aqueous solutions, had a dominant effect on the exhibition of the memory effect of C_3H_8 hydrate. Thus, as we found earlier (Uchida et al., 2016a,b, 2020), this conclusion supports the guest dissolution hypothesis for the memory effect on C_3H_8 hydrates, not the water structuring hypothesis.

We now analyze the promoting effect of C_3H_8 hydrate more quantitatively. To compare the fitting parameters with those obtained in previous studies (Takeya et al., 2000; Uchida et al., 2016b, 2020), we fit the normalized nucleation probability $P(t)$ curves of **Figure 5** to

$$P(t) = 1 - \exp[-J(t - \tau_0)], \quad (1)$$

TABLE 2 | Nucleation probability parameters (Equation 1).

Sample	τ_0 [h]	J [$\times 10^{-2}$ h^{-1}]	$< \Delta t_{ind} >$ [h]
C_3H_8-UFB-included water	−1.8	7.78 ± 1.09	14.1
C_3H_8-hydrate dissociated water	−5.9	4.48 ± 1.00	16.9
Pure water	−4.2	2.03 ± 0.41	—

where J is the nucleation rate and τ_0 the offset time. **Table 2** shows the resulting fits. The resulting values of τ_0 are small and negative, indicating that most of the nucleation occurs at an early stage compared to other long induction times. The fits in **Table 2** also show that the nucleation rate J is larger in both C_3H_8-hydrate dissociated water and UFB-included water than that in pure water. However, compared to the rate increase by factors of 100 and 110 for C_2H_6 hydrate (Uchida et al., 2016b), these increases are only factors of about 2.2 times and 3.8 times, respectively, compared to that with pure water.

To quantify the promoting effect, we estimate the expected induction time $<\Delta t_{ind}>$ following the method of Sowa and Maeda (2015) and Uchida et al. (2016b). We compare the difference of areas below the nucleation probability curves between the test water and pure water (**Figure 5**). The resulting values give the magnitude on the promoting effect of C_3H_8-hydrate dissociated water and C_3H_8-UFB-included water. As shown in the last column of **Table 2**, these two aqueous solutions have nearly the same value, which is consistent with the results obtained for C_2H_6 hydrate (Uchida et al., 2016b). The reason why the data and the curve do not fit well is considered to be mainly the small number of data. The additional number of experiments under the same condition would provide better solution in the future studies.

The above comparisons show that the UFBs exhibit the memory effect in C_3H_8 hydrate. Given that the nucleation of C_3H_8 hydrate is much more difficult than those of other gases, the exhibition of a promoting effect can be significant. For example, for C_2H_6 hydrate, the time at which the nucleation probability reaches 1 is about 1.2 h in pure water (Uchida et al., 2016a) and about 0.7 h for CO_2 hydrate (Uchida et al., 2020), whereas for C_3H_8 hydrate, the probability of formation was as low as 0.6 even for 50 h. With the promoting effect of UFBs, the time for nucleation of C_2H_6 hydrate is shorter by only about 15 min (Uchida et al., 2016a), whereas for C_3H_8 hydrate the time was shorter by more than 20 h. In this way, the use of UFB-containing water is a promising way to promote those gas hydrates that are difficult to nucleate.

Roles of UFBs on the Promoting Effects of C_3H_8 Hydrates

The stability measurements indicate that the UFBs remained in high concentration ($\sim 10^8$ mL^{-1}) even after 50 h and stored at room temperature, we argue that they have a role in the promotion effect on C_3H_8 hydrate.

As the nucleation of gas hydrates occurs preferentially at the gas-liquid interface (Sloan and Koh, 2007), the induction time should be shorter in water with a much larger interface area,

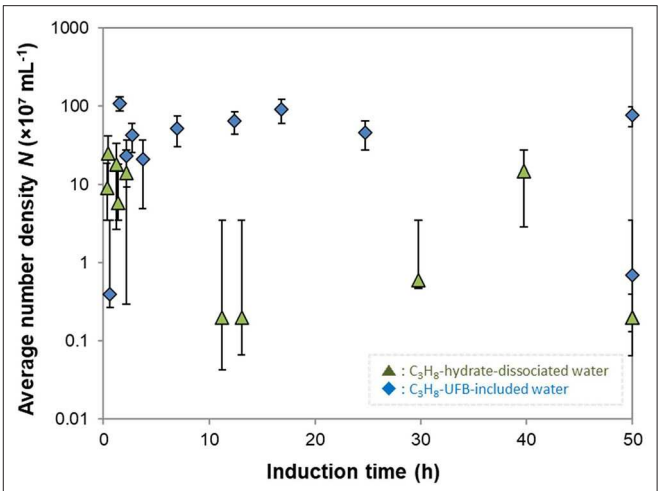

FIGURE 6 | Average number density of UFBs N and induction times. Error bars show the standard deviation of measured number densities ($n > 16$).

that is, one containing many UFBs. The nucleation probability in **Figure 5** shows that C_3H_8 hydrates are formed at a higher rate in the narrow Δt range in the UFB-containing waters. This is associated with the increase of value of J. The increase of J is also observed in other gas hydrate systems with UFBs (Uchida et al., 2016a, 2020). Thus, we assume that the gas-hydrate formation involves heterogeneous nucleation on the gas-liquid interface as argued previously.

To further investigate the roles of UFBs on hydrate formation, we measured the number density of UFBs in the aqueous solutions by the LS method prior to the formation experiments. **Figure 6** shows the dependence of the induction time on the number density of larger UFBs (>300 nm). This figure shows that the aqueous solutions contained UFBs with a number density N of 10^6 to 10^9 mL^{-1}. This figure also shows that the induction time does not clearly depend on N. This result suggests that the hydrate-formation process is not limited by the total area of the gas-liquid interface from the population of UFBs. Thus, the gas-liquid interface appears crucial for nucleation, but its total area is not a key parameter. An explanation for this behavior was proposed by Lipenkov (2000) who suggested that the hydrate nucleation would preferentially occur at a certain size of bubble. In his investigation of air-hydrate distributions in the ice matrix retrieved from a deep ice sheet in Antarctica, he proposed a nucleation process in which air-hydrate crystals transformed from air bubbles smaller than a critical size. Testing this hypothesis requires both a greater number of hydrate formation tests under the same conditions and the actual size distribution of UFBs in each liquid sample over the diameter range from 10^{-9} to 10^{-5} m. However, both of them are unfortunately difficult at present. As suggested by our results in **Figure 3**, it is still difficult to obtain the combined size distribution of UFBs obtained by FFT observations and by PTA measurements. Further quantitative investigations are needed.

CONCLUSION

To help improve the technology for producing gas hydrate, we investigated the promoting mechanism for the memory effect on propane (C_3H_8) hydrate. C_3H_8 is the main component of LPG, and an important component of natural gas, so its control technology is very important. However, C_3H_8 hydrate is difficult to form from pure water and pure C_3H_8 gas. This difficulty was reconfirmed in the present study. In particular, the nucleation probability within 50 h was about 0.6, much lower than that found previously for ethane (C_2H_6) hydrates. Therefore, the development of the formation-promotion technology on C_3H_8 hydrate is important.

We found that a key factor in the promoting effect is the presence of ultra-fine bubbles (UFBs). As had been found previously from dissociation of CH_4 and C_2H_6 hydrates, the dissociation of C_3H_8-hydrate produced a similar amount of UFBs. Thus, UFBs have been found in both the dissociation of sI-type hydrates (CH_4 and C_2H_6) and sII-type hydrate (C_3H_8). Concerning these UFBs, their number density tended to decrease with time, likely controlled by the saturation condition with guest gas in water. However, the fraction remaining within 50 h was at least 0.4, with more than 10^7 mL^{-1} remaining in water after 50 h.

We compared the memory effect on C_3H_8 hydrates between two C_3H_8-UFB containing waters, specifically, C_3H_8-hydrate dissociated water and C_3H_8-UFB-included water prepared by an UFB generator. Based on 11 experiments with C_3H_8-hydrate formation, we found that the nucleation probability within 50 h was 1.3 times larger than that of the case with pure water, and that the induction time was shortened by nearly half. Therefore, we confirmed that UFB-containing water promoted the formation of C_3H_8 hydrates, with the two types of UFB-containing water giving nearly the same nucleation probability curve. We argued that this similarity does not support the idea that the promotion is due to a hydrate-memory structure in the water. In addition, we found little correlation between the initial UFB number density and nucleation probability. Therefore, we argue that the memory effect of gas hydrates arises from the existence of guest-gas UFBs, which are mainly playing a role as the guest-gas supplying source, thus supporting the gas dissolution hypothesis.

DATA AVAILABILITY STATEMENT

The raw data supporting the conclusions of this article will be made available by the authors, without undue reservation.

AUTHOR CONTRIBUTIONS

TU, KY, and KG contributed conception and design of the study. AS performed the statistical analysis. TU wrote the first draft of the manuscript. TU, HM, and RS wrote sections of the manuscript. All authors contributed to manuscript revision, read and approved the submitted version.

FUNDING

This work was partly supported financially by the Tonen General Sekiyu Research/Development Encouragement & Scholarship Foundation. The TEM observations were supported by the Hokkaido University Microstructure Characterization Platform's facility.

ACKNOWLEDGMENTS

The authors acknowledge the technical supports of TEM observations by Drs. N. Sakaguchi, and T. Tanioka (Hokkaido Univ.). PTA measurements were supported by Prof. K. Kimura, Mr. S. Kiuchi and Mr. H. Fernandes (Hokkaido Univ.). The authors also acknowledge the fruitful discussion in the Joint Research Program of the Institute of Low Temperature Science, Hokkaido University.

REFERENCES

Bagherzadeh, S. A., Alavi, S., Ripmeester, J. A., and Englezos, P. (2015). Formation of methane nano-bubbles during hydrate decomposition and their effect on hydrate growth. *J. Chem. Phys.* 142:214701. doi: 10.1063/1.4920971

Buchanan, P., Soper, A. K., Thompson, H., Creek, J. L., Hubson, G., and Koh, C. A. (2005). Search for memory effects in methane hydrate: structure of water before hydrate formation and after hydrate decomposition. *J. Chem. Phys.* 123:164507. doi: 10.1063/1.2074927

Christiansen, R. L., and Sloan, E. D. Jr. (1994). Mechanisms and kinetics of hydrate formation. *Ann. NY Acad. Sci.* 715, 283–305. doi: 10.1111/j.1749-6632.1994.tb38841.x

Giavarini, C., Maccioni, F., and Santarelli, M. L. (2003). Formation kinetics of propane hydrates. *Ind. Eng. Chem. Res.* 42, 1517–1521. doi: 10.1021/ie0207764

Gudmundsson, J., and Borrehaug, A. (1996). Frozen hydrate for transport of natural gas. *Proc. ICGH* 2, 415–422.

Horiguchi, K., Watanabe, S., Moriya, H., Nakai, S., Yoshimitsu, A., and Taoda, A. (2011). "Completion of natural gas hydrate (NGH) overland transportation demo project," in *Proceedings of 7th International Conference* (Edinburgh: Natural Gas Hydrates), 17–21.

Hwang, M. J., Wright, D. A., Kapur, A., and Holder, G. D. (1990). An experimental study of crystallization and crystal growth of methane hydrates from melting ice. *J. Inclusion Phenom. Molecul. Recogn. Chem.* 8, 103–116. doi: 10.1007/BF01131291

Ida, H., and Kohda, K. (2004). *Highly Efficient Natural Gas Hydrate Production Technology*. JFE Technical. Report No. 6, 76–80 (in Japanese with English abstract).

ISO 20408-1:2017. (2017). *Fine Bubble Technology - General Principles for Usage and Measurement of Fine Bubbles - Part 1: Terminology* . Available online at: https://www.iso.org/standard/68187.html?browse$=$tc (accessed Febuary 27, 2020).

Kvenvolden, K. A. (1988). Methane hydrate - a major reservoir of carbon in the shallow geosphere? *Chem. Geol.* 71, 41–51. doi: 10.1016/0009-2541(88)90104-0

Lipenkov, V. Y. (2000). "Air bubbles and air-hydrate crystals in the vostok ice core," in *Physics of Ice Core Records*. ed T. Hondoh (Sapporo: Hokkaido Univ. *Press)*, 327–358.

Masuda, Y., Uchida, T., Nagakubo, S., and Satoh, M. (2016). "Methane hydrates," in *Fossil Fuels: Current Status and Future Directions, World Scientific Series in Current Energy Issues,* ed G. M. Crawley (Singapore: World Scientific Pub. Co. Pte. Ltd.), 289–327. doi: 10.1142/9789814699983_0010

Mimachi, H., Takeya, S., Yoneyama, A., Hyodo, K., Takeda, T., Gotoh, Y., et al. (2014). Natural gas storage and transportation within gas hydrate of smaller particle: size dependence of self-preservation phenomenon of natural gas hydrate. *Chem. Eng. Sci.* 118, 208–213. doi: 10.1016/j.ces.2014.07.050

Ohmura, R., Ogawa, M., Yasuoka, K., and Mori, Y. H. (2003). Statistical study of clathrate-hydrate nucleation in a water/hydrochlorofluorocarbon system: search for the nature of the "memory effect". *J. Phys. Chem. B* 107, 5289–5293. doi: 10.1021/jp027094e

Oshita, S., and Uchida, T. (2013). "Basic Characterization of nanobubbles and its potential applications," in *Bio-Nanotechnology: a Revolution in Biomedical Sciences, and Human Health. eds D. Bagchi, M. Bagchi, H. Moriyama, and F. Shahidi (West Sussex, UK: John Wiley and Sons, Ltd.),* 506–516. doi: 10.1002/9781118451915.ch29

Parent, J. S., and Bishnoi, P. R. (1996). Investigation into the nucleation behavior of methane gas hydrates. *Chem. Eng. Commun.* 144, 51–64. doi: 10.1080/00986449608936444

Ripmeester, J. A., and Alavi, S. (2016). Some current challenges in clathrate hydrate science: nucleation, decomposition and the memory effect. *Curr. Opin. Solid State Mater. Sci.* 20, 344–351. doi: 10.1016/j.cossms.2016.03.005

Rodger, P. M. (2000). Methane hydrate, melting and memory. *Ann. N.Y. Acad. Sci.* 912, 474–482. doi: 10.1111/j.1749-6632.2000.tb06802.x

Seddon, J. R. T., Lohse, D., Ducker, W. A., and Craig, V. S. J. (2012). A deliberation on nanobubbles at surfaces and in bulk. *ChemPhysChem* 13, 2179–2187. doi: 10.1002/cphc.201100900

Sefidroodi, H., Abrahamsen, E., and Kelland, M. A. (2013). Investigation into the strength and source of the memory effect for cyclopentane hydrate. *Chem. Eng. Sci.* 87, 133–140. doi: 10.1016/j.ces.2012.10.018

Sloan, E. D. (2004). Fundamental principles and applications of natural gas hydrates. *Nature* 426, 353–363. doi: 10.1038/nature02135

Sloan, E. D., and Koh, C. A. (2007). *Clathrate Hydrate of Natural Gases, 3rd Edn. Boca Raton, FL: CRC Press*. doi: 10.1201/9781420008494

Sowa, B., and Maeda, N. (2015). Statistical study of the memory effect in model natural gas hydrate systems. *J. Phys. Chem. A* 119, 10784–10790. doi: 10.1021/acs.jpca.5b07308

Takahashi, M. (2005). ζ potential of microbubbles in aqueous solutions: electrical properties of the gas-water interface. *J. Phys. Chem. B* 190, 21858–21864. doi: 10.1021/jp0445270

Takeya, S., Hori, A., Hondoh, T., and Uchida, T. (2000). Freezing-memory effect of water on nucleation of CO2 hydrate crystals. *J. Phys. Chem. B* 104, 4164–4168. doi: 10.1021/jp993759+

Takeya, S., Mimachi, H., and Murayama, T. (2018). Methane storage in water frameworks: self-preservation of methane hydrate pellets formed from NaCl solutions. *Appl. Energy* 230, 86–93. doi: 10.1016/j.apenergy.2018.08.015

The Chemical Society of Japan (2004). *Kagaku-binran Handbook of Chemistry, 5th Edn. Tokyo: Maruzen Co. Ltd.* 144–149.

Uchida, T., Liu, S., Enari, M., Oshita, S., Yamazaki, K., and Gohara, K. (2016c). Effect of NaCl on the lifetime of micro- and nanobubbles. *Nanomaterials* 6:31. doi: 10.3390/nano6020031

Uchida, T., Miyoshi, H., Yamazaki, K., and Gohara, K. (2020). "Effects of ultra-fine bubbles on exhibiting the memory effect," in *Proceedings of 10th Interenational Conference* (Singapore: Natural Gas Hydrates).

Uchida, T., Yamazaki, K., and Gohara, K. (2016a). Generation of micro- and nano-bubbles in water by dissociation of gas hydrates. *Korean J. Chem. Eng.* 33, 1749–1755. doi: 10.1007/s11814-016-0032-7

Uchida, T., Yamazaki, K., and Gohara, K. (2016b). Gas nano-bubbles as nucleation acceleration in the gas-hydrate memory effect. *J. Phys. Chem. C* 120, 26620–26629. doi: 10.1021/acs.jpcc.6b07995

Uchida, T., Yamazaki, K., and Gohara, K. (2017). "Generation of gas nano-bubbles by gas hydrate dissociation and its effect on the memory effect," in *Proceedings of 10th Interenational Conference* (Denver, CL: Natural Gas Hydrates).

Yagasaki, T., Matsumoto, M., Andoh, Y., Okazaki, S., and Tanaka, H. (2014). Effect of bubble formation on the dissociation of methane hydrate in water: a molecular dynamic study. *J. Phys. Chem. B* 118, 1900–1906. doi: 10.1021/jp412692d

Zeng, H., Moudrakovski, I. L., Ripmeester, J. A., and Walker, V. K. (2006). Effect of antifreeze protein on nucleation, growth and memory of gas hydrates. *AIChE J.* 52, 3304–3309. doi: 10.1002/aic.10929

Conflict of Interest: The authors declare that the research was conducted in the absence of any commercial or financial relationships that could be construed as a potential conflict of interest.

NOMENCLATURE

D	Average diameter of UFBs
J	Nucleation frequency
N	Number density of UFBs
τ_0	Offset time
$< \Delta t_{ind} >$	Expected induction time
$P(t)$	Normalized nucleation probability by time t

frontiers in Chemistry

MINI REVIEW
published: 16 June 2020
doi: 10.3389/fchem.2020.00464

Enhancement of Clathrate Hydrate Formation Kinetics Using Carbon-Based Material Promotion

Yuan-Mei Song[1], Ru-Quan Liang[1], Fei Wang[2], Jian-Hui Shi[1], Deng-Bo Zhang[1] and Liu Yang[1]*

[1] The School of Mechanical & Vehicle Engineering, Linyi University, Linyi, China, [2] Shandong Engineering Laboratory for Preparation and Application of High-Performance Carbon-Materials, College of Electromechanical Engineering, Qingdao University of Science & Technology, Qingdao, China

Although hydrate-based technology has been considered as a safe and environmentally friendly approach for gas storage and transportation in recent decades, there are still inherent problems during hydrate production, such as a long induction time, slow formation kinetics, and limited hydrate storage capacity. Attempts to resolve these issues have resulted in the development of various kinetics promoters, among which carbon-based materials have become one of the most attractive owing to their unique promotion effect. Herein, results on promotion by bulk wetted carbon materials in the forms of a packed bed, carbon particles in a suspension, and nano-carbon materials in a nanofluid are collected from the published literature. Meanwhile, the promotion mechanisms and influencing factors of the carbon-based promoters are discussed. The purpose of this mini-review is to summarize recent advances and highlight the prospects and future challenges for the use of carbon-based materials in hydrate production.

Keywords: gas hydrates, methane storage, efficient promoter, carbon-based materials, kinetic promotion

OPEN ACCESS

Edited by:
Xi Zhang,
Shenzhen University, China

Reviewed by:
Siddharth Surajbhan Gautam,
The Ohio State University, United States
Jean-Marc Simon,
Université de Bourgogne, France

****Correspondence:***
Yuan-Mei Song
songyuanmei@lyu.edu.cn

Specialty section:
This article was submitted to Physical Chemistry and Chemical Physics, a section of the journal Frontiers in Chemistry

Received: *16 February 2020*
Accepted: *04 May 2020*
Published: *16 June 2020*

Citation:
Song Y-M, Liang R-Q, Wang F, Shi J-H, Zhang D-B and Yang L (2020) Enhancement of Clathrate Hydrate Formation Kinetics Using Carbon-Based Material Promotion. Front. Chem. 8:464. doi: 10.3389/fchem.2020.00464

INTRODUCTION

Natural gas hydrate, also referring to the methane hydrate, is an ice-like clathrate constituted by hydrogen-bonded water molecules and light molecules like methane that have filled in the cavities via Van der Waals force (Sloan, 1998). This solidified natural gas (SNG) has been viewed as a potential alternative for natural gas transportation and storage because of several advantages (Thomas, 2003; Javanmardi et al., 2005; Koh et al., 2011; Veluswamy et al., 2018): the high volumetric storage capacity of 160–180 v/v, much milder formation and storing conditions than CNG and LNG, e.g., at 273.15 K and 3.2 MPa for methane hydrate formation, and safe and environmentally benign manufacturing process. However, technical challenges arise in the production process, primarily the slow kinetics of hydrate formation, large amount of heat generated, and limited gas storage capacity. Hydrate formation is always accompanied by heat release, which will impede hydrate growth if the heat is not removed in time, particularly in large-scale industrialization. Moreover, the theoretical gas storage capacity is hard to achieve due to the retarded mass transfer caused by the formation of thin hydrate layers at gas–liquid interfaces (Lee et al., 2006; Aman and Koh, 2016).

A great deal of effort has been focused on developing efficient methods for overcoming the above issues. To date, the most well-studied field is the formation of methane hydrates in the presence of surfactant, among which sodium dodecyl sulfate (SDS) showed the best performance (Zhong and Rogers, 2000; Kumar et al., 2015). In a recent review article, He et al. He et al. (2019) have provided a good review of surfactant-promoted gas hydrate formation during the past three decades. Given the enormous amount of foam production in hydrate dissociation and the difficulty of recycling the surfactant, non-surfactant-based methods for improving hydrate formation have attracted growing attention over the last 10 years. A review by Veluswamy et al. (2018) documented and discussed in detail the different materials applied for methane hydrate formation, e.g., silica gel, dry water, dry gel, sand, zeolite, and hollow silica, which are used as a fixed bed for hydrate reaction. Another review conducted by Nashed et al. (2018) shed light on the nanomaterials for gas hydrate formation, where various metal-based particles, like nano-Ag, Cu, CuO, and ZnO were discussed, and it was concluded that nanoparticles not only could help to promote mass transfer but they could also contribute to heat transfer enhancement in the hydrate reaction. Additionally, some non-metal materials such as silica nanoparticles (Wang et al., 2019), graphene (Wang et al., 2017), and carbon nanotubes (Pasieka et al., 2014) exhibited excellent performance in promoting gas storage capacities and hydrate formation rate.

As carbon-based materials (e.g., activated carbon, graphite, graphene, and carbon nanotubes) have been widely employed in gas hydrate formation in recent years, this mini-review summarizes the published studies where the promotion effects of carbon-based materials on gas hydrate formation were investigated. With an attempt to draw critical conclusions after compiling this knowledge into a single article, this review provides significant guidance for developing novel methods for hydrate-based technology.

GAS HYDRATE FORMATION WITH CARBON-BASED MATERIALS

Porous carbon-based materials, such as active carbon, graphite, carbon nanotubes, and graphene, can realize gas adsorption due to their porosity and high specific areas when utilized for hydrogen or methane storage (Nikitin et al., 2008; Mohan et al., 2019). During research on the gas adsorption process, scientists discovered that when carbon materials were wetted by water or dispersed in water, a higher methane storage capacity was obtained via hydrate formation under certain conditions. Hence, carbon materials attracted research interest as efficient promoters for the gas hydrate formation, resulting in numerous investigations in the last 10 years. Referring to the literature concerning different kinds of carbon materials, this section is divided into three parts: the promotion of gas hydrate formation by bulk carbon materials, carbon-based suspensions, and carbon-based nanofluid, respectively.

Gas Hydrate Formation With Bulk Carbon Materials

Since natural gas hydrates are usually stored within porous sediments in nature, it is essential to understand the characteristics of hydrate formation in porous space. In experiments, the reactor is often filled with bulk materials with adsorbed water in the form of a packed bed for hydrate formation. The mass ratio of water to bulk materials, the material types, and the pore size are the primary factors that affect the gas hydrate formation rate and storage capacity.

The literature regarding the use of porous carbon materials (mainly referring to activated carbon) in methane hydrate formation is listed in chronological order in **Table 1A**. The porous material first reported as being for hydrate formation was active carbon, in an investigation by Zhou and Sun (2001). They found that wet activated carbon caused an increase in methane adsorption isotherms and enhanced gas uptake by 60% at a water ratio of 1.4. Later on, many studies proved the optimal water/carbon mass ratio to be about 1 (Perrin et al., 2003; Yan et al., 2005; Celzard and Marêché, 2006). By analysis of pore styles, Perrin et al. found that microporosity seemed to be useless for clathrate formation, while mesoporous and macroporous carbon materials were more favorable to enhancing hydrate formation. Following this work, Celzard and Marêché (2006) proved, however, that saturated pore space would slow down the hydrate formation kinetics since gas diffusion pathways became scarce when the small spaces in the pore network were filled by water. Similarly, another study showed that a 96.5% enhancement of water conversion was obtained due to the larger interstitial pore space between activated particles than between other smaller particles under 8 MPa and 4°C (Siangsai et al., 2015). Via observation of the morphology of methane hydrate formed in porous media of activated carbon, Babu et al. (2013) confirmed that the hydrates primarily nucleated on the surface of the activated carbon and that whether the hydrates further developed into stable hydrate crystals depended on the interstitial space between the activated carbon particles. As a consequence, porous activated carbons with an optimal water ratio can provide excellent interfaces that enlarge the area of gas–liquid contact for hydrate nucleation and growth, and the hydrate formation process is only accelerated by active carbons with large pore size rather than micropores.

Aiming to determine the critical hydrate formation conditions, phase equilibrium estimations of gas hydrate formation in porous carbon materials have been conducted in many experimental or theoretical studies. The methane hydrate equilibrium was usually shifted to a higher pressure or lower temperature in bulk carbons compared to pure water (Najibi et al., 2008; Mingjun et al., 2010; Yang et al., 2012). For example, Liu et al. (2018) measured the methane hydrate formation or dissociation conditions in eleven porous materials, verifying that smaller pores size (below 6.2 nm) exerted a negative influence on the hydrate formation conditions due to extra capillary pressure in these pores. Taking the pore size, pore distribution, capillary pressure, and hydrate–liquid interfacial tension into consideration, some new equilibrium models were established

TABLE 1 | List of the carbon-based materials used in methane hydrate formation.

Carbon material	Pore size (nm)	SSA (m^2/g)	R_w	T (K)	P (MPa)	References
(A)-FOR BULK CARBON-BASED MATERIALS						
Activated carbon	-	1,800	1.4	275	4.6	Zhou and Sun, 2001
NC58	-	1,000	1.0	275.15	8	Perrin et al., 2003
NC86		1,257				
NC120		2,031				
Picazine		1,967				
Activated carbon	1.9	978, 1,126	1.7, 2.9	278	8	Yan et al., 2005
Activated carbon	-	1,000, 1,587, 2,031	1.09, 0.72, 0.85	275.15	8	Celzard and Marêché, 2006
NC120	-	2031	1.0	277.15	10	Najibi et al., 2008
Picazine		1967				
Activated carbon	2.19	866.7	0.5, 1.0	277.15	8	Babu et al., 2013
Activated carbon	-	864–918	1.0	277.15	6 or 8	Siangsai et al., 2015
Activated carbon	1.5	-	0.3	-	10	Liu et al., 2018

Particles	Concentration	T (K)	P (MPa)	Duration (min)	Storage efficiency improvement	References
(B) FOR CARBON NANOTUBE-BASED NANOFLUID						
OCNTs	0.001–0.006%	274.15	3&4	720	375%	Park et al., 2012
OCNTs	0.001–0.006%	274.15	-	720	260%	Pasieka et al., 2013
OCNTs	1×10^{-6}–1×10^{-4}%	275.15	4.7	-	-	Lim et al., 2014
SDS@ CNTs	0.05–0.6 mg/L	275.15	6	100	600%	Song Y. et al., 2017
RR195@CNTs	2–40 ppm	275.15	6	203	250%	Song et al., 2019
f-CNTs	10–150 ppm	275.15	6	100	575%	Song Y. M. et al., 2017
Ag@ OCNTs	20 ppm	275.15	6	110	650%	Song et al., 2018

R_w is the mass ratio of water to carbon; "-" means "not found"; SSA refers to specific surface area; P and T are the pressure and temperature respectively; the storage efficiency improvement was calculated based on a pure water system.

and also supported the experimental results (Zhang et al., 2020).

The addition of a traditional promoter such as a surfactant or thermodynamic promoter into the water or offering hydrophobic/hydrophilic groups on the carbon surface have proved to be efficient ways of improving gas storage capacity and the hydrate formation rate in porous media (Casco et al., 2017; Cuadrado-Collados et al., 2020; Palodkar and Jana, 2020; Zhang et al., 2020). In the latest research, Cuadrado-Collados et al. (2020) reported the promotion effects of various additives, such as the sodium dodecyl sulfate (SDS), leucine, and tetrahydrofuran (THF) in the confined nanospace of the carbon surface, where hydrate nucleation and growth rate were both accelerated significantly. A similar work was conducted by Zhang et al. (2020), who noted that, when anionic active groups aggregated onto the surface of the porous media, the modified carbon could promote gas adsorption and enhance formation process because of micellar solubilization in the presence of SDS. By introducing oxygen-containing groups on the activated carbon, the carbons performed better after being wetted by water, as shown by the result that the methane hydrate yield was elevated to 51% for oxidation-treated carbons under the conditions of 3.3 MPa and 2°C. It was assumed that the locations of the oxygen groups on the surfaces of carbons acted as nucleation centers for water clustering, which benefited further hydrate growth (Casco et al., 2017). Herein, after functionalization or being attached to other promoters, porous carbon materials provided more efficient reaction media for hydrate formation.

There are two basic kinds of promotion mechanism for hydrate formation in wetted porous carbon materials. The generally accepted mechanism is the interface adsorption theory (Zhou and Sun, 2001; Mingjun et al., 2010; Cuadrado-Collados et al., 2018; Andres-Garcia et al., 2019). Unlike in the gas–free water system, there are many voids among and inside the carbon particles when water is absorbed in porous activated carbon, and these will provide efficient contact areas for gas and water. The hydrate formation process can then be described as: liquid water films gradually form at the surface of the carbon interface, followed by hydrate formation after gas adsorption at the water–carbon interface. This theory also points out that methane

hydrates tend to form in wider pores and the intersectional spaces between particles. Another promotion mechanism is the capillary effect caused by the pores or interstitial space in the porous media. As the capillary force can enhance liquid phase migration in the pores, continuous gas–liquid contact is realized, and hydrate formation distributions are changed constantly. This promotion mechanism became more obvious when surfactant was added to the porous materials (Zhang et al., 2020). However, in this light, a minimum pore size of about 3 nm is required for methane hydrate formation considering the hydrate crystal size. Conversely, in some cases, the pore capillary force was assumed to reduce the activity of the pore-confined water that hindered hydrate formation (Liu et al., 2018).

Gas Hydrate Formation With Carbon-Based Suspensions

Suspensions formed by carbon particles in an aqueous solution are considered another potential reaction medium for rapid hydrate formation (Takahata et al., 2010; Govindaraj et al., 2015; Yu et al., 2016, 2018). In case of severe sedimentation of hydrophobic particles in the reaction system, mechanical agitation is necessary during the hydrate formation. A carbon-based suspension is preferable to bulk materials in a fixed bed as the hydrate reaction system, since there are three distinct advantages when particles are dispersed in a liquid phase: the greater gas–liquid contact area of stirred suspensions, a more uniformly distributed hydrate crystallization process, and the feasibility of a continuous production process (Govindaraj et al., 2015).

By investigating methane hydrate formation kinetics in an activated carbon particle suspension at loadings of 0.5, 1.0, and 2.0 wt%, Govindaraj et al. elucidated that suspensions with a higher fraction of activated carbon particles had stronger promotion effects on hydrate formation kinetics (Govindaraj et al., 2015). Meanwhile, a prominent positive correlation was established between the activated carbon concentration and the hydrate gas storage capacity, where the gas storage capacity was increased by 60% in a 2.0 wt% suspension compared to a pure water system. Although in several studies, the graphite had marginal promotion effects on methane hydrates, mixtures of graphite and other promoters, e.g., a mixture of graphite and hematite or a mixture of graphite and surfactant could lead to rapid hydrate formation (Takahata et al., 2010; Yu et al., 2016). Carbon nanotubes, in particular, attracted most interest for the excellent thermal properties reported in some literature. By adding multi-walled or single-walled carbon nanotubes to pure water, the gas consumption and hydrate reaction rate during hydrate formation were dramatically improved (Park et al., 2010). A comparative study on the enhanced formation of methane hydrate by different types of CNTs indicated that a shorter nucleation stage and more rapid growth process were obtained when short nanotubes (CM-95) rather CM-100 were applied as additives as a result of the larger specific area of the shorter MWCNTs (Kim et al., 2011).

In summary, carbon particle suspensions have obvious promotion effects on gas hydrate formation. The primary reason for this is the enlarged gas–liquid contact area provided by suspended particles, which leads to a mass transfer enhancement. However, it is noted that hydrate formation must be carried out with the aid of stirring, and it thus requires extra energy consumption and the use of an agitation apparatus.

Gas Hydrate Formation With Carbon-Based Nanofluid

Nanofluid is actually a stable dispersion formed by nanoparticles dispersed homogeneously in an aqueous phase. Nanofluid is considered an excellent hydrate reaction medium based on its superior mass transfer and heat transfer properties (Li et al., 2017; Nashed et al., 2018). The behaviors of nanoparticles in nanofluid that promote hydrate formation are as follows. Firstly,

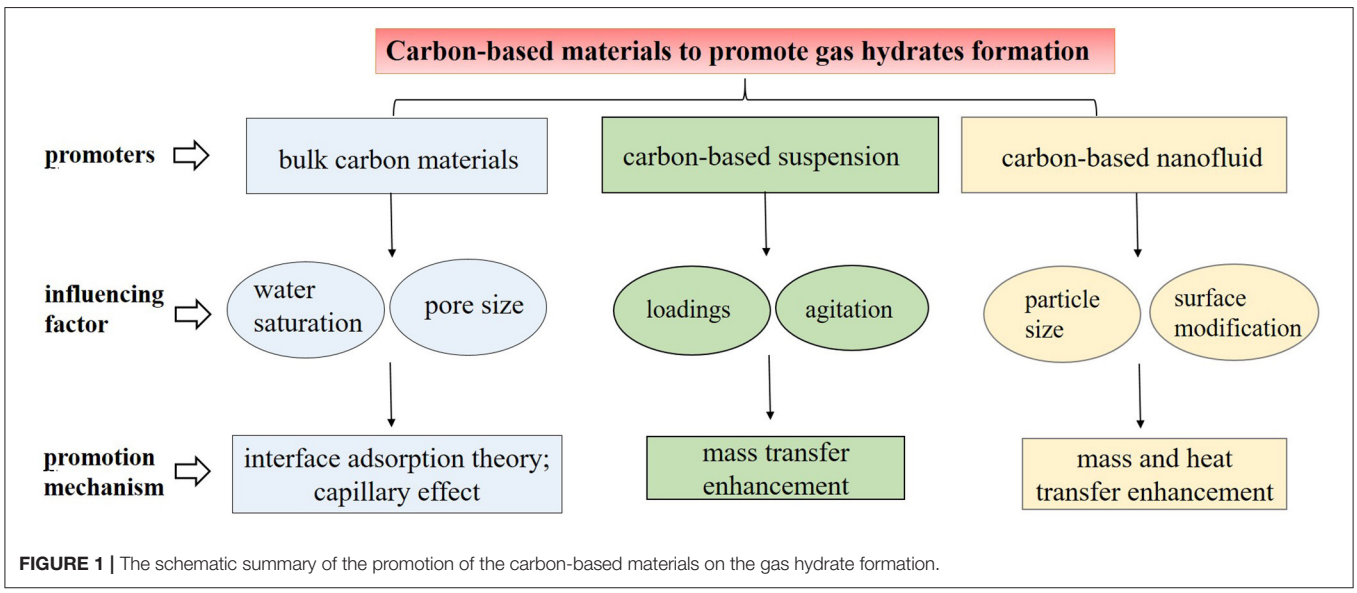

FIGURE 1 | The schematic summary of the promotion of the carbon-based materials on the gas hydrate formation.

the nanoparticles move like microstirrers in the liquid through Brownian motion, resulting in constant updating of the gas–liquid interface. Secondly, the nanoparticles have high specific surface areas and can thus offer plenty of nucleation sites for hydrate formation. Lastly, the continuous movement of carbon nanoparticles helps to remove the heat generated during hydrate formation. Carbon nanomaterials such as carbon nanotubes and graphene are more beneficial to heat transfer due to their intrinsic high thermal conductivity.

Nanofluid constituted by water-soluble carbon nanotubes has been verified to be an excellent promoter for gas hydrate formation (as listed in **Table 1B**). When an oxidized CNT nanofluid was used as the reaction system, the gas consumption was up to 4.5 times higher than in water (Park et al., 2012; Li et al., 2017). The promotion efficiency of chemically or physically treated CNT nanofluid exceeded that of pristine CNTs. For instance, acid-treated CNTs, SDS-coated CNTs and plasma-functionalized CNTs could efficiently reduce induction time, increase gas consumption, and enhance growth rate (Park et al., 2010; Pasieka et al., 2013, 2015). The promotion efficiency of the CNT-based nanofluid, however, is affected by the particle fraction, the surface functional groups, and the treatment methods. The best concentration of OCNTs for promoting the growth of methane hydrate was 0.003% in Park et al. (2010). In view of the marked reactivity of the sulfonate groups contained in SDS, some researchers have coated the CNT surfaces with SDS, long-chain polymers containing SO_3-, or Reactive Red 195 molecules and then dispersed the CNTs in water for use as the reaction system. Hydrates formed in these nanofluids all exhibited gas storage capacities that were elevated to 140–150 v/v, and the hydrate reactions finished within 100 min (Song Y. et al., 2017; Song Y. M. et al., 2017; Song et al., 2019). Moreover, with the aid of a high-speed ball milling process, the obtained functionalized CNTs (such as RR195@CNTs) had excellent recycling performance in the hydrate formation process (Song et al., 2019). Due to the thermal conductivity of metal nanoparticles (nano-Ag or nano-Cu), a prepared compound nanofluid containing OCNTs grafted by metal nanoparticles had a stronger promotion effect than the one-component nanofluid, with the exception that the metal nanoparticle-grafted OCNT nanofluid was not as stable as an OCNT nanofluid (Song et al., 2018).

Since graphene has smooth surfaces and is easy to functionalize by sulfonate groups or to load with metal nanoparticles, this two-dimensional carbon material is also introduced to hydrate formation reactions. Wang et al. (2017) grafted sulfonate groups successfully to graphene by covalent bonding and used it in methane hydrate formation. The results showed that the promotion efficiency of SGO (sulfated graphene) was better than that of GO (oxidized graphene). In another work, nano-Ag coated SGO was prepared for methane hydrate formation, and a shorter hydrate formation stage was achieved compared to SGO (He and Wang, 2018).

Considering that the fraction of carbon nanoparticles in the nanofluid is far smaller, the promotion efficiency of the equivalent carbon-based material in nanofluid is superior to the materials in suspension or a packed bed. Besides, the stable carbon-based nanofluid has excellent recycling performance in repeated hydrate formation, which thus contributes to more economical hydrate production.

CONCLUSION AND PROSPECTS

This work is devoted to the summary of hydrate formation in various carbon media of different forms: porous carbon materials in packed beds, particles in suspension, and nanoparticles in nanofluid. **Figure 1** highlights the themes of this mini review. Porous carbons provide a large interface area for gas-liquid contact, and particles in suspension or nanofluids are helpful for heat and mass transfer enhancement. To sum up, carbon-based materials, either in macro or micro forms, all show unique promotion effects on gas hydrate formation. Carbon-based nanofluid is the preferable medium among these for achieving economical and efficient hydrate production. Accordingly, it is necessary to develop more economical and efficient carbon-based nanofluids via surface modifications or coupling with other promoters. Besides, a majority of current research focuses on experimental investigation, while few works have attempted molecular illustration of the gas hydrates promoted by those carbon materials. Molecular simulation or mathematical modeling to investigate the hydrate formation characteristics and hydrate growth mechanism in carbon-based materials is therefore required, and this would also be helpful for designing and propelling the application of novel carbon materials for hydrate-based technology.

AUTHOR CONTRIBUTIONS

Y-MS was in charge of literature collection, review, and writing. R-QL contributed to the tools and the internet search. FW and D-BZ helped write the manuscript. J-HS and LY assisted with manuscript enhancement. All authors contributed to the article and approved the submitted version.

FUNDING

This work was supported financially by the National Natural Science Foundation of China under the grants 51676031, 51976087, 21706269, and 21978142 and by the Natural Science Foundation of Shandong Province with grant number ZR2018PEE004.

REFERENCES

Aman, Z. M., and Koh, C. A. (2016). Interfacial phenomena in gas hydrate systems. *Chem. Soc. Rev.* 45, 1678–1690. doi: 10.1039/c5cs00791g

Andres-Garcia, E., Dikhtiarenkob, A., Fauthc, F., Silvestre-Alberod, J., Ramos-Fernándezd, E. V., Jorge, G., et al. (2019). Methane hydrates Nucleation in microporous materials. *Chem. Eng. J.* 360, 569–576. doi: 10.1016/j.cej.2018.11.216

Babu, P., Yee, D., Linga, P., Palmer, A., Khoo, B. C., Tan, T. S., et al. (2013). Morphology of methane hydrate formation in porous media. *Energ. Fuel.* 27, 3364–3372. doi: 10.1021/ef4004818

Casco, M. E., Cuadrado-Collados, C., Martínez-Escandell, M., Rodríguez-Reinoso, F., and Silvestre-Albero, J. (2017). Influences of the oxygen-containing surface functional groups in the methan hydrate nucleation and growth in nanoporous carbon. *Carbon* 123, 299–301. doi: 10.1016/j.carbon.2017.07.061

Celzard, A., and Marêché, J. F. (2006). Optimal wetting of active carbons for methane hydrate formation. *Fuel* 85, 957–966. doi: 10.1016/j.fuel.2005.10.019

Cuadrado-Collados, C., Farrando-Pérez, J., Martínez-Escandell, M., Missyul, A., and Silvestre-Albero, J. (2020). Effect of additives in the nucleation and growth of methane hydrates confined in a high-surface area activated carbon material. *Chem. Eng. J.* 338, 124–224. doi: 10.1016/j.cej.2020.124224

Cuadrado-Collados, C., Fauth, F., Such-Basanez, I., Martínez-Escandell, M., and Silvestre-Albero, J. (2018). Methane hydrate formation in the confined nanospace of activated carbons in seawater environment. *Micropor. Mesopor. Mat.* 255, 220–225. doi: 10.1016/j.micromeso.2017.07.047

Govindaraj, V., Mech, D., Pandey, G., Nagarajan, R., and Sangwai, J. S. (2015). Kinetics of methane hydrate formation in the presence of activated carbon and nano-silica suspensions in pure water. *J. Nat. Gas Sci. Eng.* 26, 810–818. doi: 10.1016/j.jngse.2015.07.011

He, Y., Sun, M.-T., Chen, C., Zhang, G.-D., Chao, K., Lin, Y., et al. (2019). Surfactant-based promotion to gas hydrate formation for energy storage. *J. Mater. Chem. A* 7, 21634–21661. doi: 10.1039/c9ta07071k

He, Y., and Wang, F. (2018). Hydrate-based CO_2 capture: kinetic improvement via graphene-carried –SO3- and Ag nanoparticles. *J. Mater. Chem. A* 6, 22619–22625. doi: 10.1039/C8TA08785G

Javanmardi, J., Nasrifar, K., Najibi, S. H., and Moshfeghian, M. (2005). Economic evaluation of natural gas hydrate as an alternative for natural gas transportation. *Appl. Therm. Eng.* 25, 1708–1723. doi: 10.1016/j.applthermaleng.2004.10.009

Kim, N. J., Park, S. S., Kim, H. T., and Chun, W. (2011). A comparative study on the enhanced formation of methane hydrate using CM-95 and CM-100 MWCNTs. *Int. Commun. Heat Mass* 38, 31–36. doi: 10.1016/j.icheatmasstransfer.2010.10.002

Koh, C. A., Sloan, E. D., Sum, A. K., and Wu, D. T. (2011). Fundamentals and Applications of Gas Hydrates. *Annu. Rev. Chem. Biomol.* 22, 237–257. doi: 10.1146/annurev-chembioeng-061010-114152

Kumar, A., Bhattacharjee, G., Kulkarni, B. D., and Kumar, R. (2015). Role of Surfactants in Promoting Gas Hydrate Formation. *Ind. Eng. Chem. Res.* 54, 12217–12232. doi: 10.1021/acs.iecr.5b03476

Lee, J. D., Song, M., Susilo, R., and Englezos, P. (2006). Dynamics of methane–propane clathrate hydrate crystal growth from liquid water with or without the presence of n-heptane. gryst. *Growth Des.* 6, 1428–1439. doi: 10.1021/cg0600647

Li, D. L., Peng, H., and Liang, D. Q. (2017). Thermal conductivity enhancement of clathrate hydrate with nanoparticles. In*t. J. Heat Mass Tran*. 104, 566–573. doi: 10.1016/j.ijheatmasstransfer.2016.08.081

Lim, S. H., Riffat, S. B., Park, S. S., Oh, S.-J., Chun, W., and Kim, N.-J. (2014). Enhancement of methane hydrate formation using a mixture of tetrahydrofuran and oxidized multi-wall carbon nanotubes. *Int. J. Energ. Res.* 38, 374–379. doi: 10.1002/er.3051

Liu, H., Zhan, S., Guo, P., Fan, S., and Zhang, S. (2018). Understanding the characteristic of methane hydrate equilibrium in materials and its potential application. *Chem. Eng. J.* 349, 775–781. doi: 10.1016/j.cej.2018.05.150

Mingjun, Y., Yongchen, S., Liu, Y., Yongjun, C., and Qingping, L. (2010). Influence of pore size, salinity and gas composition upon the hydrate formation conditions. *Therm. Chem. Eng. Data* 18, 292–296. doi: 10.1016/S1004-9541(08)60355-9

Mohan, M., Sharma, V. K., Kumar, E. A., and Gayathri, V. (2019). Hydrogen storage in carbon materials—A review. *Energy Storage* 1:35. doi: 10.1002/est2.35

Najibi, H., Chapoy, A., and Tohidi, B. (2008). Methane_natural gas storage and delivered capacity for activated carbons in dry and wet conditions. *Fuel* 87, 7–13. doi: 10.1016/j.fuel.2007.03.044

Nashed, O., Partoon, B., Lal, B., Sabil, K. M., and Shariff, A. M. (2018). Review the impact of nanoparticles on the thermodynamics and kinetics of gas hydrate formation. *J. Nat. Gas Sci. Eng.* 55, 452–465. doi: 10.1016/j.jngse.2018.05.022

Nikitin, A., Li, X., Zhang, Z., Ogasawara, H., Dai, H., and Nilsson, A. (2008). Hydrogen storage in carbon nanotubes through the formation of stable C-H bonds. *Nano Lett.* 8, 162–167. doi: 10.1021/nl072325k

Palodkar, A. V., and Jana, A. K. (2020). Clathrate hydrate dynamics with synthetic and bio-surfactant in porous media: model formulation and validation. *Chem. Eng. Sci.* 213:115386. doi: 10.1016/j.ces.2019.115386

Park, S. S., An, E. J., Lee, S. B., Chun, W. G., and Kim, N. J. (2012). Characteristics of methane hydrate formation in carbon nanofluids. *J. Ind. Eng. Chem.* 18, 443–448. doi: 10.1016/j.jiec.2011.11.045

Park, S. S., Lee, S. B., and Kim, N. J. (2010). Effect of multi-walled carbon nanotubes on methane hydrate formation. *J. Ind. Eng. Chem.* 16, 551–555. doi: 10.1016/j.jiec.2010.03.023

Pasieka, J., Coulombe, S., and Servio, P. (2013). Investigating the effects of hydrophobic and hydrophilic multi-wall carbon nanotubes on methane hydrate growth kinetics. *Chem. Eng. Sci.* 104, 998–1002. doi: 10.1016/j.ces.2013.10.037

Pasieka, J., Coulombe, S., and Servio, P. (2014). The effect of hydrophilic and hydrophobic multi-wall carbon nanotubes on methane dissolution rates in water at three phase equilibrium (V-L-w-H) conditions. *Ind. Eng. Chem. Res.* 53, 14519–14525. doi: 10.1021/ie502457c

Pasieka, J., Jorge, L., Coulombe, S., and Servio, P. (2015). Effects of as-produced and amine-functionalized multi-wall carbon nanotubes on carbon dioxide hydrate formation. *Energ. Fuel.* 29, 5259–5266. doi: 10.1021/acs.energyfuels.5b01036

Perrin, A., Celzard, A., Marêch,é, J. F., and Furdin, G. (2003). Methane storage within dry and wet active carbons a comparative study. *Energ. Fuel.* 17, 1283–1291. doi: 10.1021/ef030067i

Siangsai, A., Rangsunvigit, P., Kitiyanan, B., Kulprathipanja, S., and Linga, P. (2015). Investigation on the roles of activated carbonparticle sizes on methane hydrate formation and dissociation. *Chem. Eng. Sci.* 126, 383–389. doi: 10.1016/j.ces.2014.12.047

Sloan, E. D. (1998). *Clathrate Hydrate of Natural Gases*. New York, NY: Marcel Dekker.

Song, Y., Wang, F., Liu, G. Q., Luo, S. J., and Guo, R.B. (2017). Promotion efffect of nanotubes-doped SDS on the methane hydrate formation. *Energ.Fuel.* 31, 1850–1857. doi: 10.1021/acs.energyfuels.6b02418

Song, Y. M., Wang, F., Guo, G., Luo, S. J., and Guo, R. B. (2017). Amphiphilic-polymer-coated carbon nanotubes as promoters for methane hydrate formation. *ACS Sustain Chem Eng.* 5, 9271–9278. doi: 10.1021/acssuschemeng.7b02239

Song, Y. M., Wang, F., Luo, S. J., Guo, R. B., and Xu, D. (2019). Methane hydrate formation improved by water-soluble carbon nanotubes via π-π conjugated molecules functionalization. *Fuel* 243, 185–191. doi: 10.1016/j.fuel.2019.01.081

Song, Y. M., Wang, F., Guo, G., Luo, S.-J., and Guo, R.-B. (2018). Energy-efficient storage of methane in the formed hydrates with metal nanoparticles-grafted carbon nanotubes as promoter. *Appl. Energ.* 224, 175–183. doi: 10.1016/j.apenergy.2018.04.068

Takahata, M., Kashiwaya, Y., and Ishi, K. (2010). Kinetics of methane hydrate formation catalyzed by iron oxide and carbon under intense stirring conditions. *Mater Trans* 51, 727–734. doi: 10.2320/matertrans.M2009369

Thomas, S. (2003). Review of ways to transport natural gas energy from countries which do not need the gas for domestic use. *Energy* 28, 1461–1477. doi: 10.1016/s0360-5442(03)00124-5

Veluswamy, H. P., Kumar, A., Seo, Y., Lee, J. D., and Linga, P. (2018). A review of solidified natural gas (SNG) technology for gas storage via clathrate hydrates. *Appl. Energ.* 216, 262–285. doi: 10.1016/j.apenergy.2018.02.059

Wang, F., Meng, H. L., Guo, G., Luo, S. J., and Guo, R. B. (2017). Methane hydrate formation promoted by -SO3–coated graphene oxide nanosheets. ACS sustain. *Chem. Eng.* 5, 6597–6604. doi: 10.1021/acssuschemeng.7b00846

Wang, R., Liu, T., Ning, F., Ou, W., Zhang, L., Wang, Z., et al. (2019). Effect of hydrophilic silica nanoparticles on hydrate formation: insight from the experimental study. *J. Energ Chem.* 30, 90–100. doi: 10.1016/j.jechem.2018.02.021

Yan, L., Chen, G., Pang, W., and Liu, J. (2005). Experimental and modeling study on hydrate formation in wet activated carbon. *J. Phys. Chem. B* 109, 6025–6030. doi: 10.1021/jp045679y

Yang, M., Song, Y., Ruan, X., Liu, Y., Zhao, J., and Li, Q. (2012). Thermodynamic modeling of pure components including the effects of capillarity. *Energies* 5, 925–937. doi: 10.3390/en5040925

Yu, Y. S., Xu, C. G., and Li, X. S. (2018). Evaluation of CO_2 hydrate formation from mixture of graphite nanoparticle and sodium dodecyl benzene sulfonate. *J. Ind. Eng. Chem*. 59, 64–69. doi: 10.1016/j.jiec.2017.10.007

Yu, Y. S., Zhou, S. D., Li, X. S., and Wang, S. L. (2016). Effect of graphite nanoparticles on CO_2 hydrate phase equilibrium. *Fluid Phase Equilibr*. 414, 23–28. doi: 10.1016/j.fluid.2015.12.054

Zhang, Z., Liu, Z., Pan, Z., Baena-Morenoe, F. M., and Soltanian, M. R. (2020). Effect of porous media and its distribution on methane hydrate formation in the presence of surfactant. *Appl. Energ*. 261:114373. doi: 10.1016/j.apenergy.2019.114373

Zhong, Y., and Rogers, R. E. (2000). Surfactant effects on gas hydrate formation. *Chem. Eng. Sci*. 55, 4175–4187. doi: 10.1016/S0009-2509(00)00072-5

Zhou, L., and Sun, Y. (2001). Enhancement of the methane storage on activated carbon by preadsorbed water. *AIChE J*. 48, 2412–2416. doi: 10.1002/aic.690481030

Conflict of Interest: The authors declare that the research was conducted in the absence of any commercial or financial relationships that could be construed as a potential conflict of interest.

frontiers in Chemistry

MINI REVIEW
published: 19 June 2020
doi: 10.3389/fchem.2020.00481

Graphene-Based Kinetic Promotion of Gas Hydrate Formation

*Meng-Ting Sun, Guo-Dong Zhang and Fei Wang**

Shandong Engineering Laboratory for Preparation and Application of High-Performance Carbon-Materials, College of Electromechanical Engineering, Qingdao University of Science and Technology, Qingdao, China

Gas hydrate technology holds great potential in energy and environmental fields, and achieving efficient gas hydrate formation is critical for its industrial application. Graphene is a novel carbon-based nanostructured material with excellent thermal conductivity and a large specific surface area. Therefore, the use of graphene-based materials for the promotion of gas hydrate formation might be feasible and has aroused a lot of interests. Accordingly, to evaluate the current research on graphene-based promotion of gas hydrate formation, this work presents a review of existing studies involving graphene-based promoters of gas hydrate formation. Here, the studies applying various types of graphene-based promoters for gas hydrate formation are listed and detailed, the peculiar properties of graphene-based promoters are discussed, and the promotion mechanisms are analyzed. Through this review, comprehensive insight into graphene-based promotion of gas hydrate formation can be obtained, which can guide the design and applications of novel graphene-based promoters and might contribute to achieving efficient gas hydrate formation.

Keywords: gas hydrate formation, graphene, promoter, kinetics, interfacial transfer

OPEN ACCESS

Edited by:
Enza Fazio,
University of Messina, Italy

Reviewed by:
Giuseppe Compagnini,
University of Catania, Italy
Chiara Castiglioni,
Politecnico di Milano, Italy

****Correspondence:***
Fei Wang
elliot_wang@qust.edu.cn

Specialty section:
This article was submitted to Physical Chemistry and Chemical Physics, a section of the journal Frontiers in Chemistry

Received: *30 December 2019*
Accepted: *08 May 2020*
Published: *19 June 2020*

Citation:
Sun M-T, Zhang G-D and Wang F (2020) Graphene-Based Kinetic Promotion of Gas Hydrate Formation. Front. Chem. 8:481. doi: 10.3389/fchem.2020.00481

INTRODUCTION

Gas hydrates have captured an increasing amount of attention during the past decades because of their great potential for energy storage and environmental conservation (Li et al., 2019). Gas hydrates are ice-like crystalline compounds formed by water molecules (hosts) and gas molecules (guests) under favorable conditions. Water molecules form cage-like vacancies via hydrogen bonds and trap gas molecules in vacancies via Van der Waals forces (Sun et al., 2003). Commonly, based on the crystal structures of hydrates, gas hydrates are considered to have three representative types: structure I, structure II, and structure H (**Figure 1**; Takeya et al., 2009). Gas hydrates can achieve high storage capacity and are stored under mild conditions and accordingly are considered to be highly promising media for gas separation, gas storage and transportation, and carbon capture and sequestration (Zhong and Rogers, 2000; Li et al., 2019). The gas hydrate formation process (HFP) involves two stages: the nucleation period and the growth period. During the nucleation period, the hydrate crystals are formed by gas and water molecules. However, these hydrate crystals are not stable until they grow to critical sizes, which leads to a stochastic and long nucleation period. After that, rapid hydrate growth is achieved, and a hydrate film is initially formed at the gas–liquid interface, which hinders the diffusion of gas into liquid and consequently results in a slow hydrate formation rate and low water to hydrate conversion. The stochastic induction time and the low formation rate are the main issues impeding the industrial application of gas hydrates (He and Wang, 2018). Therefore, achieving efficient gas hydrate formation is essential for the industrialization of gas hydrate technology.

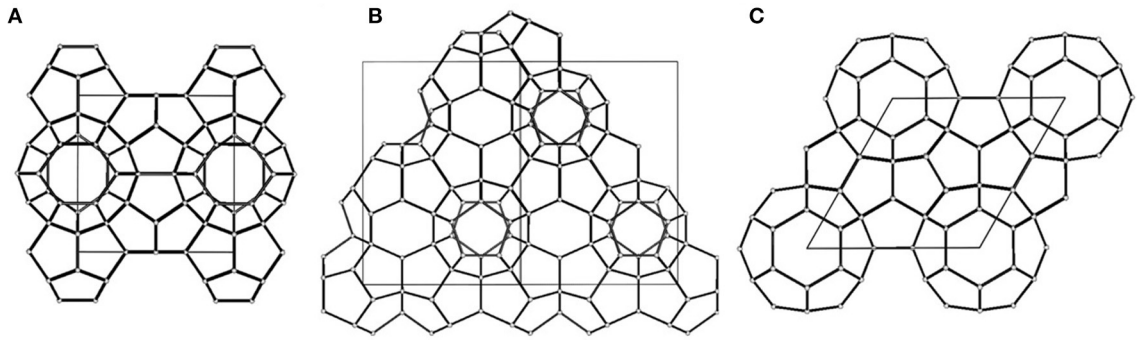

FIGURE 1 | Crystal structure types of gas hydrates: **(A)** Structure I, **(B)** Structure II, **(C)** Structure H; the solid line in each figure represents the unit cell of gas hydrates; reproduced from Takeya et al. (2009) with permission from the American Chemical Society.

Because HFP is an interfacial phenomenon, increasing heat or mass transfer in the gas–liquid interface can effectively promote the hydrate formation rate. Mechanical methods, which include stirring, water spraying, and gas bubbling, can achieve rapid hydrate growth via improving mass transfer between gas, and liquid. However, mechanical methods consume energy, which leads to increased cost and, at the same time, generates frictional heat in the system, which works against the exothermic hydrate formation (Fukumoto et al., 2001; Luo et al., 2007; Zhong et al., 2015). During the past two decades, increasing research interest has been paid to promoters, which act as non-mechanical methods to improve HFP. Promoters are divided into two categories: thermodynamic promoters and kinetic promoters (He et al., 2019). Thermodynamic promoters, including tetra-n-butyl ammonium halide (TBAH) and tetrahydrofuran (THF), enhance hydrate formation via reducing the phase equilibrium conditions and moderating the reaction conditions (Joshi et al., 2012; da Silva Lirio et al., 2013). Kinetic promoters improve heat or mass transfer during HFP and consequently speed up the hydrate formation rate (Nashed et al., 2018). Various surfactants have been applied to facilitate the dissolution of gas in water by reducing the mass transfer resistance and have resulted in an improved hydrate formation rate and a reduced induction time. Among these, sodium dodecyl sulfate (SDS) performed best in promoting HFP (He et al., 2019). However, the surfactants generate a large amount of foam in the system and cover the gas–water interface, which reduces the dissolution of gas in water as well as causing losses of surfactants (Veluswamy et al., 2016).

Recently, carbon nanostructures have been demonstrated to be efficient promoters of gas HFP without causing the foaming problem (Park et al., 2010). On the one hand, HFP is exothermic, and the heat generated during the process will detroy the hydrate crystals and negatively impact hydrate growth; therefore, carbon nanostructures with high thermal conductivity can eliminate the heat from the system, which maintains the system at a low temperature and makes the hydrate growth more stable. On the other hand, the carbon nanostructures exhibit a large specific surface area due to their nanometric shape and size, which provides more active sites for nucleation and consequently increases mass transfer. Furthermore, the inhomogeneity of the system will rise in the presence of carbon nanostructures, and heterogeneous nucleation will occur, which forms hydrate crystals more easily than homogenous nucleation. Accordingly, the HFP can be improved by carbon nanostructures (Ghozatloo et al., 2015; Rezaei et al., 2016).

As a novel carbon nanostructure, graphene presents excellent mechanical strength and thermal conductivity and large specific surface area, making it a promising candidate for the promotion of gas hydrate formation (Wang et al., 2017). Here, we implement a review focusing on graphene-based promoters of gas hydrate formation. We initially introduce the exceptional properties of graphene-based materials; we then expound the cases where different graphene-based promoters have been used for gas hydrate formation and discuss their promotion mechanisms in detail.

PROPERTIES OF GRAPHENE AND RELATED MATERIALS

Graphene is a two-dimensional, single-layer nanosheet consisting of sp^2 hybridized and honeycomb-arranged carbon atoms (**Figure 2A**; Huang et al., 2011). The peculiar layer structure and chemical structure endow graphene with remarkable properties, including large specific surface area, high transparency, excellent mechanical strength, and superior electrical and thermal conductivities, which enable graphene to permit a wide range of applications (Park and Ruoff, 2009).

Pristine graphene is highly hydrophobic and is impossible to directly disperse in water without assistance or dispersing agents, which constrains large-scale solution-based production and application processes (Li et al., 2008). Graphene derivatives, such as graphene oxide (GO) and chemically modified graphene (CMG), have been prepared. Compared to pristine graphene, graphene derivatives keep more oxygen-containing groups or other functional groups, which cause graphene derivatives to exhibit more appreciable dispersity and chemical reactivity (Huang et al., 2011). Graphene and its derivatives have been further incorporated into different functional materials to form graphene-based composites, which could be applied in the fabrication of field-effect transistors, sensors, clean energy devices, transparent conductive

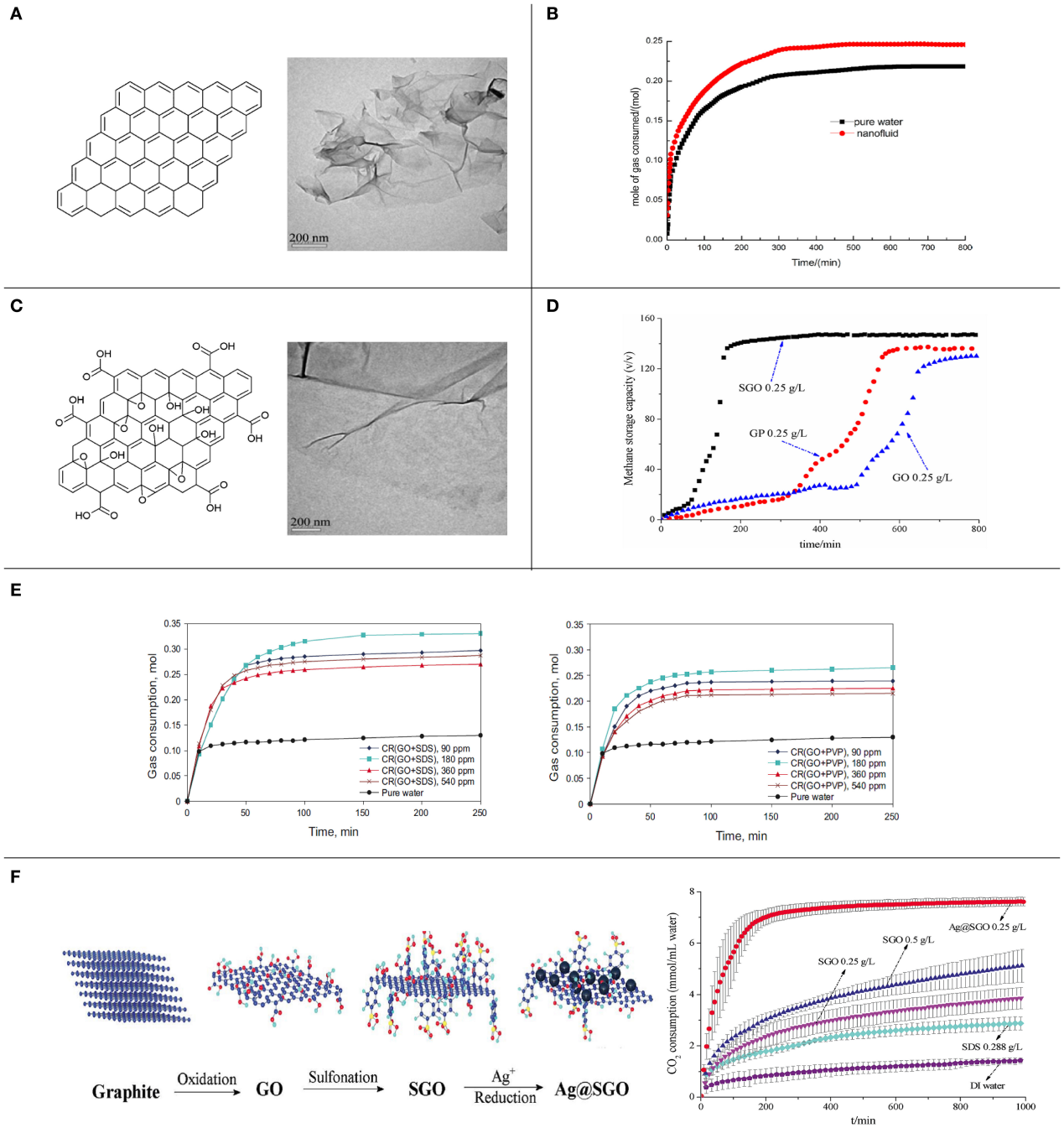

FIGURE 2 | (A) Structural diagram and TEM image of graphene; reproduced from Wang et al. (2017) with permission from the American Chemical Society. **(B)** Gas consumption during CO_2 hydrate formation with pure water and graphene nanofluid; reproduced from Zhou et al. (2014) with permission from the American Chemical Society. **(C)** Structural diagram and TEM image of GO; reproduced from Wang et al. (2017) with permission from the American Chemical Society. **(D)** Storage capacity during methane hydrate formation in the presence of graphene, GO, and SGO; reproduced from Wang et al. (2017) with permission from the American Chemical Society. **(E)** Gas consumption during methane hydrate formation at different concentrations of chemically RGO with SDS and PVP; reproduced from Abedi-Farizhendi et al. (2019b) with permission from the China University of Petroleum Beijing. **(F)** Structural diagram of graphite, GO, SGO, and Ag@SGO, and gas consumption during CO_2 hydrate formation with different promoters; reproduced from He and Wang (2018), which was previously conducted by us and originally published by the Royal Society of Chemistry.

films, photocatalysis, etc. (Kumar et al., 2019). Graphene, graphene derivatives, and graphene-based composites are collectively known as graphene-based materials, all of which have admirable thermal and electrical properties as well as presenting a nanostructure and a large specific surface area (**Figure 2**).

GRAPHENE-BASED PROMOTORS OF GAS HYDRATE FORMATION

Due to their excellent properties, graphene-based materials might be exceptional promoters of gas hydrate formation: they can efficiently improve heat transfer by removing the heat generated during HFP and can meanwhile increase mass transfer due to their nanostructure and also accelerate nucleation by increasing inhomogeneity of the system, which consequently promote gas hydrate formation. The studies employing graphene-based materials as promoters of gas hydrate formation are shown in **Table S1**.

Graphene

The hydrophobic graphene has been dispersed in water to prepare graphene nanofluid, and this has been used as a promoter of gas hydrate formation. Ghozatloo et al. (2015) studied the effects of graphene in natural gas hydrate formation and utilized 1 wt% of graphene nanofluid at initial conditions of 6.89 MPa and 277.15 K. The results showed that the graphene nanofluid could reduce the induction time by 61.07% and increase the storage capacity by 12.9% compared with pure water (**Figure 2B**). These enhancements might be attributable to the increase in initial dissolved gas in nanofluid, heterogeneous nucleation, and the heat transfer coefficient. Wang et al. (2017) used graphene nanofluid to promote methane hydrate formation at initial conditions of 6 MPa and 277.15 K with 300 rpm stirring and found that graphene (0.25–0.75 g L^{-1}) reduced the hydrate formation period by 45–80% and improved the hydrate formation rate and the storage capacity by 190–660% and 45–70%, respectively, compared with pure water. The results implied that the graphene nanosheets not only increased heterogeneous nucleation in the system and provided abundant active sites for hydrate nucleation but also produced a high transfer efficiency that could remove the heat generated by hydrate formation from the system, consequently improving the efficiency of methane hydrate formation. Due to similar promotion mechanisms, graphite nanoparticles also have positive effects on gas hydrate formation. Zhou et al. (2014) applied graphite nanoparticles to promote CO_2 hydrate formation at initial conditions of 3.5 MPa and 277.15 K with 300 rpm stirring and suggested that the induction time was decreased by 80.8% and the maximum CO_2 consumption was increased by 12.8% in comparison to pure water. They argued that the high heat transfer coefficient and the large specific surface area of graphite nanoparticles played critical roles in promoting CO_2 hydrate formation.

Graphene Oxide

GO sheet is exfoliated from graphite oxide and has abundant oxygen-containing groups on its surface. GO also retains a single-layer structure, good thermal properties, and a huge specific surface area (**Figure 2C**). Compared to graphene, the thermal conductivity of GO is weakly decreased because of the existence of oxygen-containing groups that destroy the conjugated structure of nanosheets (Wang et al., 2017). However, GO is amphipathic and can act as a surfactant and presents superior dispersion in water; therefore, GO might be suitable for promoting gas hydrate formation (Yan et al., 2018).

GO has been immediately added into the system during HFP and functioned well in promoting gas hydrate formation. Rezaei et al. (2016) conducted ethylene hydrate formation with GO and SDS as promoters, revealing that GO was more effective in decreasing the induction time while SDS performed better in increasing the storage capacity. The minimum induction time, reduced by 96% compared to pure water, was obtained by 150 ppm of GO. The storage capacity failed to be promoted at a low concentration of GO (50 ppm), whereas it was markedly promoted at high concentrations of GO (150 and 150 ppm). Rezaei et al. argued that GO could provide an excellent structure for heterogeneous nucleation and a network pattern for the assembly of water and ethylene molecules. Additionally, its high specific surface area could improve mass transfer, and, meanwhile, the carboxyl and hydroxyl groups on GO could incorporate hydrogen bonds that further stabilize the hydrate crystals. Abedi-Farizhendi et al. (2019a) carried out propane hydrate formation in the presence of reduced graphene oxide (RGO) and GO, and the results indicated that they both improved the propane hydrate nucleation and formation rate while having no significant effects on storage capacity and water to hydrate conversion. The improvements could be attributed to the numerous nucleation sites, high specific surface area, and increased mass transfer produced by carbon nanostructures. Yan et al. (2018) adopted GO as a promoter of CO_2 hydrate formation at 279 K and different initial pressures ranging from 3 to 5 MPa. They found that GO could shorten the induction time by 53–74.3% and increase the gas consumption by 5.1–15.9%. These effects were ascribed to the high heat and mass transfer efficiencies, high gas dissolution, and improved nucleation and formation rate.

However, a few studies found that GO also had inhibiting effects on gas hydrate formation. Kim et al. (2014) mentioned that the confinement and strong interaction of water caused by nano-sized pores and hydrophilic groups of GO could reduce water activity and therefore that the phase behavior of methane hydrates would be significantly inhibited. In another study, Wang et al. (2017) investigated the effects of GO on methane hydrate formation and revealed that GO exhibited poorer promotion effects on hydrate formation compared with graphene, which might possibly be attributable to the lowered thermal conductivity of GO and the reduced water activity caused by GO (**Figure 2D**).

Collectively, GO has favorable thermal conductivity, a nanostructure, and a large specific surface area, which could increase heat and mass transfers during HFP. Meanwhile, the stronger hydrophilicity of GO could accelerate its dispersion in water, which is convenient for the use of GO in an aqueous system during HFP. However, the hydrophilicity of GO also has inhibitory effects on HPF, as it reduces the water activity in the system and possibly inhibits gas hydrate formation. Fortunately, with abundant functional groups, GO has admirable dispersity and chemical reactivity and accordingly can be readily modified by chemical modification methods of its carbon backbone to produce CMG, which offers infinite possibilities for

improvement of the properties of GO to make it more applicable for the promotion of gas hydrate formation.

Surfactant-Stabilized Graphene

In addition to the direct promotion of gas hydrate formation, graphene can also be mixed with surfactants to generate surfactant-stabilized nanofluids. Graphene usually exhibits poor dispersity and stability during gas hydrate formation, causing weak performance and cyclability during promotion. Therefore, a mixture of graphene and surfactants has been employed, where the surfactants function as both stabilizer and co-promoter. Hosseini et al. (2015) used SDS to stabilize graphene nanofluid (1 wt%) to prepare an SDS/graphene promoter for natural gas hydrate formation and indicated that the SDS/graphene promoter reduced the induction time by 19.2% and increased the storage capacity by 7.6% compared to the SDS/water system. The reduction in induction time was attributed to the presence of heterogeneous nucleation and a high heat transfer coefficient, and the enhancement in storage capacity was considered to be due to the increased gas dissolution and heterogeneous active sites. Moreover, the addition of SDS could improve the stability of nanosheets in aqueous suspensions. Abedi-Farizhendi et al. (2019b) synthesized RGO with SDS and polyvinylpyrrolidone (PVP), respectively, which were applied to promote methane hydrate formation at initial conditions of 4.5 MPa and 273.15 K. The results showed that the synthesized promoters both significantly decreased the induction time and considerably increased the water to hydrate conversion while not changing the storage capacity (**Figure 2E**). On the one hand, the RGO might produce heterogeneous nucleation, which has a lower effective surface energy, causing lower free energy and a lower nucleation barrier than homogeneous nucleation, and is consequently more kinetically favorable than homogeneous nucleation. Additionally, the carbon nanostructures provide numerous nucleation sites to facilitate nucleation. On the other hand, the movement of carbon nanostructures decreased resistance in the gas–liquid interface. Therefore, the mass transfer was increased, leading to a reduced induction time. Yu et al. (2018) mixed graphite nanoparticles (GN, 0.4 wt%) with different concentrations of sodium dodecyl benzene sulfonate (SDBS) to prepare promoters and subsequently investigated the synergistic effects of GN and SDBS on the kinetics of CO_2 hydrate formation. The experimental results showed that the gas consumption, hydrate storage, hydrate formation rate, and water to hydrate conversion were increased by 86.4, 35.8, 85.1, and 20%, respectively, in the presence of GN+SDBS (0.04%) compared in a pure water system. Adding SDBS into GN nanofluid could inhibit GN aggregation and greatly reduce the surface tension of the solution, making gas molecules dissolve in water more easily, which favored CO_2 hydrate formation.

Graphene-Carried Promoters

Due to its firm and stable carbon backbone, graphene can also serve as a nanocarrier to fabricate novel promoters of gas hydrate formation. Wang et al. (2017) grafted $-SO_3^-$ onto graphene nanosheets through sulfonation to form an SGO promoter, and SGO performed more efficiently than graphene nanofluid and GO in promoting methane hydrate formation. Methane hydrate formation finished within 200–300 min with 0.25–0.75 g L^{-1} of SGO, and the storage capacity reached 140–150 v/v (**Figure 2D**). On the one hand, the majority of oxygen-containing groups were reduced during preparation, which removed the inhibition of water activity. On the other hand, $-SO_3^-$-coated nanosheets could provide a large interface for methane molecule adsorption and water molecule association and therefore led to a rapid hydrate formation rate. Furthermore, a novel promoter named Ag@SGO has been synthesized by He and Wang through grafting Ag nanoparticles onto SGO nanosheets, and this was subsequently used as a promoter for CO_2 hydrate formation. Under 0.25 g L^{-1} of Ag@SGO, most of the CO_2 hydrate formation finished within 200–250 min, and CO_2 consumption reached 7.62 ± 0.16 mmol mL^{-1} water at 1000 min, which was almost 2.6 times that with SDS (**Figure 2F**; He and Wang, 2018). Ag nanoparticles could provide additional active sites for nucleation as well-removing heat from the system and accordingly further facilitated the CO_2 hydrate formation.

Summarily, using graphene as a nanocarrier for various functional groups and nanoparticles is an effective, flexible, and feasible approach to preparing novel promoters for gas hydrate formation and is well-worth further study.

CONCLUSION AND PROSPECTS

In this review, the existing studies on graphene-based promoters of gas hydrate formation have been summarized, the beneficial properties and advantages of graphene-based materials have been emphasized, and the promotion mechanisms of graphene, GO, surfactant-stabilized graphene, and graphene-carried promoters have been discussed and analyzed. Graphene-based materials with admirable properties are capable of promoting gas hydrate formation: the heat generated during HFP can be removed by graphene-based materials because of their high thermal conductivity, which increases heat transfer in the system and avoids the destruction of hydrate crystals by high temperature; secondly, graphene-based materials with a large specific surface area can increase mass transfer during HFP via providing abundant active sites for nucleation; additionally, the appearance of graphene-based materials can increase inhomogeneity in the system, and the heterogeneous nucleation forms hydrate crystals more readily than homogenous nucleation, effectively promoting gas hydrate formation.

The existing studies on graphene-based promotion of gas hydrate formation were implemented in lab-scale experiments, so the promotion effects, stability, and cyclability of graphene-based promoters in gas hydrate formation need to be investigated in pilot tests, which could be conducted in future work. Additionally, further research can focus on grafting graphene/GO with functional groups to produce exceptional CMG or introducing functional nanoparticles (e.g., Ag and Fe_3O_4 nanoparticles) onto surfaces of graphene/GO, aiming to obtain novel graphene-based promoters with desirable properties to significantly promote gas hydrate formation. Moreover, because of its nanostructure and

remarkable electrical conductivity, graphene might serve as a nano-sized electric rotor under an electric field that could effectively stir within nano-sized confinement spaces, which might possibly be applied for HFP promotion via improving mass transfer.

AUTHOR CONTRIBUTIONS

M-TS wrote and revised the manuscript. FW and G-DZ supervised and revised the manuscript. All authors contributed to the article and approved the submitted version.

FUNDING

This work was supported by the National Natural Science Foundation of China (21978142), the Youth Innovation Talent Development Project for Universities of Shandong Province, and the Taishan Scholar Project of Shandong Province (ts20190937).

SUPPLEMENTARY MATERIAL

The Supplementary Material for this article can be found online at: https://www.frontiersin.org/articles/10.3389/fchem.2020.00481/full#supplementary-material

REFERENCES

Abedi-Farizhendi, S., Iranshahi, M., Mohammadi, A., Manteghian, M., and Mohammadi, A. H. (2019b). Kinetic study of methane hydrate formation in the presence of carbon nanostructures. *Petrol. Sci.* 16, 657–668. doi: 10.1007/s12182-019-0327-5

Abedi-Farizhendi, S., Rahmati-Abkenar, M., Manteghian, M., Salehzadeh Yekshaveh, J., and Zahmatkeshan, V. (2019a). Kinetic study of propane hydrate in the presence of carbon nanostructures and SDS. *J. Petrol. Sci. Eng.* 172, 636–642. doi: 10.1016/j.petrol.2018.04.075

da Silva Lirio, C. F., Pellegrini Pessoa, F. L., and Cohen Uller, A. M. (2013). Storage capacity of carbon dioxide hydrates in the presence of sodium dodecyl sulfate (SDS) and tetrahydrofuran (THF). *Chem. Eng. Sci.* 96, 118–123. doi: 10.1016/j.ces.2012.10.022

Fukumoto, K., Tobe, J., Ohmura, R., and Mori, Y. H. (2001). Hydrate formation using water spraying in a hydrophobic gas: a preliminary study. *AIChE J.* 47, 1899–1904. doi: 10.1002/aic.690470821

Ghozatloo, A., Hosseini, M., and Shariaty-Niassar, M. (2015). Improvement and enhancement of natural gas hydrate formation process by Hummers' graphene. *J. Nat. Gas Sci. Eng.* 27, 1229–1233. doi: 10.1016/j.jngse.2015.09.069

He, Y., Sun, M. T., Chen, C., Zhang, G. D., Chao, K., Lin, Y., et al. (2019). Surfactant-based promotion to gas hydrate formation for energy storage. *J. Mater. Chem. A.* 7, 21634–21661. doi: 10.1039/C9TA07071K

He, Y., and Wang, F. (2018). Hydrate-based CO_2 capture: kinetic improvement via graphene-carried $-SO^{3-}$ and Ag nanoparticles. *J. Mater. Chem. A* 6, 22619–22625. doi: 10.1039/C8TA08785G

Hosseini, M., Ghozatloo, A., and Shariaty-Niassar, M. (2015). Effect of CVD graphene on hydrate formation of natural gas. *J. Nanostruct. Chem.* 5, 219–226. doi: 10.1007/s40097-015-0153-2

Huang, X., Yin, Z., Wu, S., Qi, X., He, Q., Zhang, Q., et al. (2011). Graphene-based materials: synthesis, characterization, properties, and applications. *Small* 7, 1876–1902. doi: 10.1002/smll.201002009

Joshi, A., Mekala, P., and Sangwai, J. S. (2012). Modeling phase equilibria of semiclathrate hydrates of CH_4, CO_2 and N_2 in aqueous solution of tetra-n-butyl ammonium bromide. *J. Nat. Gas Chem.* 21, 459–465. doi: 10.1016/S1003-9953(11)60391-5

Kim, D., Kim, D. W., Lim, H. K., Jeon, J., Kim, H., Jung, H. T., et al. (2014). Inhibited phase behavior of gas hydrates in graphene oxide: influences of surface and geometric constraints. *Phys. Chem. Chem. Phys.* 16, 22717–22722. doi: 10.1039/C4CP03263B

Kumar, A., Sharma, K., and Dixit, A. R. (2019). Carbon nanotube- and graphene-reinforced multiphase polymeric composites: review on their properties and applications. *J. Mater. Sci.* 55, 2682–2724. doi: 10.1007/s10853-019-04196-y

Li, D., Muller, M. B., Gilje, S., Kaner, R. B., and Wallace, G. G. (2008). Processable aqueous dispersions of graphene nanosheets. *Nat. Nanotech.* 3, 101–105. doi: 10.1038/nnano.2007.451

Li, S., Lv, R., Wu, Y., Huang, F., Zhang, X., and Yue, T. (2019). Size-, aggregation-, and oxidization-dependent perturbation of methane hydrate by graphene nanosheets revealed by molecular dynamics simulations. *J. Phys. Chem. C.* 123, 13154–13166. doi: 10.1021/acs.jpcc.9b02659

Luo, Y. T., Zhu, J. H., Fan, S. S., and Chen, G. J. (2007). Study on the kinetics of hydrate formation in a bubble column. *Chem. Eng. Sci.* 62, 1000–1009. doi: 10.1016/j.ces.2006.11.004

Nashed, O., Partoon, B., Lal, B., Sabil, K. M., and Shariff, A. M. (2018). Review the impact of nanoparticles on the thermodynamics and kinetics of gas hydrate formation. *J. Nat. Gas Sci. Eng.* 55, 452–465. doi: 10.1016/j.jngse.2018.05.022

Park, S., and Ruoff, R. S. (2009). Chemical methods for the production of graphenes. *Nat. Nanotechnol.* 4, 217–224. doi: 10.1038/nnano.2009.58

Park, S. S., Lee, S. B., and Kim, N. J. (2010). Effect of multi-walled carbon nanotubes on methane hydrate formation. *J. Ind. Eng. Chem.* 16, 551–555. doi: 10.1016/j.jiec.2010.03.023

Rezaei, E., Manteghian, M., and Tamaddondar, M. (2016). Kinetic study of ethylene hydrate formation in presence of graphene oxide and sodium dodecyl sulfate. *J. Petrol. Sci. Eng.* 147, 857–863. doi: 10.1016/j.petrol.2016.10.008

Sun, Z., Wang, R., Ma, R., Guo, K., and Fan, S. (2003). Natural gas storage in hydrates with the presence of promoters. *Energ. Convers. Manage.* 44, 2733–2742. doi: 10.1016/S0196-8904(03)00048-7

Takeya, S., Udachin, K. A., Moudrakovski, I. L., Susilo, R., and Ripmeester, J. A. (2009). Direct space methods for powder x-ray diffraction for guest-host materials: applications to cage occupancies and guest distributions in clathrate hydrates. *J. Am. Chem. Soc.* 132, 524–531. doi: 10.1021/ja905426e

Veluswamy, H. P., Hong, Q. W., and Linga, P. (2016). Morphology study of methane hydrate formation and dissociation in the presence of amino acid. *Cryst. Growth Des.* 16, 5932–5945. doi: 10.1021/acs.cgd.6b00997

Wang, F., Meng, H. L., Guo, G., Luo, S. J., and Guo, R. B. (2017). Methane hydrate formation promoted by $-SO^{3--}$ -coated graphene oxide nanosheets. *ACS Sustain. Chem. Eng.* 5, 6597–6604. doi: 10.1021/acssuschemeng.7b00846

Yan, S., Dai, W., Wang, S., Rao, Y., and Zhou, S. (2018). Graphene oxide: an effective promoter for CO_2 hydrate formation. *Energies* 11:1756. doi: 10.3390/en11071756

Yu, Y., Xu, C., and Li, X. (2018). Evaluation of CO_2 hydrate formation from mixture of graphite nanoparticle and sodium dodecyl benzene sulfonate. *J. Ind. Eng. Chem.* 59, 64–69. doi: 10.1016/j.jiec.2017.10.007

Zhong, D. L., Lu, Y. Y., Sun, D. J., Zhao, W. L., and Li, Z. (2015). Performance evaluation of methane separation from coal mine gas by gas hydrate formation in a stirred reactor and in a fixed bed of silica sand. *Fuel* 143, 586–594. doi: 10.1016/j.fuel.2014.11.083

Zhong, T., and Rogers, R. E. (2000). Surfactant effects on gas hydrate formation. *Chem. Eng. Sci.* 55, 4175–4187. doi: 10.1016/S0009-2509(00)00072-5

Zhou, S., Yu, Y., Zhao, M., Wang, S., and Zhang, G. (2014). Effect of graphite nanoparticles on promoting CO_2 hydrate formation. *Energ. Fuel.* 28, 4694–4698. doi: 10.1021/ef5000886

Conflict of Interest: The authors declare that the research was conducted in the absence of any commercial or financial relationships that could be construed as a potential conflict of interest.

frontiers in Chemistry

MINI REVIEW
published: 08 July 2020
doi: 10.3389/fchem.2020.00514

Biopromoters for Gas Hydrate Formation: A Mini Review of Current Status

Yong-Tao Zhang[1], *Fu-Lin Chen*[1], *Shi-Jie Yu*[2] *and Fei Wang*[1]*

[1] College of Electromechanical Engineering, Shandong Engineering Laboratory for Preparation and Application of High-Performance Carbon-Materials, Qingdao University of Science & Technology, Qingdao, China, [2] Military Representative Office of Army, Qingdao, China

Gas hydrates have promising application prospects in the fields of future energy sources, natural gas storage and transportation, CO_2 capture and sequestration, gas separation, and cold energy. However, the application of hydrate technologies is being restricted due to the slow formation rate of gas hydrates. Kinetic promoters have been receiving increased attention, given that they can improve the hydrate formation rate with very small doses and do not affect gas storage capacity. However, most kinetic promoters are non-renewable, petrochemical-derived, non-degradable materials, inevitably leading to resource waste and environmental pollution. Biopromoters, derived from biomass, are renewable, biodegradable, environmentally friendly, non-toxic (or low toxic), and economically feasible. This mini review summarizes the current status of already discovered biopromoters, including lignosulfonate, amino acid, biosurfactant, and biological porous structures, which have the potential to replace petrochemical-derived promoters in hydrate technologies. Finally, future research directions are given for the development of biopromoters.

Keywords: gas hydrate, biopromoter, kinetic promoter, biomass, mechanism

OPEN ACCESS

Edited by:
Zhuhua Zhang,
Nanjing University of Aeronautics and Astronautics, China

Reviewed by:
Jincheng Lei,
Rice University, United States
Senbo Xiao,
Norwegian University of Science and Technology, Norway

***Correspondence:**
Fei Wang
elliot_wang@qust.edu.cn

Specialty section:
This article was submitted to Physical Chemistry and Chemical Physics, a section of the journal Frontiers in Chemistry

Received: *20 February 2020*
Accepted: *18 May 2020*
Published: *08 July 2020*

Citation:
Zhang Y-T, Chen F-L, Yu S-J and Wang F (2020) Biopromoters for Gas Hydrate Formation: A Mini Review of Current Status. Front. Chem. 8:514. doi: 10.3389/fchem.2020.00514

INTRODUCTION

Gas hydrates are a form of non-stoichiometric crystalline, in which water molecules form the host lattice via hydrogen bonds and guest gases are trapped in the host lattice via intermolecular forces (He et al., 2019). Gas hydrates have been getting increased attention due to their promising number of applications, such as in future energy sources, natural gas storage and transportation, CO_2 capture and sequestration, gas separation, and cold energy (Sun and Kang, 2016; Veluswamy et al., 2018; He et al., 2019). However, the application of hydrate technology is restricted by the slow formation rate of hydrates.

Kinetic promoters can improve the hydrate formation rate with very small doses and do not affect gas storage capacity (He et al., 2019). Researchers have used various kinetic promoters for gas hydrate formation, such as synthetic surfactants, activated carbon, porous silica, metal nanoparticles, graphene, carbon nanotubes, glass beads, sand grains, and dry water (Siangsai et al., 2015; Chong et al., 2016; He et al., 2019). However, most of the promoters above are non-renewable, petrochemical-derived, non-degradable materials, which will inevitably lead to resource waste and environmental pollution. Synthetic surfactants show an obvious superiority compared with other promoters, particularly given the material cost, especially for sodium dodecyl sulfate (SDS) (He et al., 2019). However, synthetic surfactants, such as SDS, sodium tetradecyl sulfate (STS), and

sodium hexadecyl sulfate (SHS) can cause chronic toxicity in living organisms (Lewis, 1991), which restricts the application of hydrate technologies. For example, Ocean CO_2 sequestration in the form of CO_2 hydrates is being considered as an effective way to decrease the CO_2 content in the atmosphere (Sun and Kang, 2016). If CO_2 hydrates sequestrated in ocean sediments are formed using synthetic surfactants with chronic toxicity, the ocean ecological environment will suffer a dramatically adverse impact once those promoters are leaked into the ocean.

Biopromoters derived from biomass are renewable, biodegradable, environmentally friendly, nontoxic (or low toxic), and economically feasible. Biopromoters could be considered as promising promoters instead of traditional promoters for the application of hydrate technology. With the purpose of achieving a comprehensive evaluation on the discovered biopromoters and creating effective guidance for future research, this mini review summarizes the promoting effects and promoting mechanisms of discovered biopromoters which have the potential to replace petrochemical-derived promoters in gas hydrate technologies.

BIOPROMOTER

In the last 10 years, scholars have explored and discovered some biopromoters that can be used for gas hydrate formation, which can be divided into four categories: (1) lignosulfonates (LSs), (2) amino acids, (3) biosurfactants, and (4) biological porous structures. These four categories of biopromoters will be separately discussed in the following sections. The promoting effects of different biopromoters under corresponding experimental conditions are listed in **Table S1**.

LS

LSs, as byproducts of the sulfite pulping process in the pulp and paper industry, are obtained by cutting α-*O*-4 ether bonds in nature lignin and sulphonating α- and/or γ-positions of the side chains of C9 units (Myrvold, 2008). The basic structure of LSs is a phenylpropane derivative, including a C3-C6 hydrophobic skeleton. LSs also contain hydrophilic groups, such as the sulfonic acid group, carboxyl group, and phenolic hydroxyl group. Although the microstructure of LSs in aqueous solutions is still inconclusive, it has been confirmed that LS macromolecules can generate cross-links and form spherical, disc-like, or sheet-like microgels with sulfonic acid groups located on its outer surface (Myrvold, 2008). **Figure 1A** shows a spherical microgel model of LS macromolecules (Rezanowich and Goring, 1960). The cross-link of LS macromolecules may offer a hydrophobic space for dissolving more guest gases, and sulfonic acid groups can associate cross-linked LS molecules with water molecules through a hydrogen bond (Wang et al., 2017).

Formation kinetics of gas hydrates in LS aqueous solutions were first reported by Wang et al. (2012). **Figure 1B** shows the formation kinetics of a CH_4 hydrate in a calcium lignosulfonate (Ca-LS) aqueous solution with different concentrations (Wang et al., 2012). It can be seen that LS significantly improved the formation rate and gas storage capacity of the CH_4 hydrate. The storage capacity of the CH_4 hydrate reached 167 v/v (storage capacity was defined as the volume of guest gas stored in per unit volume of hydrate) within 1000 min in 0.5 wt% Ca-LS aqueous solution, t_{90} (the time to achieve 90% of the corresponding gas storage capacity) was only about 20 min, and the induction time reduced to <6 min. Among synthetic surfactants, the promoting effect of SDS is recognized as the best. However, a large amount of foam is generated during the dissociation process of the hydrate using SDS as a promoter, which not only influences the release of methane gas from the methane hydrate but also causes the loss of the SDS promoter in cyclic utilization (He et al., 2019). By contrast, the generated foam had a significant reduction during hydrate dissociation when the hydrate formed in a sodium lignosulfonate (Na-LS) aqueous solution, because the dissolution of Na-LS only generated a small amount foam (Mofrad et al., 2016). Besides, under certain concentrations, the CH_4 storage capacity using Na-LS as a promoter is better than that of SDS, although the formation rate of Na-LS is still lower than that of SDS (Mofrad et al., 2016). For a CO_2/CH_4 gas mixture system, gas storage capacity under a Na-LS promoter was about 1.7 times higher than that in pure water, but the hydrate formation still had a longer induction time, ranging from 46.7 min to 400 min (Yi et al., 2019).

Most scholars think the promoting mechanism of LSs comes from their being capillarity-driven and their mass transfer. As observed by Wang et al. (2012), a CH_4 hydrate grew upward along the inner wall of the reactor in an LS aqueous solution, which was a representative phenomenon from something that is capillarity-driven. As shown in **Figure 1C**, LS molecules can adsorb on the surface of forming hydrate particles under the action of hydrogen bonds between partial hydrophilic groups and hydrate molecules. Meanwhile, partial hydrophilic groups, such as sulfonic acid group and carboxyl group, are exposed to the outside surface of forming hydrate particles, which leads to mutual repulsion among forming hydrate particles under electrostatic action (Dicharry et al., 2016). And the hydrate particles become more wettable for water molecules due to hydrophilic groups. A water-wettable porous hydrate structure is formed, which drives the capillary action for sucking the water molecules to the reaction site of hydrate. CH_4 hydrate formation has stronger capillarity-driven action than a CO2 hydrate formation (Daniel-David et al., 2015). On the other hand, the LS molecules arrange on the gas-liquid interface and reduce interfacial tension, which enhances the diffusion of gas molecules from a gas phase to a liquid phase. As a result, the supersaturation of gas molecules in a liquid phase promotes hydrate nucleation. However, it is necessary to use higher concentrations of LS to reduce interfacial tensions, compared with single molecule surfactants (Gupta and Washburn, 2014).

Amino Acids

Amino acids are the basic constituent units of biologically macromolecular proteins and are an indispensable nutrient in the biological body. There are 20 species of amino acids obtained after proteolysis, around which researches have been focusing on both promoting hydrate formation and inhibiting hydrate formation in the last 10 years (Bavoh et al., 2019). The side

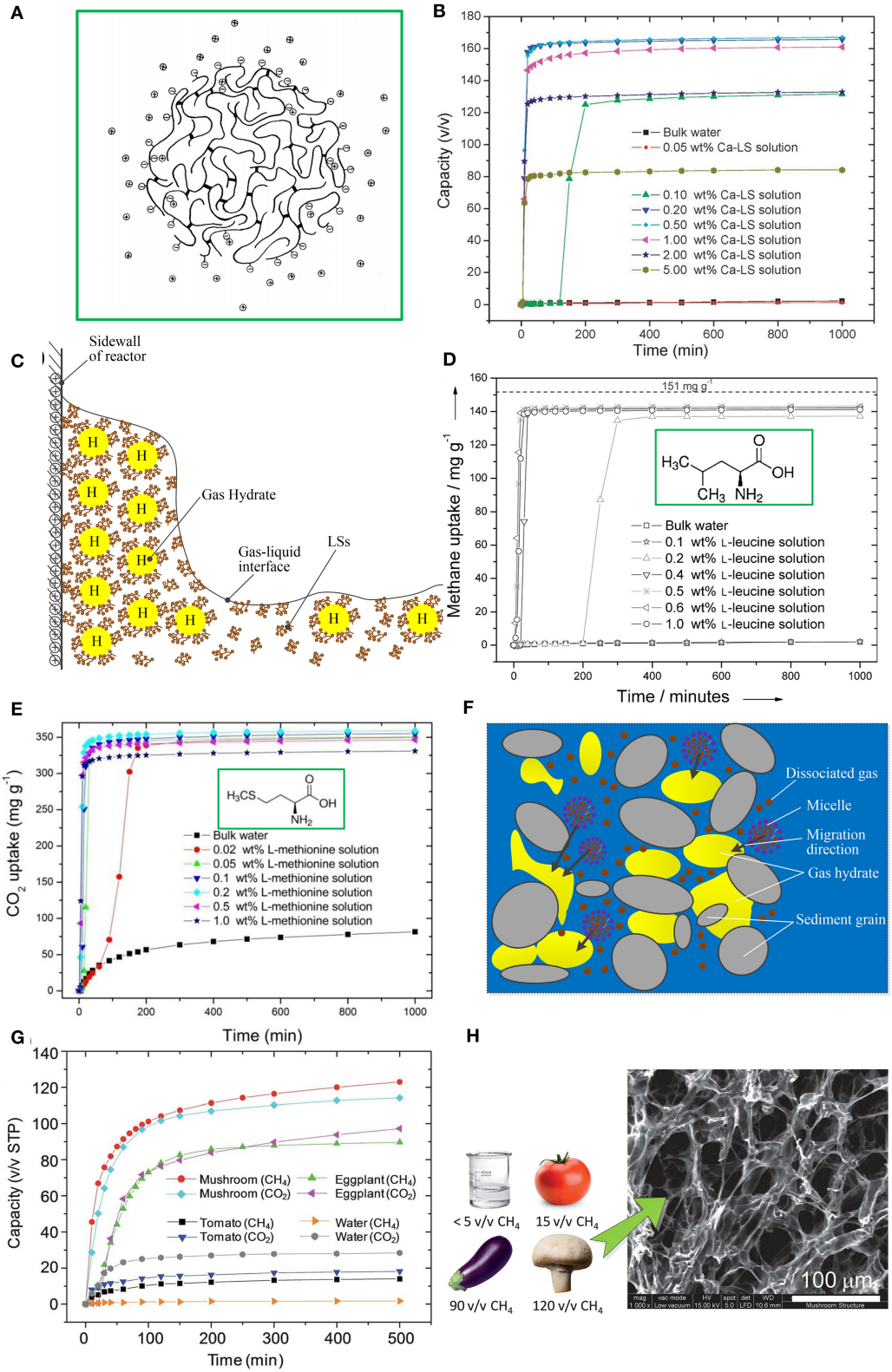

FIGURE 1 | (A) Spherical microgel model of an LS macromolecule. Reproduced from Rezanowich and Goring (1960) with permission from Elsevier. **(B)** CH_4 formation kinetics in a Ca-LS aqueous solution at 273.2 K and 9.5 MPa. Reproduced from Wang et al. (2012) with permission from the Royal Society of Chemistry.

(Continued)

FIGURE 1 | (C) Schematic diagram of the promoting mechanism of LSs. **(D)** CH_4 formation kinetics in a L-leucine aqueous solution at 273 K and 9.5 MPa. Reproduced from Liu et al. (2015) with permission from John Wiley and Sons. **(E)** CO_2 formation kinetics in L-methionine aqueous solution at 273.2 K and 3.3 MPa. Reproduced from Cai et al. (2017) with the permission from the John Wiley and Sons. **(F)** Schematic diagram of the promoting mechanism of biosurfactant in seabed sands/clay; **(G)** CH_4 and CO_2 formation kinetics for tomato, eggplant, and mushroom samples. Reproduced from Wang et al. (2013) with permission from the Royal Society of Chemistry. **(H)** SEM image of a mushroom sample showing a fine porous structure. Reproduced from Wang et al. (2013) with permission from the Royal Society of Chemistry.

chain of amino acids, ranging from a nonpolar alkyl chain to a charged or uncharged polar chain, plays a key role in their physico-chemical properties (Madeira et al., 2014).

Amino acids used for promoting gas hydrate formation were first reported by Liu et al. (2015). Leucine showed the best promoting effect for a CH_4 hydrate among the surveyed Amino acids. As shown in **Figure 1D**, CH_4 storage capacity reached 144 mg per g water (equivalent to a storage capacity of 161 v/v according to conversion Equation (1) in the **Supplementary Material**) and t_{90} was about 20 min. While for the CO_2 system, L-methionine showed the best promoting effect, as shown in **Figure 1E**, where CO_2 storage capacity reached 356 mg per g water (equivalent to a storage capacity of 144 v/v) and t_{90} was about 15 min (Cai et al., 2017). Summarizing previous studies, it can be found that for different guest gases the same amino acid will exert different effects. For example, L-histidine presented a promoting effect for a CH_4 hydrate (Bhattacharjee et al., 2016), while presenting an inhibiting effect for a CO_2 hydrate (Roosta et al., 2016). Leucine was reported to exert a poor promoting effect for an ethane hydrate and THF hydrate (Naeiji et al., 2014), but a favorable promoting effect for a CH_4 hydrate (Liu et al., 2015). For a CH_4 hydrate, the amino acids with a kinetic promoting effect are listed in order at concentration of 0.5 wt% as follows: L-leucine > L-isoleucine > D-leucine > L-methionine > L-phenylalanine > L-tryptophan > L-valine > L-arginine > L-glutamic acid > L-histidine > L-threonine (Liu et al., 2015). For CO_2 hydrate, the amino acids with a kinetic promoting effect are listed in order as follows: L-methionine > L-norleucine > L-tryptophan > L-norvaline > n-hexylamine at concentration of 0.2 wt% reported by Cai et al. (2017) and L-methionine > L-cysteine > L-valine > L-threonine > L-phenylalanine at concentration of 0.5 wt%, reported by Prasad and Kiran (2018).

Most authors think the promoting effect comes from the surface activity of amino acids generated by the amine group, carboxylic group, and side chain. Given that the amine group and carboxylic group have hydrophilic properties, the amino acids with an aromatic sided chain and hydrophobic properties generally present a promoting effect (Bavoh et al., 2019). The formation of a hydrate film on the gas-liquid interface at the initial formation stage reduces the diffusion of gas molecules from a gas phase to a liquid phase. The surface activity of amino acids can restrain the formation of this initial hydrate film, which enhances gas mass transfer. The forming hydrates in an amino acid aqueous solution are very flexible and expandable, which indicates that being capillarity-driven also plays a role in the growth phase of hydrates (Veluswamy et al., 2016). In addition, amino acids can chemically adsorb CO_2 molecules in a CO_2 system via a zwitterionic mechanism, which is speculated to influence CO_2 hydrate formation (Zhang et al., 2018). The CO_2 molecule firstly reacts with the amine group, producing a zwitterion, and then the zwitterion reacts with the amine group, producing amino acid salt. The CO_2 adsorption rate is related to the promoting effect of CO_2 hydrate formation (Bavoh et al., 2019).

Biosurfactant

Biosurfactants are secreted metabolites with surface activity during the metabolism of microorganisms under certain conditions. Microorganisms such as *Pseudomonas aeruginosa* and *Bacillus subtilis* were found from exploiting natural gas hydrate samples in the Gulf of Mexico (Lanoil et al., 2001). These two microorganisms can produce biosurfactants, i.e., rhamnolipid and surfactin, respectively, which has attracted the attention of hydrate researchers. Rhamnolipid is composed of 1-2 rhamnose rings (hydrophilic group) and saturated or unsaturated hydroxy fatty acids (hydrophobic group). Surfactin is a combination of a peptide ring containing 7 amino acid residues and β-hydroxy fatty acid containing 13-16 carbons by lactone bond (Arora et al., 2014).

Surfactin and rhamnolipid were first proven to have a promoting effect for natural gas hydrate formation in seawater-saturated sand/clay by Rogers et al. (2003), in which the hydrate formation rate increased by 96–288% and induction time decreased by 20–71%. Rhamnolipid was used as a co-promoter in a C-type silica-gel bed for promoting CH_4 hydrate formation (Arora et al., 2016). As a result, the hydrate formation rate increased by 42.97% and induction time decreased by 22.63%, compared with a C-type silica-gel bed with saturated pure water. Biosurfactants also exhibited comparability with SDS. According to the research of Jadav et al. (2017), for 200 ppm surfactin, rhamnolipid, and SDS aqueous solution, the conversion rate from CH_4 to hydrate was 42.7, 47.3, and 33.3%, and induction time was about 0.21, 0.23, and 1.13 h, respectively.

Biosurfactants have a lower critical micellar concentration (CMC) compared with synthetic surfactants (Arora et al., 2014). The CMC of the rhamnolipid seawater solution was about 13 ppm, which was easily achieved through minimal microbial activity in seabed sands/clay (Rogers et al., 2003). As shown in **Figure 1F**, the promoting effect of biosurfactants in seabed sands/clay was thought to be due to a micelle migration process, where micelles, dissolving hydrocarbon gas, migrated through seabed sand/clay with saturated seawater to the hydrate formation zone. On the other hand, both surfactin and rhamnolipid belong to anionic surfactants. Surfactin and rhamnolipid molecules can adsorb on the surface of hydrate particles to form a loose hydrate structure and enhance capillarity-driven action (Jadav et al., 2017). Rhamnolipid

presents a better promoting effect compared with surfactin. This may be due to the difference in molecular structure. The anionic groups in surfactin and rhamnolipid molecules are nitrogen bonding and carboxylate, respectively, while rhamnolipid has more tails than surfactin, which helps to enhance the adsorption of rhamnolipid molecules on the surface of hydrate particles (Jadav et al., 2017). Rhamnolipid with a concentration of not <0.5 wt% was proved to form well-dispersed CH_4 hydrate morphology in an oil-water system (Hou et al., 2018), which has an anti-agglomeration function. Besides, surfactin and rhamnolipid can also enhance mass transfer between the gas phase and liquid phase (Arora et al., 2014).

Biological Porous Structure

Various biological structures have evolved for tackling gas transport and enhancing mass transfer in nature, such as alveoli, gills, stoma of leaves, etc., which encourages scholars to find some natural biological structures for promoting gas hydrate formation. Wang et al. (2013) first studied the promoting effect of the biological porous structure from mushroom, eggplant, and tomato on CH_4 and CO_2 hydrate formation, as shown in **Figure 1G**. CH_4 storage capacity could reach 120 and 90 v/v within 500 min in mushroom and eggplant samples, respectively. CO_2 storage capacity was similar to CH_4 storage capacity. The better promoting effect benefits from the large surface-to-volume ratio and fine porous structure, as shown in **Figure 1H**, which improves gas mass transfer and helps to form loose gas hydrates with a biological porous structure as a framework. However, when mushroom and eggplant samples were used for the second hydrate cycle, there was a significant drop in gas storage capacity and formation rate. This was because the porous structure was destroyed after a hydrate-decomposition process.

Given that natural biological porous materials lack the structural stability for use in the recycling application of promoters in hydrate technologies, artificially biological structures may provide a better recycling stability. Nambiar et al. (2015) applied a porous cellulose foam fixed-bed for a hydrate-based CO_2 separation from a $CO_2/H_2/C_3H_8$ gas mixture. They found that, compared with the saturation level of 100%, a cellulose foam fixed-bed under a saturation level of 50% presented a better promoting effect, because there was more available gas for gas mass transfer and migration of water molecules in the porous structure during hydrate formation. Unfortunately, there was no report on the recycling performance of a cellulose foam fixed-bed in the paper.

CONCLUSION AND PROSPECT

This mini review summarizes the current status of already discovered biopromoters, including LSs, amino acids, biosurfactants, and biological porous structures. In general, the order of promoting effect from strong to weak is as follows: LSs > amino acids > biological porous structures > biosurfactants. The surface activity and capillarity-driven action of LSs, amino acids, and biosurfactants play key roles in promoting gas hydrate formation. A biological porous structure improves gas mass transfer and helps to form loose gas hydrates. The following research direction should earn more attention in the future:

(1) There is no consensus on the promoting mechanisms of biopromoters. Further study on promoting mechanisms is necessary, which would help to provide guidance for the selection of biologic materials as biopromoters.
(2) At present, biopromoters have not shown enough advantages to replace petrochemical-derived promoters in gas hydrate technologies, particularly given the promoting effect. The gas storage capacity under biopromoters can be better than that under petrochemical-derived promoters, but only at certain concentrations. However, there is still a gap between the formation rates of gas hydrate under biopromoters and petrochemical-derived promoters. Nature is a treasury of biologic materials. It is necessary to seek new promising natural biopromoters to achieve a higher formation rate.
(3) Artificially preparing biopromoters through chemical modification or by constructing a porous structure could be a promising approach for improving the promoting effect and recycling performance of promoters in hydrate technologies.

AUTHOR CONTRIBUTIONS

FW conceived the structure of the manuscript. F-LC collected materials and data. Y-TZ wrote the manuscript. S-JY wrote the **Supplementary Material**. FW revised and approved the manuscript.

FUNDING

This work was supported by the National Natural Science Foundation of China (21978142, 21706269), the Youth Innovation Talent Development Project for Universities of Shandong Province, and the Taishan Scholar Project of Shandong Province (ts20190937).

SUPPLEMENTARY MATERIAL

The Supplementary Material for this article can be found online at: https://www.frontiersin.org/articles/10.3389/fchem.2020.00514/full#supplementary-material

REFERENCES

Arora, A., Cameotra, S. S., Kumar, R., Balomajumder, C., Singh, A. K., Santhakumari, B., et al. (2016). Biosurfactant as a promoter of methane hydrate formation: thermodynamic and kinetic studies. *Sci. Rep.* 6, 1–13. doi: 10.1038/srep20893

Arora, A., Cameotra, S. S., Kumar, R., Kumar, P., and Balomajumder, C. (2014). Effects of biosurfactants on gas hydrates. *J.*

Petrol. Environ. Biotechnol. 5:170. doi: 10.4172/2157-7463.1000170

Bavoh, C. B., Lal, B., Osei, H., Sabil, K. M., and Mukhtar, H. (2019). A review on the role of amino acids in gas hydrate inhibition, CO_2 capture and sequestration, and natural gas storage. *J. Nat. Gas Sci. Eng.* 64, 52–71. doi: 10.1016/j.jngse.2019.01.020

Bhattacharjee, G., Choudhary, N., Kumar, A., Chakrabarty, S., Kumar, R., et al. (2016). Effect of the amino acid l-histidine on methane hydrate growth kinetics. *J. Nat. Gas Sci. Eng.* 35, 1453–1462. doi: 10.1016/j.jngse.2016.05.052

Cai, Y., Chen, Y., Li, Q., Huang, H., Wang, S., Wang W., et al. (2017). CO_2 Hydrate formation promoted by a natural amino acid l-methionine for possible application to CO_2 capture and storage. *Energy Technol.* 5, 1195–1199. doi: 10.1002/ente.201600731

Chong, Z. R., Yang, M., Khoo, B. C., and Linga, P. (2016). Size effect of porous media on methane hydrate formation and dissociation in an excess gas environment. *Ind. Eng. Chem. Res.* 55, 7981–7991. doi: 10.1021/acs.iecr.5b03908

Daniel-David, D., Guerton, F., Dicharry, C., Torré, J. P., and Broseta, D. (2015). Hydrate growth at the interface between water and pure or mixed CO_2/CH_4 gases: Influence of pressure, temperature, gas composition and water-soluble surfactants. *Chem. Eng. Sci.* 132, 118–127. doi: 10.1016/j.ces.2015.04.015

Dicharry, C., Diaz, J., Torré, J. P., and Ricaurte, M. (2016). Influence of the carbon chain length of a sulfate-based surfactant on the formation of CO_2, CH_4 and CO_2-CH_4 gas hydrates. *Chem. Eng. Sci.* 152, 736–745. doi: 10.1016/j.ces.2016.06.034

Gupta, C., and Washburn, N. R. (2014). Polymer-grafted lignin surfactants prepared via reversible addition-fragmentation chain-transfer polymerization. *Langmuir* 30, 9303–9312. doi: 10.1021/la501696y

He, Y., Sun, M. T., Chen, C., Zhang, G. B., Chao, K., Lin, Y., et al. (2019). Surfactant-based promotion to gas hydrate formation for energy storage. *J. Mater. Chem. A* 7, 21634–21661. doi: 10.1039/C9TA07071K

Hou, G., Liang, D., and Li, X. (2018). Experimental study on hydrate anti-agglomeration in the presence of rhamnolipid. *RSC Adv.* 8, 39511–39519. doi: 10.1039/c8ra07215a

Jadav, S., Sakthipriya, N., Doble, M., and Sangwaia, J. S. (2017). Effect of biosurfactants produced by *Bacillus subtilis* and *Pseudomonas aeruginosa* on the formation kinetics of methane hydrates. *J. Nat. Gas Sci. Eng.* 43, 156–166. doi: 10.1016/j.jngse.2017.03.032

Lanoil, B. D., Sassen, R., La Duc, M. T., Sweet, S. T., and Nealson, K. H. (2001). Bacteria and archaea physically associated with gulf of Mexico gas hydrates. *Appl. Environ. Microbiol.* 67, 5143–5153. doi: 10.1128/AEM.67.11.5143-5153.2001

Lewis, M. A. (1991). Chronic and sublethal toxicities of surfactants to aquatic animals: a review and risk assessment. *Water Res.* 25, 101–113. doi: 10.1016/0043-1354(91)90105-Y

Liu, Y., Chen, B., Chen, Y., Zhang, S., Guo, W., Cai, Y., et al. (2015). Methane storage in a hydrated form as promoted by leucines for possible application to natural gas transportation and storage. *Energy Technol.* 3, 815–819. doi: 10.1002/ente.201500048

Madeira, P. P., Bessa, A., Álvares-Ribeiro, L., Aires-Barros, M. R., Rodrigues, A. E., Uversky, V. N., et al. (2014). Amino acid/water interactions study: a new amino acid scale. *J. Biomol. Struct. Dyn.* 32, 959–968. doi: 10.1080/07391102.2013.800994

Mofrad, H. R., Ganji, H., Nazari, K., Kameli, M., Rezaie Rod, A., Kakavand, K., et al. (2016). Rapid formation of dry natural gas hydrate with high capacity and low decomposition rate using a new effective promoter. *J. Pet. Sci. Eng.* 147, 756–759. doi: 10.1016/j.petrol.2016.10.002

Myrvold, B. O. (2008). A new model for the structure of lignosulphonates: Part 1. behaviour in dilute solutions. *Ind. Crop. Prod.* 27, 214–219. doi: 10.1016/j.indcrop.2007.07.010

Naeiji, P., Arjomandi, A., and Varaminian, F. (2014). Amino acids as kinetic inhibitors for tetrahydrofuran hydrate formation: experimental study and kinetic modeling. *J. Nat. Gas Sci. Eng.* 21, 64–70. doi: 10.1016/j.jngse.2014.07.029

Nambiar, A., Babu, P., and Linga, P. (2015). CO_2 capture using the clathrate hydrate process employing cellulose foam as a porous media. *Can. J. Chem.* 93, 808–814. doi: 10.1139/cjc-2014-0547

Prasad, P. S. R., and Kiran, B. S. (2018). Are the amino acids thermodynamic inhibitors or kinetic promoters for carbon dioxide hydrates? *J. Nat. Gas Sci. Eng.* 52, 461–466. doi: 10.1016/j.jngse.2018.02.001

Rezanowich, A., and Goring, D. A. I. (1960). Polyelectrolyte expansion of a lignin sulfonate microgel. *J. Colloid Sci.* 15, 452–471. doi: 10.1016/0095-8522(60)90049-0

Rogers, R. E., Kothapalli, C., Lee, M. S., and Woolsey, J. L. (2003). Catalysis of Gas Hydrates by Biosurfactants in Seawater-Saturated Sand/Clay. *Can. J. Chem. Eng.* 81, 973–980. doi: 10.1002/cjce.5450810508

Roosta, H., Dashti, A., Mazloumi, S. H., and Varaminian, F. (2016). Inhibition properties of new amino acids for prevention of hydrate formation in carbon dioxide-water system: Experimental and modeling investigations. *J. Mol. Liq.* 215, 656–663. doi: 10.1016/j.molliq.2016.01.039

Siangsai, A., Rangsunvigit, P., Kitiyanan, B., Kulprathipanja, S., and Linga, P. (2015). Investigation on the roles of activated carbon particle sizes on methane hydrate formation and dissociation. *Chem. Eng. Sci.* 126, 383–389. doi: 10.1016/j.ces.2014.12.047

Sun, Q., and Kang, Y. T. (2016). Review on CO_2 hydrate formation/dissociation and its cold energy application. *Renew. Sust. Energ. Rev.*, 62, 478–494. doi: 10.1016/j.rser.2016.04.062

Veluswamy, H. P., Hong, Q. W., and Linga, P. (2016). Morphology study of methane hydrate formation and dissociation in the presence of amino acid. *Cryst. Growth Des.* 16, 5932–5945. doi: 10.1021/acs.cgd.6b00997

Veluswamy, H. P., Kumar, A., Seo, Y., Lee, J. D., and Linga, P. (2018). A review of solidified natural gas (SNG) technology for gas storage via clathrate hydrates. *Appl. Energy* 216, 262–285. doi: 10.1016/j.apenergy.2018.02.059

Wang, F., Guo, G., Luo, S. J., Guo, R. B. (2017). Preparation of $-SO_3^-$-coated nanopromoters for methane hydrate formation: effects of the existence pattern of $-SO_3^-$ groups on the promotion efficiency. *J. Mater. Chem. A.* 5, 2640–2648. doi: 10.1039/C6TA08839B

Wang, W., Ma, C., Lin, P., Sun, L., and Cooper, A. I. (2013). Gas storage in renewable bioclathrates. *Energy Environ. Sci.* 6, 105–107. doi: 10.1039/c2ee23565j

Wang, W. X., Huang, Z., Chen, H. R., Tan, Z., Chen, C., and Sun, L. (2012). Methane hydrates with a high capacity and a high formation rate promoted by biosurfactants. *Chem. Commun.* 48, 11638–11640. doi: 10.1039/C2CC35603A

Yi, J., Zhong, D. L., Yan, J., and Lu, Y. Y. (2019). Impacts of the surfactant sulfonated lignin on hydrate based CO_2 capture from a CO_2/CH_4 gas mixture. *Energy* 171, 61–68. doi: 10.1016/j.energy.2019.01.007

Zhang, Z., Li, Y., Zhang, W., Wang, J., Soltanian, M. R., and Olabi, A. G. (2018). Effectiveness of amino acid salt solutions in capturing CO_2: a review. *Renew. Sust. Energ. Rev.* 98, 179–188. doi: 10.1016/j.rser.2018.09.019

Conflict of Interest: The authors declare that the research was conducted in the absence of any commercial or financial relationships that could be construed as a potential conflict of interest.

frontiers in Chemistry

ORIGINAL RESEARCH
published: 16 July 2020
doi: 10.3389/fchem.2020.00547

Thermophysical Property Measurements of Tetrabutylphosphonium Oxalate (TBPOx) Ionic Semiclathrate Hydrate as a Media for the Thermal Energy Storage System

Takashi Miyamoto[1], *Ryo Koyama*[1], *Naruki Kurokawa*[1], *Atsushi Hotta*[1], *Saman Alavi*[2] *and Ryo Ohmura*[1]*

[1] Department of Mechanical Engineering, Keio University, Tokyo, Japan, [2] Department of Chemistry and Biomolecular Sciences, Ottawa University, Ottawa, ON, Canada

OPEN ACCESS

Edited by:
Amadeu K. Sum, Colorado School of Mines, United States

Reviewed by:
Mohammad Tariq, Universidade NOVA de Lisboa, Portugal
Didier Dalmazzone, École Nationale Supérieure de Techniques Avancées, France

***Correspondence:**
Ryo Ohmura
rohmura@mech.keio.ac.jp

Specialty section:
This article was submitted to Physical Chemistry and Chemical Physics, a section of the journal Frontiers in Chemistry

Received: *19 March 2020*
Accepted: *27 May 2020*
Published: *16 July 2020*

Citation:
Miyamoto T, Koyama R, Kurokawa N, Hotta A, Alavi S and Ohmura R (2020) Thermophysical Property Measurements of Tetrabutylphosphonium Oxalate (TBPOx) Ionic Semiclathrate Hydrate as a Media for the Thermal Energy Storage System. Front. Chem. 8:547. doi: 10.3389/fchem.2020.00547

With increasing global power demand, thermal energy storage technology could play a role ensuring a sustainable energy supply in power generation from renewable energy sources and power demand concentration. Hydrates have high potential as phase change materials (PCMs) for the use as a thermal energy storage medium. To develop thermal energy storage technology using a hydrate-based material, further investigation of thermophysical properties and the selection of a suitable hydrate are required. Tetrabutylphosphonium oxalate (TBPOx) ionic semiclathrate hydrate contains oxalic acid in salt form, as a guest compound, which is classified as carboxylic acid group with low environmental impact. In the present study, the phase equilibrium temperature and the dissociation heat of TBPOx hydrate were measured. The highest equilibrium temperature of the solid hydrate formed was 9.4°C at the mass fraction 0.35 of TBPOx in aqueous solution. The largest dissociation heat was 186.0 ± 0.5 kJ·kg^{-1} at the mass fraction of 0.35. Comparing with other PCMs with close phase equilibrium temperatures, TBPOx hydrate is superior in safety and sustainability. These results indicate that TBPOx hydrate would be suitable as the thermal storage medium for the general air conditioning systems.

Keywords: ionic semiclathrate hydrate, tetrabutylphosphonium oxalate (TBPOx), carboxylic acid, phase equilibrium temperature, dissociation heat, phase change material (PCM), thermal energy storage medium

INTRODUCTION

To deal with the world energy consumption issue, modern society needs energy management to relieve the concentration of electricity demand, which leads to emission of greenhouse gas from power generation (International Energy Agency IEA World Energy Outlook, 2019). The amount of generated electricity throughout the day depends on the time of day at a particular location. The energy use in the daytime tends to be higher than the night time. Additionally, renewable energy technology utilizing sources such as solar and wind power depends on the operating environment. These energy sources are unfavorable to achieve a stable electricity supply at all times. Current energy supply system management requires solutions to close the huge gap between the

production and consumption of the energy, particularly when the contributions from renewable energy are included.

Thermal energy storage systems could help to change these imbalances between energy supply and demand (Pielichowska and Pielichowski, 2014; Veerakumar and Sreekumar, 2015; Pelay et al., 2017). The thermal energy storage is the technology that stores heat energy using the heat capacity of substances. At night, the surplus electricity would be stored as the cold energy in advance of the daytime peak in power usage. When daytime power demand increases, by using the cold thermal energy stored in the substances, it could help to reduce the total electricity that needs to be generated. These systems use phase change materials (PCMs) as the thermal energy storage medium. These substances can utilize latent heat adding to sensible heat and have higher energy density than sensible heat storage (Mehling and Cabeza, 2007, 2008).

The main categories of PCMs are organic and inorganic compounds in solid–liquid PCMs (Pielichowska and Pielichowski, 2014; Veerakumar and Sreekumar, 2015). The organic PCMs are represented by paraffin, and the typical examples of the inorganic PCMs are metal salt hydrates and water. Having flammability and low thermal conductivity, organic PCMs have safety issues (Zalba et al., 2003). Metal salt hydrates have corrosiveness and need high temperatures to melt (Veerakumar and Sreekumar, 2015). With those characteristics, metal salt hydrates are not suitable for long-term use. Water is often used as ice. Despite having the large latent heat, the freezing point of ice is relatively low. Therefore, the available temperature range of ice is limited. Instead of these compounds, recent studies proposed clathrate hydrates or more simply hydrates as thermal energy storage medium (Li et al., 2012; Castellani et al., 2014; Oshima et al., 2018).

Clathrate hydrates are crystalline compounds consisting of the space-filling cages of water molecules and other molecules called guest compounds enclosed within the cages. They show various physical properties depending on the type of guest compounds contained (Nakayama and Hashimoto, 1980; Nakayama et al., 1983; Mayoufi et al., 2011; Sakamoto et al., 2011; Sato et al., 2013; Yamauchi et al., 2017a,b; Arai et al., 2018; Shimada et al., 2018, 2019). Ionic semiclathrate hydrates have unique structures. The anion of guest molecules replaces water molecules of the cage and the cation of guests is enclosed within the hydrogen-bonded water molecules cages. In the process of synthesizing ionic semiclathrate hydrates, tetrabutylammonium (TBA) salts or tetrabutylphosphonium (TBP) salts have mainly been found convenient for use. With the hydrogen bonding between water within the cage molecules, and the strong interaction between the guest and water molecules, these substances have large dissociation heats (Alavi and Ohmura, 2016). The decomposition phase transformation of ionic semiclathrate hydrates can occur under atmospheric pressure and around the room temperature. Consisting of water molecules, they are flame-retardant compounds. Based on these beneficial properties, the ionic semiclathrate hydrates can be used as PCM.

In recent years, tetrabutylammonium bromide (TBAB) hydrate has been commercialized as PCM for the air conditioning refrigerant (Darbouret et al., 2005; Wang and Dennis, 2015). It is the only commercialized semiclathrate hydrate and includes a bromide halogen ion within the guest compounds. The previous studies reported the equilibrium temperature of TBAB hydrate as 12.7°C and the largest dissociation heat as 193.2 $kJ \cdot kg^{-1}$ (Oyama et al., 2005; Kobori et al., 2015). Data of thermophysical property are essential to select suitable materials as thermal energy storage media. For the development of thermal energy storage technology, similar experiments on other hydrates should be conducted.

The semiclathrate hydrates composed with anions with carboxylic acid anions in the guest compounds have been previously investigated (Nakayama and Torigata, 1984; Yamauchi et al., 2017a,b; Arai et al., 2018; Shimada et al., 2018, 2019). Carboxylic acid anion containing compounds are more environmentally benign, unlike those which incorporate halide anions. The previous studies of ionic semiclathrate hydrates with carboxylic acid anions imply the existence of relationships between thermophysical properties of ionic semiclathrate hydrates and the molar mass of the guest compounds. From the trend of physical property values, the heats of dissociations are expected to be large when the range of molar mass of the carboxylic acid in the guest compounds is from 60 to 90 $kg \cdot kmol^{-1}$.

Tetrabutylphosphonium oxalate (TBPOx) hydrate is an ionic semiclathrate hydrate consisting oxalic acid as the guest compound in oxalate anion form. The molar mass of oxalic acid is 90.03 $kg \cdot kmol^{-1}$, and this corresponds to the molar mass range of the carboxylic acid of the guest group in semiclathrate hydrates that are expected to have large dissociation heat. A previous study reported on the synthesis and properties of the ionic semiclathrate hydrate with the oxalic acid anion, namely, tetrabutylammonium oxalate (TBAOx) hydrate (Dyadin et al., 1976). The highest phase equilibrium temperature of TBAOx hydrate is reported as 16.2°C. However, no data about the other thermophysical properties were measured. The phase equilibrium temperatures of TBP hydrates have the tendency to be lower than those of TBA hydrates when both hydrates have the same guest anions (Kobori et al., 2015). By using TBP salt instead of TBA salt, the phase equilibrium temperature of TBPOx hydrate could be expected to be lower than TBAOx and it would meet the required temperature of the cooling medium for the air conditioning systems (ASRAE, 2016).

TBP hydrates consisting of carboxylic acid anions were reported in the previous studies (Arai et al., 2018; Shimada et al., 2018, 2019). Further investigation of the thermophysical properties of hydrate will lead to expand the application range of hydrates. Depending on the obtained properties, it could be applied to the various hydrate technologies. In this study, phase equilibrium temperatures and dissociation heats of TBPOx hydrate were measured.

MATERIALS AND METHODS

Materials

The materials used in this study are summarized in **Table 1**. TBPOx aqueous solutions were obtained by neutralizing

TABLE 1 | Specifications of materials used in this study.

Name	Chemical formula[b]	Supplier	Purity
Oxalic acid	$H_2C_2O_4$	Sigma-Aldrich Co. LLC.	0.98 content in anhydrous solid
Tetrabutylphosphonium hydroxide (TBPOH) aqueous solutions	$(CH_3CH_2CH_2CH_2)_4POH$	Sigma-Aldrich Co. LLC.	0.40 mass fraction in aqueous solution[a]
Water	H_2O	Laboratory made	Electrical conductivity was $<0.1\ \mu S{\cdot}cm^{-1}$
Tetrabutylphosphonium oxalate (TBPOx) aqueous solutions	$[(CH_3CH_2CH_2CH_2)_4P]_2C_2O_4$	Laboratory made with above materials	The standard uncertainty of mass fraction was $\pm\ 5.0 \times 10^{-3}$ [b]
Hydrochloric acid	HCl	Kanto chemical Co. Inc.	0.01 $mol{\cdot}L^{-1}$ [c]

[a] *This is the labeled mass fraction on the reagent bottle. The concentration with the uncertainty of TBPOH aqueous solution was measured by acid-based titration with HCl. The actual mass fraction of TBPOH aqueous solution was 0.41. The standard uncertainty of the mass fraction was* 5.0×10^{-3}.

[b] *The uncertainties of the mass fraction of TBPOx aqueous solution were estimated from the uncertainties of the mass measurements on TBPOH aqueous solution, oxalic acid solution, and water on the neutralizing and adjusting processes.*

[c] *HCl was utilized for the titration measurement to determine the uncertainty for mass fraction of TBPOH aqueous solution.*

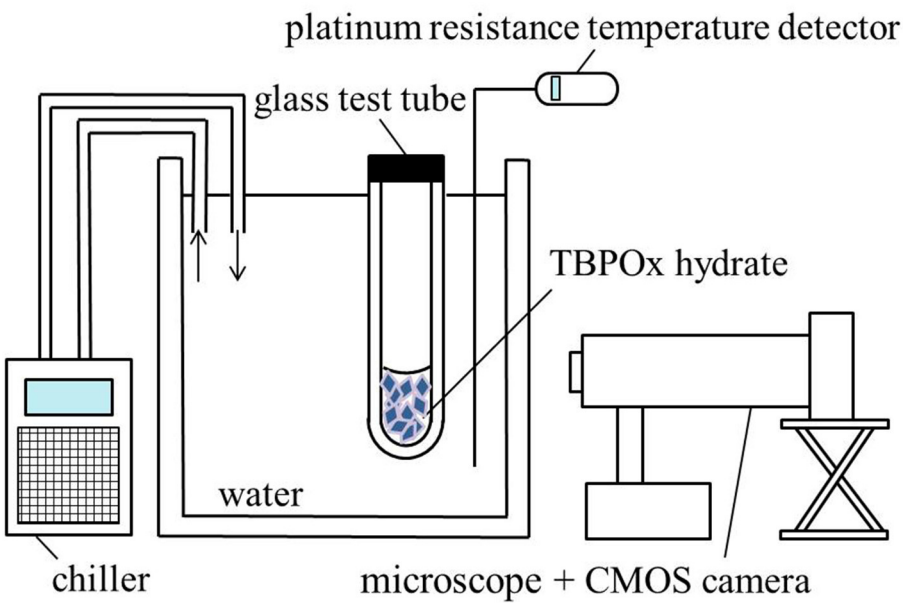

FIGURE 1 | Schematic diagram of the equipment for the measurement of the phase equilibrium temperature.

tetrabutylphosphonium hydroxide (TBPOH) aqueous solutions (0.40 mass fraction in aqueous solution, Sigma-Aldrich Co., LLC.) with oxalic acid (0.98 content in anhydrous solid, FUJIFILM Wako Pure Chemical Co., Ltd.). Before the neutralization, oxalic acid solid and distilled water in the vessels were warmed with hot water until oxalic acid solid was completely dissolved in the solution. The distilled water for the concentration adjustment was made by a water distillation unit (Yamato Scientific Co., Ltd., WG 222) in the laboratory. In this study, the samples of TBPOx aqueous solution were made at the mass fraction range from 0.20 to 0.40. The mass of oxalic acid, water, and TBPOx aqueous solution was measured by an electronic balance (IUW-200D sefi, As One Co., LLC.) with an expanded uncertainty of ± 0.1 mg (coverage factor $k = 2$).

Equilibrium Temperature Measurement

The schematic diagram of experimental equipment used for observing the dissociation of TBPOx hydrate crystal is shown on **Figure 1**. Approximately 0.5 g of TBPOx aqueous solution samples in the glass test tubes was refrigerated at -20°C for 24 h to form the hydrate crystals. After visually confirming the hydrate formation, the glass test tubes (external diameter 10 mm, internal diameter 8 mm, height 90 mm) within the hydrate crystal were set into the water bath under the atmospheric pressure. The temperature of the water was measured by a platinum resistance temperature detector with an expanded uncertainty of $\pm 0.1^{\circ}$C (coverage factor $k = 2$) and controlled by a chiller (Tokyo Rikakikai Co., CTP-3000). The system temperature was maintained constant for at least 4 h. The crystal dissociation behavior was visually observed by a CMOS camera with a microscope. If no remarkable change was seen on the crystals,

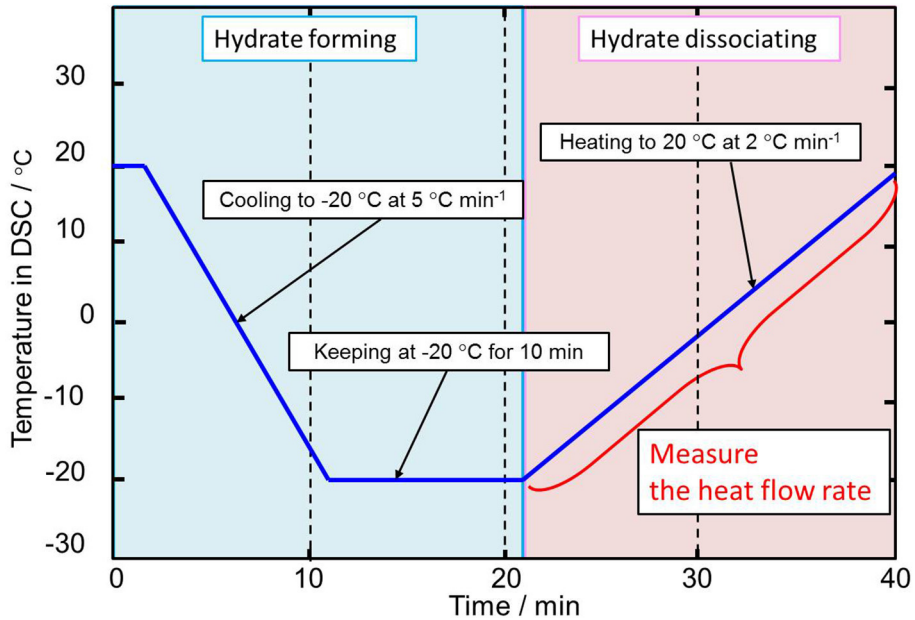

FIGURE 2 | Schematic diagram of the DSC temperature program for the dissociation heat measurement.

the system temperature was increased by 0.1°C and maintained constant another several hours again. When the dissociation was observed, the system was kept at the same temperature for several hours. By repeating these procedures, the hydrate crystals were completely dissociated. The equilibrium temperature was the temperature just before complete dissociation. Therefore, the equilibrium temperature was determined as 0.1°C lower than the dissociation temperature.

The measurements were performed at least three times at each mass fraction. Three different samples prepared from three different TBPOx aqueous solutions were measured for a given mass fraction. The visual observations with the similar apparatus and method were performed in the previous studies (Yamauchi et al., 2017a,b; Arai et al., 2018, 2019; Shimada et al., 2018; Koyama et al., 2019). These studies supported the reliability of the equilibrium temperature obtained in this study.

Dissociation Heat Measurement

The dissociation heats of TBPOx hydrate were measured by the differential scanning calorimetry (abbreviated as DSC) (TA Instrument, DSC25). For the temperature and latent heat calibration, indium (purity 99.99%) and distilled water were used. The uncertainty of enthalpy was confirmed by measuring the latent heat of water three times. The average of three measurements was 335.7 kJ·kg^{-1} and the uncertainty of the dissociation heat measurements was estimated to be 3.2 kJ·kg^{-1} (coverage factor $k = 2$), which was consistent with the literature data within the experimental uncertainty (Feistel and Wagner, 2006).

Approximately 15 mg of sample from TBPOx aqueous solution and air was encapsulated into the aluminum test cell as a sample and a reference. The test cells have a volume of 40×10^{-3} cm^3. The sample cell and the test cell were placed inside the DSC device filled with dry N_2 gases at 0.1 MPa to eliminate moisture.

The temperature in the DSC was controlled as shown in **Figure 2**. First, the temperature was kept for 20°C to dry the internal device, and then it was decreased from 20 to −20°C under a cooling rate of −5°C min^{-1} to form the hydrate crystals. After keeping at −20°C for 10 min to complete the formation of the hydrate crystals, the system temperature was increased from −20°C to 20°C under a heating rate of 2°C min^{-1} to dissociate the hydrate crystals. The reliability of the higher heating rate of 2°C min^{-1} used in this process in determining the dissociation temperature was shown in previous studies (Yamauchi et al., 2017a; Arai et al., 2018; Shimada et al., 2018).

During the hydrate dissociating process, the heat flow rate, which was normalized per unit mass, was measured. Then, the dissociation heat of TBPOx hydrate was obtained by integrating the endothermic peak of the heat flow rate. As the equilibrium temperature measurement, triplicate measurements were performed at each mass fraction of TBPOx solutions. Three independent measurements were performed with three different samples for a given mass fraction.

RESULTS AND DISCUSSION

Phase Equilibrium Temperatures

Phase equilibrium temperatures of TBPOx hydrate were measured at the mass fraction range from 0.20 to 0.40 under the atmospheric pressure by visual observation. The visual observation images of hydrate dissociation at a mass fraction of 0.35 are shown in **Figure 3**. This figure also reveals the experimental process to measure the equilibrium temperature

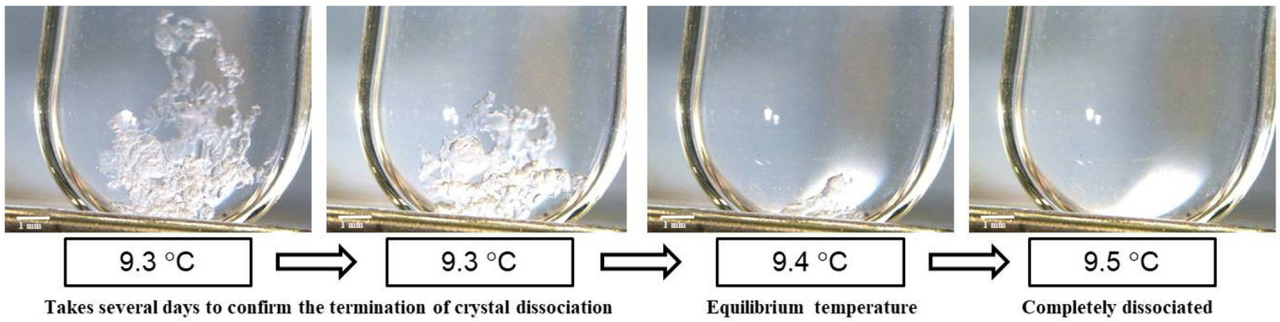

FIGURE 3 | The visual observation during TBPOx hydrate dissociation.

TABLE 2 | The phase equilibrium temperatures of TBPOx hydrate.

w_{TBPOx}[a]	x_{TBPOx}[b]	T_{eq}[c] (°C)
0.20	0.0074	6.2
0.25	0.0098	7.6
0.30	0.0126	8.6
0.34	0.0151	9.3
0.35	0.0157	9.4
0.36	0.0164	9.3
0.37	0.0171	9.2
0.38	0.0180	9.2
0.39	0.0186	9.3
0.40	0.0194	8.0

[a] *The standard uncertainty u (w_{TBPOx}) is ± 5.0 × 10^{-3}.*
[b] *The standard uncertainty u (w_{TBPOx}) is ± 4.0 × 10^{-4}. x_{TBPOx} indicates the mole fraction of TBPOx in aqueous solutions. These values of mole fractions were obtained by converting the mass fractions.*
[c] *The expanded uncertainty U (T_{eq}) is ± 0.1 K (k = 2).*

of TBPOx hydrate. Near the equilibrium temperature, it took several days to confirm the termination of hydrate dissociation with one step of increasing temperature. Constant temperature increasing methods, like DCS measurement, would not be suitable for the observation of the slow hydrate dissociation dynamics. These results obtained from the process similar to **Figure 3** are presented in **Table 2**, where w_{TBPOx}, x_{TBPOx}, and T_{eq}, respectively, indicate the mass fraction, the mole fraction of TBPOx aqueous solution, and the phase equilibrium temperatures.

In the measurement, the maximum points were confirmed at a mass fraction of 0.35. The phase equilibrium temperatures significantly increased with the mass fraction at a mass fraction range below 0.34. In the ranges from 0.34 to 0.35, the phase equilibrium temperature showed a slight increase. Then, the phase equilibrium temperatures gradually decreased with the mass fraction increase in the range from 0.35 to 0.39. For the solutions over the mass fraction range 0.39, the phase equilibrium temperatures sharply decreased.

In the previous studies of ionic semiclathrate hydrates, similar tendencies of temperature increase and decrease with mass fraction in solution were reported (Yamauchi et al., 2017a,b; Arai et al., 2018, 2019; Shimada et al., 2018, 2019). From the low mass fraction to a specific mass fraction for each ionic semiclathrate hydrate, the phase equilibrium temperature tended to rise with the increase of the mass fraction. After a specific mass fraction, the phase equilibrium temperature decreased with the increase of the mass fraction in solution. At that specific mass fraction, the highest phase equilibrium temperature was observed. The previous studies also reported that the congruent point would be at the mass fraction of the highest phase equilibrium temperature (Yamauchi et al., 2017a,b; Arai et al., 2018, 2019; Shimada et al., 2018, 2019; Koyama et al., 2019).

In the present study, the congruent point would exist at the range of mass fraction 0.34 to 0.36. The highest phase equilibrium temperature was 9.4°C at the mass fraction 0.35, which met the required temperature of the cooling medium for the air conditioning system from 5 to 15°C (ASRAE, 2016).

Heat Flow and Dissociation Heat

The dissociation heats of TBPOx hydrate were deduced from the data of the heat flow rates. In obtaining the dissociation heats, the baseline was drawn from the start to the end of the heat flow peak to integrate the heat flow rates. TBPOx solutions were injected into the aluminum pan, which is the test section. In the present measurements, the thermal behavior of TBPOx hydrates formed inside the pans was observed. The heat flow rates were measured by DSC at nine different mass fractions from 0.20 to 0.40. The results are presented in **Figures 4**–**7**. As shown in **Figure 4**, three representative heat flows were respectively obtained in the measurement range at each mass fraction 0.30, 0.38, and 0.40.

The first peak of the mass fraction 0.30 at a temperature around 0°C emerged due to ice melting, which was observed at low mass fraction in the measurement range. The ice would be formed by residual water that was not consumed for hydrate crystal formation. The largest peak of the mass fraction 0.30, 0.38, and 0.40 at a temperature around 10°C was due to hydrate dissociation, which was obtained at almost all mass fractions in the present measurements. Considering the starting point of the heat flow, the small peak at the temperature around 5°C was not caused by the ice melting. This temperature indicated that

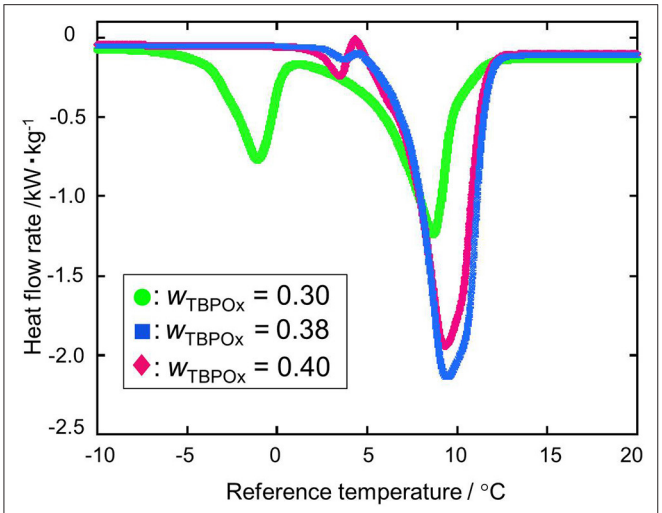

FIGURE 4 | The heat flow rate at the mass fractions 0.30, 0.38, and 0.40: green ●, $w_{TBPOx} = 0.30$; blue ■, $w_{TBPOx} = 0.38$; red ♦, $w_{TBPOx} = 0.40$.

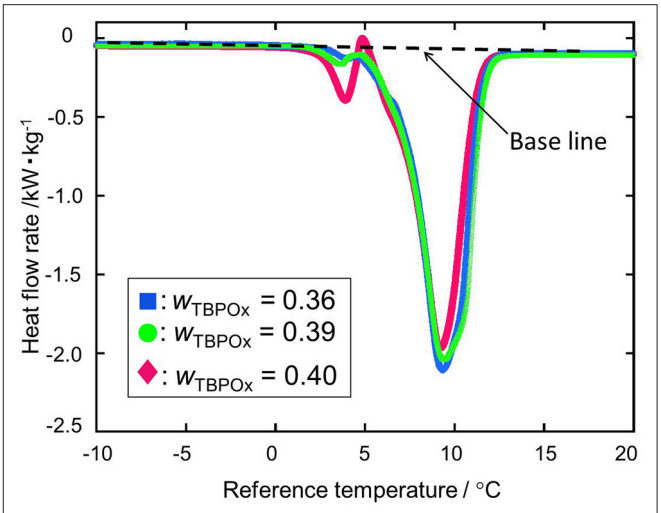

FIGURE 6 | The heat flow rate at the mass fractions 0.36, 0.39, and 0.40: blue ■, $w_{TBPOx} = 0.36$; green ●, $w_{TBPOx} = 0.39$; red ♦, $w_{TBPOx} = 0.40$.

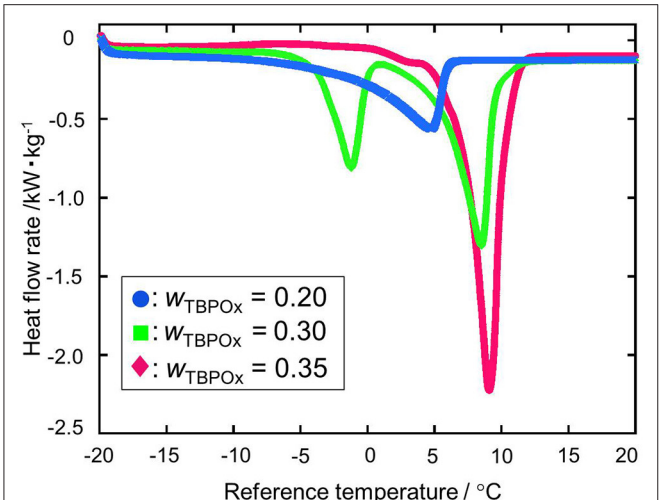

FIGURE 5 | The heat flow rate at the mass fractions 0.20, 0.30, and 0.35: blue ●, $w_{TBPOx} = 0.20$; green ■, $w_{TBPOx} = 0.30$; red ♦, $w_{TBPOx} = 0.35$.

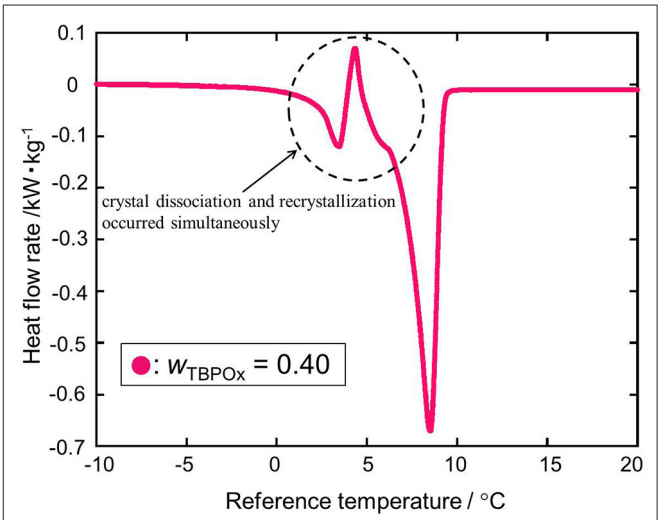

FIGURE 7 | The heat flow rate at the mass fractions 0.40 with the heating rate of 0.5°C/min: red ●, $w_{TBPOx} = 0.40$.

the small peak was due to the dissociation of a hydrate phase, which has a different equilibrium temperature from the hydrate dissociated around 10°C. Polymorphism was observed in the previous studies of ionic semiclathrate hydrates (Oyama et al., 2005; Sakamoto et al., 2011; Yamauchi et al., 2017a,b; Arai et al., 2018, 2019). In the TBPOx hydrate system, at least two types of hydrates with different thermophysical properties and crystal structures would exist at a mass fraction of 0.40.

Figure 5 shows the heat flows at the mass fraction range from 0.20 to 0.35. The heat flow curves significantly changed with the increase in mass fraction. At the mass fraction 0.20, the endothermic peak due to ice melting did not appear around 0°C. The peak appearing at the midpoint between 0 and 10°C was due to only hydrate dissociation. Since the nucleation of ice is a stochastic phenomenon, no ice formation from the residual water occurred at a solution mass fraction of 0.20. From the mass fraction 0.30 to 0.35, the hydrate dissociation peak increased while the ice melting peak decreased. The deepest peak was observed at the mass fraction 0.35.

Figure 6 shows two kinds of heat flows at mass fractions from 0.36 to 0.40. In this range, the endothermic peak due to ice melting was not observed. From the mass fraction 0.36 to 0.39, hydrate dissociation peaks with similar shapes appeared at the temperature around 10°C. The depths of those peaks tend to slightly decrease with the increase in solution TBPOx mass fraction. At the mass fraction 0.40, the small endothermic peak and exothermic peak were observed at a temperature of around 5°C. After the appearance of those small peaks, the

deep dissociation peak, similar to the mass fraction 0.36 to 0.39, emerged.

At the mass fraction range smaller than the hydrate composition, with increase of the mass fraction in solution, more hydrate crystals formed. Those crystals resulted in the larger peak due to hydrate dissociation. With the hydrate crystal formation, the amount of residual water in the aqueous solution decreased. Therefore, the ice melting peak tends to decrease as the mass fraction increased. This tendency was observed at the mass fraction range from 0.20 to 0.35 shown in **Figure 4**. When the mass fraction of the aqueous solution was equal to the hydrate composition, the largest amount of hydrate should be formed. After hydrate formation, no residual water existed in the test section. That means ice melting peak that emerged from the water may not appear at this mass fraction. Those results may lead to the deepest single peak of hydrate dissociation at a mass fraction of 0.35. At the mass fraction range larger than the hydrate composition, the amount of water required to form the ice exceeded the amount of the water in the aqueous solution. With increase in the mass fraction of the TBPOx in this aqueous solution, more water may be needed to form hydrate with all of the excess TBPOx present in solution. Due to the lack of water compared to the required stoichiometry, hydrate formation decreased. This would explain the decreasing peak depth of hydrate dissociation heats shown in **Figure 6** at the mass fractions from 0.36 to 0.39.

As shown in **Figure 6** at the mass fraction 0.40, the heat flow obtained by the heating rate of 2°C min^{-1} crossed the baseline. The two kinds of hydrate dissociation peaks were not separated at this heating rate. For a more accurate measurement, the dissociation measurement was performed with the heating rate of 0.5°C min^{-1} only at the mass fraction 0.40. In **Figure 7**, as well as the previous heat flow, two endothermic peaks of hydrate dissociation and one exothermic peak were obtained. Compared to the heat flow at 2°C min^{-1} heating rate, the exothermic peak at a temperature of around 5°C was obviously confirmed. The exothermic peak appeared just after the small endothermic peak. The endothermic peaks would emerge due to the hydrate formation. Although the heating rate was slower, two kinds of hydrate dissociation peaks were still not separated. The reaction of small endothermic, exothermic, and large endothermic processes continuously occurred. The small endothermic peak emerged because of the dissociation of the lower equilibrium temperature hydrate, and the large endothermic peak was due to the hydrate dissociated around 10°C. At the temperature around 5°C, the hydrate of the lower equilibrium temperature was dissociated into aqueous solution, and another type of hydrate of equilibrium temperature around 10°C also started to dissociate. On the endothermic dissociation process of the higher equilibrium temperature hydrate, the aqueous solution from the lower equilibrium temperature hydrate would be cooled. The dissociation of the higher equilibrium temperature hydrate and the recrystallization of the lower equilibrium temperature hydrate would occur simultaneously.

The dissociation heats, corresponding to the peaks in the DSC spectra near 10°C measured in this study, are shown in **Table 3**, where ΔH_d indicates the dissociation heats (enthalpies). The dissociation heats increased with the mass fraction at the mass fraction range below 0.35. In the present measurements, no ice melting peak appeared at a mass fraction of 0.30. The dissociation heat was obtained from the heat flow without the ice melting peak. At the mass fraction 0.35, the largest dissociation heat, 186.0 ± 0.5 kJ·kg^{-1}, was obtained. At the mass fraction range from 0.35 to 0.37, the dissociation heats gradually decreased and then increased with the mass fraction at that range from 0.38 to 0.39. Over the mass fraction range 0.39, the dissociation heats decreased. The values of the hydrate dissociation heat resulted from the amount of hydrates formed in the test cell. The largest amount of hydrates was considered to be formed at the mass fraction 0.35.

TABLE 3 | The dissociation heats of TBPOx hydrate from differential scanning calorimetry measurements.

w_{TBPOx} [a]	x_{TBPOx} [b]	ΔH_d (kJ·kg^{-1})	U [c] (ΔH_d) (kJ·kg^{-1})
0.20	0.0074	77.8	±1.5
0.30	0.0126	145.1	±2.2
0.34	0.0151	180.9	±1.0
0.35	0.0157	186.0	±0.5
0.36	0.0164	178.3	±0.7
0.37	0.0171	179.4	±2.7
0.38	0.0180	181.8	±3.5
0.39	0.0186	181.7	±3.5
0.40	0.0194	176.0	±3.7

[a] *The standard uncertainty u (w_{TBPOx}) is ± 5.0 × 10^{-3}.*
[b] *The standard uncertainty u (w_{TBPOx}) is ± 4.0 × 10^{-3}. These values of mole fractions were obtained by converting the mass fractions.*
[c] *The expanded uncertainty U (ΔH_d) (kJ·kg^{-1}) was obtained by the triplicate measurements (k = 2).*

The measurement data of the phase equilibrium temperatures and the dissociation heats are summarized in **Figure 8**. In the phase equilibrium measurement, as well as the tendency of the dissociation heat, measured values of the thermophysical properties initially increased with the mass fraction. Over the mass fraction range from 0.35 to 0.39, the phase equilibrium temperature and dissociation heat tended to decrease. Those plots, respectively showed parabolic shapes, which was similarly confirmed in the previous studies (Yamauchi et al., 2017a,b; Arai et al., 2018, 2019; Shimada et al., 2018, 2019; Koyama et al., 2019).

The maximum points in the plots of phase equilibrium temperature and dissociation heat indicate that the congruent point of TBPOx semiclathrate hydrate would exist at the mass fraction range from 0.34 to 0.36.

Evaluation as Thermal Energy Storage Medium

The measurements showed that the highest phase equilibrium temperature of TBPOx was 9.4°C and the largest dissociation heat was 186.0 ± 0.5 kJ·kg^{-1}. To evaluate thermophysical property as a thermal energy storage medium, TBPOx could be compared with other PCMs, organic compounds, water, metallic

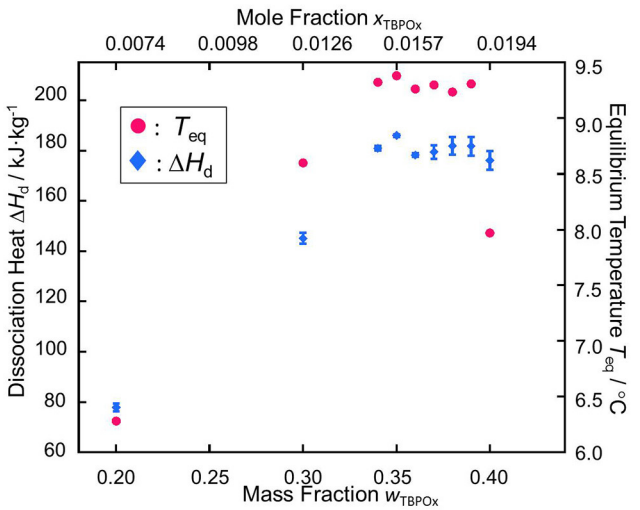

FIGURE 8 | Relationships between the equilibrium temperature T_{eq} and the dissociation heat ΔH_d vs. the mass fraction of TBPOx aqueous solution w_{TBPOx} and the mole fraction of TBPOx aqueous solution x_{TBPOx}: red ●, the phase equilibrium temperature of TBPOx hydrate; blue ♦, the dissociation heat of TBPOx hydrate.

TABLE 4 | The equilibrium temperatures and dissociation heats of PCMs available as cold energy.

Compound	T_{eq} (°C)	ΔH_d (kJ·kg^{-1})	References
Paraffin (C15–16)	8.0	153[a]	Lorsch et al., 1975; Mehling and Cabeza, 2007
$LiClO_3 \cdot 3H_2O$	8.1	155[a]	Naumann and Emons, 1989; Veerakumar and Sreekumar, 2015
Water	0	333	Feistel and Wagner, 2006
Tetrabutylammonium bromide (TBAB) hydrate [b]	12.7	193	Oyama et al., 2005; Kobori et al., 2015
Tetrabutylammonium chloride (TBAC) hydrate [b]	15.0	201	Castellani et al., 2014
Tetrabutylammonium butylate (TBABu) hydrate	15.4	185	Yamauchi et al., 2017b
Tetrabutylammonium propionate (TBAP) hydrate	17.5	203	Yamauchi et al., 2017a
Tetrabutylphosphonium bromide (TBPB) hydrate [b]	9.2	214	Suginaka et al., 2012
Tetrabutylphosphonium holoride (TBPC) hydrate [b]	10.3	194	Sakamoto et al., 2011
Tetrabutylphosphonium propionate (TBPBu) hydrate	13.9	204	Shimada et al., 2019
Tetrabutylphosphonium propionate (TBPP) hydrate	15.6	190	Shimada et al., 2019
Tetrabutylphosphonium oxalate (TBPOx) hydrate	9.4	186	-

[a] *The value of the latent heat.*
[b] *The hydrate contains halide anions.*

salt hydrates, and other semiclathrate hydrates. **Table 4** shows the latent heat of substances that could be utilized as cold energy.

The PCMs, paraffin (C15–16), and $LiClO_3 \cdot 3H_2O$ respectively represent organic compounds and metal salt hydrates, which have phase equilibrium temperature similar to that of TBPOx hydrate (Lorsch et al., 1975; Naumann and Emons, 1989; Mehling and Cabeza, 2007; Veerakumar and Sreekumar, 2015). In this temperature range, the latent heat of water is not available. The required energy 42.2 kJ·kg^{-1} was calculated by multiplying the specific heat of water 4.22 kJ kg^{-1}·K^{-1} (IAPWS, 2008) with the temperature difference 10 K. As well as water, TBPOx hydrate also has the sensible heat. Adding the sensible heat to the dissociation heat, total energy density of TBPOx hydrate would be over 186.0 kJ·kg^{-1}. This could help reduce the size and the mass of the practical device.

The energy density of TBPOx hydrate is approximately four times larger than that of water. Compared with other PCMs with close phase equilibrium temperature, TBPOx hydrate has the equivalent energy density. Furthermore, it has no flammability and corrosiveness unlike organic compounds and metal salt hydrates. While well-known semiclathrate hydrates, TBAB hydrate and tetrabutylammonium choloride (TBAC) hydrate, have large latent heat, they contain halide anions (Oyama et al., 2005; Sato et al., 2013). TBPOx hydrate includes carboxylic acid anions in the guest compounds. Compared to these compounds, TBPOx hydrate is environmentally friendly. With this safety and benign environmental aspect, TBPOx hydrate is suitable for the thermal energy storage media in air conditioning systems. Compared to hydrates incorporating carboxylic anions, TBPOx hydrate has a different equilibrium temperature from tetrabutylammonium butylate (TBABu) hydrate, tetrabutylammonium propionate (TBAP) hydrate, tetrabutylphosphonium butylate (TBPBu) hydrate, and tetrabutylphosphonium propionate (TBPP) hydrate. Although the value of the latent heat is slightly lower than them, TBPOx could extend the temperature range for the application.

CONCLUSION

In this study, thermophysical properties of TBPOx hydrate were measured. The highest phase equilibrium temperature was 9.4°C at the mass fraction 0.35 in aqueous solution. The largest dissociation heat was 186.0 ± 0.5 kJ·kg^{-1} at the mass fraction 0.35. Incorporating carboxylic acid anions as parts of the guest compounds, it has a more environmentally friendly composition than halide-based alternatives. As a PCM, the energy density of TBPOx hydrate is equal to or greater than other substances having close phase equilibrium temperature. Moreover, having no flammability and corrosiveness unlike organic compounds and salt metal hydrates, it is useful in the aspect of safety and sustainability. TBPOx hydrate would be suitable as a thermal energy storage media for the use of air conditioning system.

DATA AVAILABILITY STATEMENT

All datasets presented in this study are included in the article/supplementary files.

AUTHOR CONTRIBUTIONS

The experiment design and manuscript preparation were done by TM with RO. NK and AH assisted with the experiments in DSC measurement. SA and RO assisted in experiment design, data analysis, and the preparation of manuscript. All authors contributed to the article and approved the submitted version.

FUNDING

This study was supported by JKA Foundation (Grant No. 2018M-170) and JSPS KAKENHI (Grant No. 17H03122).

ACKNOWLEDGMENTS

The authors gratefully acknowledge the Ohmura Lab members for valuable discussion and support.

REFERENCES

Alavi, S., and Ohmura, R. (2016). Understanding decomposition and encapsulation energies of structure I and II clathrate hydrates. *J. Chem. Phys.* 145:154708. doi: 10.1063/1.4964673

Arai, Y., Koyama, R., Endo, F., Hotta, A., and Ohmura, R. (2019). Thermophysical property measurements on tetrabutylphosphonium sulfate ionic semiclathrate hydrate consisting of the bivalent anion. *J. Chem. Thermodyn.* 131, 330–335. doi: 10.1016/j.jct.2018.11.017

Arai, Y., Yamauchi, Y., Tokutomi, H., Endo, F., Hotta, A., Alavi, S., et al. (2018). Thermophysical property measurements of tetrabutylphosphonium acetate (TBPAce) ionic semiclathrate hydrate as thermal energy storage medium for general air conditioning systems. *Int. J. Refrig.* 88, 102–107. doi: 10.1016/j.ijrefrig.2017.12.020

ASRAE (2016). *Technical Committee TC*, 9.9 *Data Center Power Equipment Thermal Guidelines and Best Practices*. Available online at: http://www.ashrae.org (accessed March 18, 2020).

Castellani, B., Morini, E., Fillipponi, M., Nicolini, A., Palombo, M., et al. (2014). Clathrate hydrates for thermal energy storage in buildings: overview of proper hydrate-forming compounds. *Sustainability*. 6, 6815–6829. doi: 10.3390/su6106815

Darbouret, M., Cournil, M., and Herri, J. (2005). Rheological study of TBAB hydrate slurries as secondary two phase refrigerants. *Int. J. Refrig.* 28, 663–671. doi: 10.1016/j.ijrefrig.2005.01.002

Dyadin, Y., Terekhova, I., Polyanskaya, T., and Aladko, L. (1976). Clathrate hydrates of tetrabutylammonium fluoride and oxalate. *J. Struct. Chem.* 17, 566–571. doi: 10.1007/BF00753438

Feistel, R., and Wagner, W. (2006). A new equation of state for H2O Ice Ih. *J. Phys. Chem. Ref Data*. 35, 1021–1047. doi: 10.1063/1.2183324

IAPWS (2008). *International association for the Properties of Water and Steam Release on the IAPWS Formulation 2008 for the Thermodynamic Properties of Seawater*. Available online at: http://www.iapws.org (accessed March 18, 2020).

International Energy Agency IEA and World Energy Outlook (2019). Available online at: http://www.iea.org (accessed March 18, 2020)

Kobori, T., Muromachi, S., Yamasaki, T., Takeya, S., Yamamoto, Y., Alavi, S., et al. (2015). Phase behavior and structural characterization of ionic clathrate hydrate formed with tetra-n-butylphosphonium hydroxide: discovery of primitive crystal structure. *Cryst. Growth Des.* 15, 3862–3867. doi: 10.1021/acs.cgd.5b00484

Koyama, R., Arai, Y., Yamauchi, Y., Takeya, S., Endo, F., Hotta, A., et al. (2019). Thermophysical properties of trimethylolethane (TME) hydrate as phase change material for cooling lithium-ion battery in electric vehicle. *J. Power Sources* 427, 70–76. doi: 10.1016/j.jpowsour.2019.04.055

Li, G., Hwang, Y., and Radermacher, R. (2012). Review of cold storage materials for air conditioning application. *Int. J. Refrig.* 35, 2053–2077. doi: 10.1016/j.ijrefrig.2012.06.003

Lorsch, H., Kauffman, K., and Denton, J. (1975). Thermal energy storage for solar heating and off-peak air conditioning. *Energy Convers.* 15, 1–8. doi: 10.1016/0013-7480(75)90002-9

Mayoufi, N., Dalmazzone, D., Delahaye, A., Clain, P., Fournaison, L., et al. (2011). Experimental data on phase behavior of simple tetrabutylphosphonium bromide(TBPB) and mixed CO2 + TBPB semiclathrate hydrates. *J. Chem. Eng. Data*. 56, 2987–2993. doi: 10.1021/je2003918

Mehling, H., and Cabeza, F. (2007). "Phase change materials and their basic properties," in *Thermal Energy Storage for Sustainable Energy Consumption. NATO Science Series (Mathematics, Physics and Chemistry)*, ed O. Paksoy (Dordrecht: Springer), 257–278. doi: 10.1007/978-1-4020-5290-3_17

Mehling, H., and Cabeza, F. (2008). *Heat and Cold Storage With PCM An Up to Date Introduction into Basics and Applications*. Berlin; Heidelberg: Springer. doi: 10.1007/978-3-540-68557-9

Nakayama, H., Asano, M., Nakajima, Y., and Hanno, K. (1983). Selective separation of anions through the formation of clathrate hydrates of quaternary ammonium salts. *Bull. Chem. Soc. Jpn*. 2, 269–272.

Nakayama, H., and Hashimoto, M. (1980). Hydrate of organic compounds. V. the clathrate hydration of alcohols. *Bull. Chem. Soc. Jpn.* 53, 2427–2433. doi: 10.1246/bcsj.53.2427

Nakayama, H., and Torigata,S. (1984). Hydrates of organic compounds. VIII. the effect of carboxylate anions on the formation of clathrate hydrates of tertabutylammonium carboxylates. *Bull. Chem. Soc. Jpn*. 57, 171–174. doi: 10.1246/bcsj.57.171

Naumann, R., and Emons, H. (1989). Results of thermal analysis for investigation of salt hydrates as latent heat-storage materials. *J. Therm. Anal.* 35, 1009–1031. doi: 10.1007/BF02057256

Oshima, M., Kida, M., and Nagao, J. (2018). Hydration numbers and thermal properties of tetra-n-butyl ammonium bromide semiclathrate hydrates determined by ion chromatography and differential scanning calorimetry. *J. Chem. Thermodyn.* 123, 32–37. doi: 10.1016/j.jct.2018.03.018

Oyama, H., Shimada, W., Ebinuma, T., Kamata, Y., Takeya, S., Uchida, T., et al. (2005). Phase diagram, latent heat, and specific heat of TBAB semiclathrate hydrate crystals. *Fluid Phase Equilib.* 234, 131–135. doi: 10.1016/j.fluid.2005.06.005

Pelay, U., Luo, L., Fan, Y., Stitou, D., and Rood, M. (2017). Thermal energy storage systems for concentrated solar power plants. *Renew. Sust. Energ. Rev.* 79, 82–100. doi: 10.1016/j.rser.2017.03.139

Pielichowska, K., and Pielichowski, K. (2014). Phase change materials for thermal energy storage. *Prog. Mater. Sci.* 65, 67–123. doi: 10.1016/j.pmatsci.2014.03.005

Sakamoto, H., Sato, K., Shiraiwa, K., Takeya, S., Nakajima, M., and Ohmura, R. (2011). Synthesis, characterization and thermal-property measurement of ionic semi-clathrate hydrates formed with tertrabutylphosphonium chloride and tetrabutylammonium acrylate. *RSC Adv.* 1, 315–322. doi: 10.1039/c1ra00108f

Sato,K., and Tokutomi, H., Ohmura, R. (2013). Phase equilibrium of ionic semiclathrate hydrates formed with tetrabutylammonium bromide and tetrabutylammonium chloride. *Fluid Phase Equilib.* 337, 115–118. doi: 10.1016/j.fluid.2012.09.016

Shimada, J., Shimada, M., Sugahara, T., and Tsunashima, K. (2019). Phase equilibrium relations of tetra-n-butylphosphonium propionate and butyrate semiclathrate hydrates. *Fluid Phase Equilib.* 485, 61–66. doi: 10.1016/j.fluid.2018.11.038

Shimada, J., Shimada, M., Sugahara, T., Tsunashima, K., Tani, A., Tsuchida, Y., et al. (2018). Phase equilibrium relations of semiclathrate hydrates based on tetra- n-butylphosphonium formate, acetate, and lactate. *J. Chem. Eng. Data.* 63, 3615–3620. doi: 10.1021/acs.jced.8b00481

Suginaka, T., Sakamoto, I. K., Takeya, S., and Nakajima, M., Ohmura, R. (2012). Thermodynamic properties of ionic semiclathrate hydrate formed with tetrabutylphosphonium bromide, *Fluid Phase Equilib.* 317, 25–28. doi: 10.1016/j.fluid.2011.12.010

Veerakumar, C., and Sreekumar, A. (2015). Phase change material based cold thermal energy storage: materials, techniques and applications - a review. *Int. J. Refrig.* 67, 271–289. doi: 10.1016/j.ijrefrig.2015.12.005

Wang, X., and Dennis, M. (2015). An experimental study on the formation behavior of single and binary hydrates of TBAB, TBAF and TBPB for cold storage air conditioning applications. *Chem. Eng. Sci.* 137, 938–946. doi: 10.1016/j.ces.2015.07.042

Yamauchi, Y., Arai, Y., Yamasaki, T., Endo, F., Hotta, A., and Ohmura, R. (2017a). Phase equilibrium temperature and dissociation heat of ionic semiclathrate hydrate formed with tetrabutylammonium butyrate. *Fluid Phase Equilib.* 441, 54–58. doi: 10.1016/j.fluid.2017.02.001

Yamauchi, Y., Yamasaki, T., Endo, F., Hotta, A., and Ohmura, R. (2017b). Thermodynamic properties of ionic semiclathrate hydrate formed with tetrabutylammonium propionate. *Chem. Eng. Technol.* 40, 1810–1816. doi: 10.1002/ceat.201600459

Zalba, B., Marín, J., Cabeza, L., and Mehling, H. (2003). Review on thermal energy storage with phase change: materials, heat transfer analysis and applications. *App. Therm. Eng.* 23, 251–283. doi: 10.1016/S1359-4311(02)00192-8

Conflict of Interest: The authors declare that the research was conducted in the absence of any commercial or financial relationships that could be construed as a potential conflict of interest.

frontiers in Chemistry

ORIGINAL RESEARCH
published: 17 July 2020
doi: 10.3389/fchem.2020.00614

Oxabicyclic Guest Compounds as sII Promoters: Spectroscopic Investigation and Equilibrium Measurements

Jiwoong Seol[1]*, *Woongchul Shin*[2] and *Juwoon Park*[3]

[1] Faculty of Liberal Education, Seoul National University, Seoul, South Korea, [2] Central Technology R&D Institute, Hyundai Oilbank Co., Ltd., Yongin-si, South Korea, [3] Naval & Energy System R&D Institute, Daewoo Shipbuilding & Marine Engineering Co., Ltd., Siheung-si, South Korea

In this study, we investigate three oxabicyclic compounds, 3,6-dioxabicyclo[3.1.0]hexane ($C_4H_6O_2$, ETHF), 7-oxabicyclo[2.2.1]heptane ($C_6H_{10}O$, 14ECH), and 7-oxabicyclo[4.1.0]heptane ($C_6H_{10}O$, 12ECH) as novel promoters for gas hydrates. According to the outcomes of powder X-ray diffraction (PXRD) and synchrotron high-resolution powder diffraction (HRPD), all CH_4 hydrates formed with ETHF, 14ECH, and 12ECH were identified to be sII (Fd-3m) hydrates with corresponding lattice parameters of 17.195, 17.330, and 17.382 Å, respectively. It was also clearly demonstrated that CH_4 molecules are accommodated in the sII-S cages through solid-state ^{13}C NMR and Raman spectra. Consequently, we clarified that the three compounds observed are large guest molecules (LGMs) that occupy the sII-L cages. Moreover, the thermodynamic stability of each LGM + CH_4 (and N_2) hydrate system was remarkably improved compared to that of the simple CH_4 (and N_2) hydrate. In particular, 14ECH manifested several unique features compared to the other two promoters. First, the 14ECH + CH_4 hydrate did not dissociate up to room temperature (298 K), even at a moderate pressure of approximately 60 bar. At a given pressure, 14ECH increased the dissociation temperature of the CH_4 hydrate by ~18 K, indicating that its promotion capability is as strong as that of tetrahydrofuran (THF), currently considered to be the most powerful promoter. Second, more interestingly, it was revealed by further PXRD, NMR, and Raman analyses that 14ECH forms a simple sII hydrate in the absence of help gases. According to differential scanning calorimetry (DSC) outcomes, we revealed that the simple 14ECH hydrate dissociates at 270~278 K under ambient pressure. In addition to the thermodynamic stability, we also note that the 14ECH + CH_4 hydrate presented a sufficiently high temperature of formation, requiring little additional cooling. Given these promising features, we expect that the 14ECH hydrate system can be adopted to realize hydrate-based technologies. We also believe that the LGMs introduced here have considerable potential to serve as alternates to conventional promoters and that they can be widely utilized in both engineering and scientific research fields.

Keywords: sII promoter, oxabicyclic compounds, 1,4-epoxycyclohexane, simple hydrate former, powder diffraction, NMR, Raman, gas storage

OPEN ACCESS

Edited by:
Fei Wang,
Qingdao University of Science and Technology, China

Reviewed by:
Lipeng Xin,
Xi'an Jiaotong University, China
Carmelo Corsaro,
University of Messina, Italy

***Correspondence:**
Jiwoong Seol
seoljiwoong@snu.ac.kr

Specialty section:
This article was submitted to Physical Chemistry and Chemical Physics, a section of the journal Frontiers in Chemistry

Received: *10 April 2020*
Accepted: *11 June 2020*
Published: *17 July 2020*

Citation:
Seol J, Shin W and Park J (2020) Oxabicyclic Guest Compounds as sII Promoters: Spectroscopic Investigation and Equilibrium Measurements. Front. Chem. 8:614. doi: 10.3389/fchem.2020.00614

INTRODUCTION

Clathrate hydrate, consisting of a hydrogen-bonded water framework and guest molecules, is now a well-known type of inclusion compound. Because general types of clathrate hydrates are mainly composed of water, various potential for sustainable hydrate-based technologies have long been suggested, including CH_4/H_2/natural gas storage (Florusse et al., 2004; Seo et al., 2009; Veluswamy et al., 2016), CO_2 capture and storage (Park et al., 2006; Shin et al., 2008), gas separation (Seo et al., 2005; Babu et al., 2015), desalination (Cai et al., 2016), air-conditioning (Nakajima et al., 2008), and their use of functional materials (Yeon et al., 2008; Park et al., 2009; Shin et al., 2009; Seol et al., 2012). Meanwhile, versatile compounds have also been extensively investigated as co-guest additives. Such additional guest molecules are referred to as large guest molecules (LGMs) or large molecule guest substances (LMGSs) given their larger sizes compared to other gaseous guest compounds. An important purpose of employing LGMs, especially given the engineering and industrial applications of hydrates, is to promote the conditions for gas hydrate formation and preservation so as to minimize the total amount of energy consumed when utilizing hydrates. In most cases, though the thermodynamic stability levels are enhanced by incorporating promoters, the structure of the original CH_4 hydrate (sI) is necessarily transformed to sII or sH, leading to reduced storage capacities by least 15∼20%. However, many researchers have focused more on the thermodynamic stability, which is improved significantly, especially when adding sII promoters.

In terms of the guest distribution, most sII gas hydrates containing LGMs are classified as "double" hydrates, because the large (sII-L) and small (sII-S) cages are primarily occupied by LGMs and gaseous components, respectively. On the other hand, gas-free sII hydrates stabilized by a LGM component alone should be classified as a "simple" hydrate, and we simply refer to these LGMs as "simple sII formers" or "simple formers" in this paper. In general, gas hydrates bearing simple sII formers exhibit considerably higher thermodynamic stability levels compared to those formed with ordinary LGMs. For example, under pressure of approximately 40 bar, the dissociation temperature of furan + CH_4 (∼295 K, Pahlavanzadeh et al., 2016) or tetrahydrofuran (THF) + CH_4 (∼297 K, Lee et al., 2012) is considerably higher than that of the pyrrolidine + CH_4 hydrate (∼287 K, Shin et al., 2012). As an another example, at nearly 80 bar, the stable region of the 1,3-dioxane + CH_4 hydrate (∼297 K, Li et al., 2020) is much larger than that of the cyclohexane (CH) + CH4 (∼290 K, Sun et al., 2002) hydrate. Moreover, simple hydrates of LGMs are expected to have a variety of applications, as they do not require pressurized gases and have good flexibility (i.e., tuning) of the guest compositions (Nakajima et al., 2008; Park et al., 2009; Seo et al., 2009; Shin et al., 2012). However, although numerous LGMs have been proposed over nearly a century, only a few of them have been found to be simple sII formers, apart from halogenated organics such as chlorofluorocarbons (CFCs). To the best of our knowledge, no new simple sII former has been discovered since Udachin et al. (2002) reported the structure of the simple hydrate of tetrahydropyran (THP) through single crystal diffraction.

It is very interesting that many the simple sII formers are empirically oxacyclic hydrocarbons such as propylene oxide, trimethylene oxide, 1,3-dioxolane, furan, THF, 1,3-dioxane, and tetrahydropyran (THP). In view of this, in this study, we investigate the three oxabicyclic compounds of 3,6-dioxabicyclo[3.1.0]hexane ($C_4H_6O_2$), 7-oxabicyclo[2.2.1]heptane ($C_6H_{10}O$), and 7-oxabicyclo[4.1.0]heptane ($C_6H_{10}O$) as novel formers of sII gas hydrates. Instead of the IUPAC names, we will use corresponding synonyms of epoxytetrahydrofuran (ETHF), 1,4-epoxycyclohexane (14ECH) and 1,2-epoxycyclohexane (12ECH) for simplicity and unity in this paper. The rest of this paper describes the following step-by-step research. First, the crystal structure of each LGM + CH_4 hydrate was determined by crystallographic analyses. Second, the distribution of the guest compounds was monitored through solid-state ^{13}C NMR and Raman spectrometry. Third, the equilibrium P-T conditions of the LGM + CH_4 (and N_2) hydrate systems were measured to estimate the promotion performances. Fourth, further PXRD, NMR, Raman and DSC assessments were conducted and the results analyzed in detail to determine whether the promoters act as simple sII formers. Finally, the unique features of the 14ECH hydrate system focusing on the formation conditions were discussed.

EXPERIMENTAL

H_2O (LC-MS grade, Merck), ETHF (97%, Tokyo Chemical Industry), 14ECP (98%, Alfa Aesar), and 12ECH (98%, Tokyo Chemical Industry) and were used as received. High-purity CH_4 (99.95%) and N_2 (99.99%) were supplied by Daesung Industrial Gas Corp. of Korea. Compared to the stoichiometric composition ($x_{LGM} = 0.0556$) for the sII hydrate, approximately 5% excessive amount of each LGM was mixed with water and charged in a high-pressure resistance cell (V∼100 ml). Then CH_4 was supplied into the vessel until the initial pressure was reached 60∼65 bar at ambient temperature (80∼90 bar of N_2 were supplied for N_2 hydrate samples). The cell in each case was gradually cooled at the rate of -1 K•h^{-1} with stirring maintained at 200 ± 10 RPM. The temperatures at which the pressure starts to drop varied significantly depending on the type of the LGMs used. However, we cooled the vessel to a sufficiently low temperature of approximately 260 K to obtain a sample in a fully solidified state. The vessel was then quenched by liquid nitrogen and the solid sample was quickly collected. Finally, for the subsequent spectroscopic analyses, it was ground into a fine powder ($d < 200\,\mu m$) inside liquid nitrogen.

To identify the crystal structures, we first utilized synchrotron high-resolution powder diffraction (HRPD) and powder X-ray diffraction (PXRD). For ETHF and 12ECH hydrates, the HRPD patterns were obtained with a single wavelength of 1.5216 Å, recording in a 2θ range of 5.0–126.0° (step width = 0.01° and scan time = 0.7 s/scan). For 14ECH and CH hydrates, the PXRD patterns were obtained with a Rigaku D/MAX-2500

equipment using a light source of Cu radiation with a wavelength of 1.54180 Å ($K\alpha_1$ = 1.54056 Å and $K\alpha_2$ = 1.54439 Å) and with a power of 8 kW (40 kV and 200 mA), recording in a 2θ range of 5.0–55.0° (step width = 0.02° and scan time = 1 s/scan). Every measurement temperature was kept at 150 K and no dissociation of the samples was detected. The crystal structures and corresponding lattice parameters were determined using FullProf and Checkcell programs.

Next, both solid-state NMR and Raman experiments were carried out to monitor the molecular behaviors of the guest components. Solid-state ^{13}C NMR (HPDEC) experiments were conducted with the Bruker 400 MHz Avance II solid-state NMR at the Korea Basic Science Institute. We used a Larmor frequency of 100.4 MHz, a pulse length (p1) of 1.6 μs, and a repetition delay time (d1) of 3 s. The static signal of tetramethylsilane was referred to as 0 ppm at room temperature. All samples were measured at 210 K with a magic-angle spinning rate of 5 kHz. The vibration frequencies of the guest molecules were studied with high-resolution Raman equipment (Horiba Jobin Yvon LabRam HR Evolution). A 532-nm laser at 50 mW was used as an excitation source. All Raman spectra were obtained at 123 K with a low-temperature Linkam accessory.

To investigate the thermal properties of hydrates, temperature-dependent phase patterns were measured with differential scanning calorimeter (DSC) equipment (NETZSCH DSC 200 F3 Maia). A small piece of each sample (approximately 3∼5 mg) was placed in aluminum pan, immersed in liquid nitrogen. The pan was then mounted on the sample stage that was precooled at 173 K. After the 10 min of isothermal time at 173 K and ambient pressure, the sample was slowly heated at a constant rate of 3 K/min to reach 298 K. During the overall measurement period, the sample stage was purged by nitrogen gas to prevent the humidity.

We also measured the equilibrium P-T conditions of the CH_4 (or N_2) hydrate systems containing the three LGMs. Each liquid mixture (total mass ∼7 g) consists of a stoichiometric composition of LGM and balanced water was charged into a high-pressure resistance cell (V ∼ 100 ml) and pressurized at various CH_4 or N_2 pressures at ambient temperature. The samples were continuously cooled to 260 K (at a rate of −1 K•h^{-1}) to form a solid hydrate phase. They were then more slowly heated to 310 K (at a rate of 0.3 K•h^{-1}). The stirring speed was kept at 200 ± 10 RPM during the overall hysteresis process. To verify the accuracy of our measurements, several equilibrium points of the simple CH_4 and THF + CH_4 hydrates were additionally measured. We note that our measurements demonstrated very good agreement with the reported values (Adisasmito et al., 1991; Lee et al., 2012).

RESULTS AND DISCUSSION

The geometries and center-to-center distances of five molecules, ETHF, 14ECH, 12ECH, THF, and CH, are illustrated in **Figure 1**. The molecular geometries were optimized via B3LYP calculations with the basis set of 6-31G++ (d, p) using Gaussian 03 program (Frisch et al., 2004). The size of THF was in good agreement with the reported value (Takeya et al., 2018). There are two types of COC bonds: those in the epoxide rings and those in the five-membered rings. In the epoxide rings, both ETHF and 12ECH

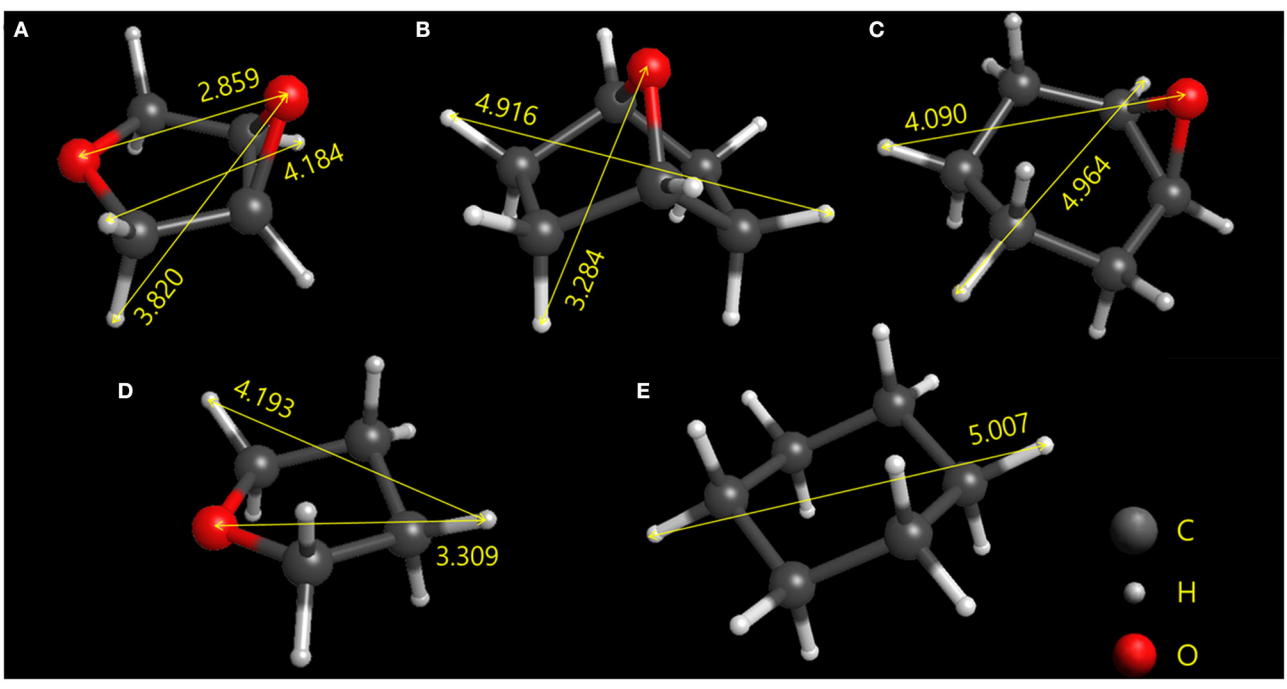

FIGURE 1 | Optimized geometries of the **(A)** ETHF, **(B)** 14ECH, **(C)** 12ECH, **(D)** THF, and **(E)** CH. The longest center-to-center distances between each type of atom are given in angstroms.

show similar CO bond lengths of 1.44 Å and COC bond angles of 61.5°. However, the five-membered rings of ETHF and 14ECH showed somewhat different geometries. The CO bond length and COC bond angle of ETHF were 1.43 Å and 110°, respectively, nearly identical to those of THF. However, the COC bond angle of 14ECH was found to be 96.6°, leading to a somewhat smaller CC distance of 2.16 Å compared to that of ETHF (2.35 Å). Consequently, the six-membered ring of 14ECH is more distorted and slightly smaller than that of 12ECH. Considering that the sizes of ETHF, 14ECH, and 12ECH are similar to those of THF and CH, one can expect that the three LGMs will form sII hydrates.

Figure 2 and **Table 1** shows the powder diffraction patterns and corresponding Miller indices of the CH_4 hydrates formed with ETHF, 14ECH, and 12ECH. The structures of the ETHF, 14ECH, and 12ECH + CH_4 hydrates were clearly identified to be the sII (Fd-3m) type with lattice parameters of 17.195, 17.330, and 17.382 Å, respectively. These lattice parameters correspond to unit-cell volumes of 5083.8, 5204.7, and 5251.89 $Å^3$. The amount of hexagonal ice (Ih) or CH_4 hydrate (sI) due to the exclusion of LGMs was minute or negligible. We also measured the powder diffraction pattern of the CH + CH_4 hydrate and obtained a lattice parameter of a = 17.480 Å (**Figure S1** and **Table S1**). The lattice parameter of the THF + CH_4 hydrate was previously reported as a = 17.224 Å (Lee et al., 2012). Thus, the unit cell sizes are in the following order: ETHF < THF < 14ECH < 12ECH < CH + CH_4 hydrates. Accordingly, we can conclude that the effective van der Waals volume of the >CH–O–CH< group is slightly smaller than that of the -CH_2-CH_2- group.

Solid-state ^{13}C NMR and Raman spectroscopy were utilized in order to cross-check the structures and monitor the CH_4 guest molecules. As shown in **Figure 3A**, a single clear peak at $\delta = -4.5 \sim -4.8$ ppm was detected for every CH_4 hydrate, corresponding to the CH_4 molecule entrapped in the small (5^{12}) cage. No other peaks were detected for the ETHF and 14ECH + CH_4 hydrates in the upfield region. Although additional signals at −4.3, −6.7, and −8.3 ppm, typical of CH_4 molecules entrapped in sI-S, sI-L, and sII-L cages (Yeon et al., 2006), respectively, were observed for the 12ECH + CH_4 hydrate, these peaks are quite small compared with the main peak near −4.8 ppm. The Raman spectra in **Figure 3B** allow the same interpretation; C-H stretching vibration bands near 2,911 cm^{-1} were clearly observed for all samples, indicative of a CH_4 molecule in a small cage, whereas only a weak signal near 2,902 cm^{-1} (sI-L or sII-L) was additionally detected for the ECH + CH_4 hydrate. To summarize the outcomes of the HRPD, ^{13}C NMR, and Raman investigations, all LGMs can readily form "double" sII hydrates with CH_4, of which the large and small cages are mainly occupied by LGM and CH_4 molecules, respectively. Moreover, the ^{13}C NMR peaks found at −4.47 (ETHF), −4.72 (ECH), and −4.80 ppm (ECH) clearly indicated that even when the type of the enclosing cage is identical (sII-S), the CH_4 molecule in the larger cage exhibits a more shielded chemical shift. It is not a great difference; however, the propensity is clear enough such that one can roughly estimate which hydrate has a larger lattice parameter by comparing the NMR peaks without precise crystallographic analyses.

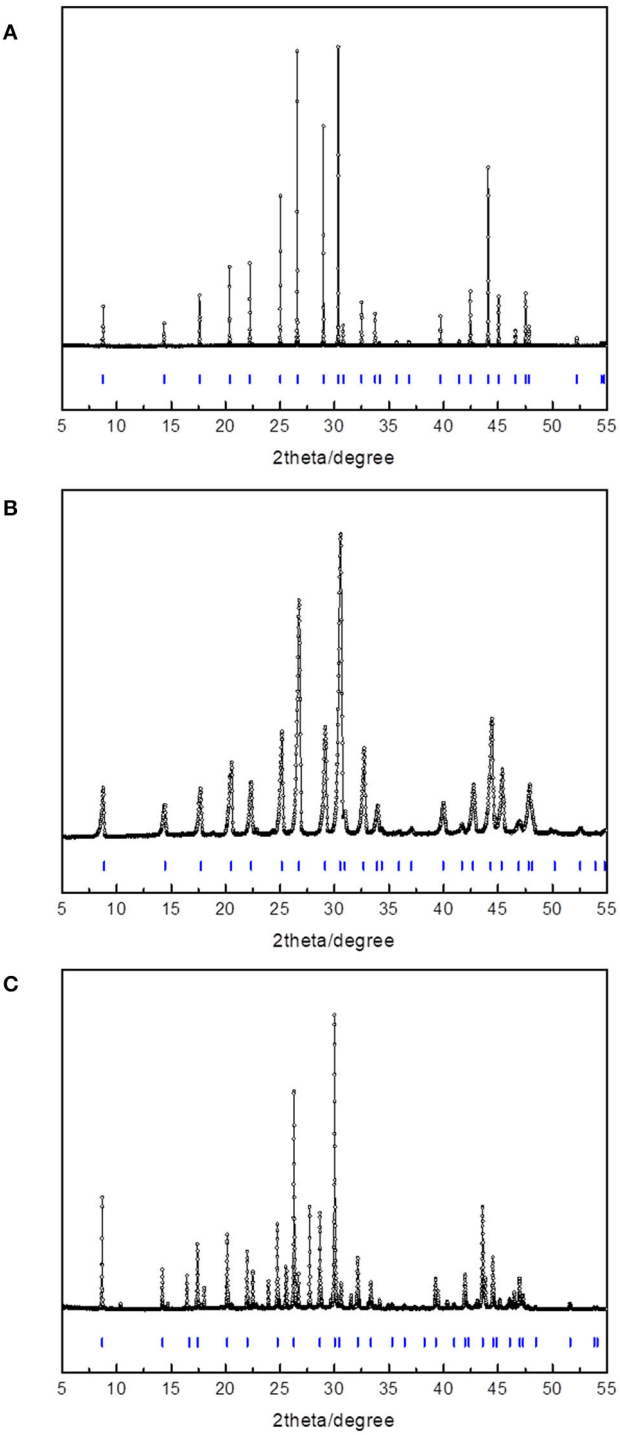

FIGURE 2 | HRPD and PXRD patterns of the **(A)** ETHF, **(B)** 14ECH, and **(C)** 12ECH + CH_4 hydrates.

Next, we measured the equilibrium P-T conditions of the three CH_4 hydrate systems at a constant mole fraction of the liquid phase ($x_{LGM} = 0.0556$) and listed the results in **Table 2**. By incorporating each LGM, the thermodynamic region of the

TABLE 1 | Miller indices of the three hydrates shown in **Figure 2**.

ETHF + CH_4			14ECH + CH_4			12ECH + CH_4		
Peaks	***hkl***	d_{hkl}	**Peaks**	***hkl***	d_{hkl}	**Peaks**	***hkl***	d_{hkl}
8.79	111	9.928	8.84	111	10.006	8.696	111	10.0355
14.38	202	6.079	14.46	202	6.127	14.223	202	6.1455
17.63	222	4.964	16.97	311	5.225	16.694	113	5.2409
20.39	400	4.299	17.73	222	5.003	17.442	222	5.0177
22.24	133	3.945	20.50	400	4.333	20.166	400	4.3455
25.04	422	3.510	22.36	313	3.976	21.997	133	3.9877
26.58	333	3.309	25.17	422	3.538	24.764	422	3.5481
28.99	404	3.040	26.73	333	3.335	26.292	333	3.3452
30.35	513	2.907	29.15	404	3.064	28.671	404	3.0727
30.79	424	2.866	30.52	513	2.929	30.015	513	2.9381
32.50	602	2.719	30.96	424	2.888	30.451	424	2.897
33.73	335	2.622	32.68	602	2.740	32.141	206	2.7483
34.13	226	2.592	33.92	335	2.643	33.359	533	2.6507
35.70	444	2.482	34.32	622	2.613	35.305	444	2.5089
36.84	515	2.408	35.90	444	2.501	36.429	515	2.434
39.74	355	2.239	37.05	515	2.427	38.239	426	2.3228
41.46	800	2.149	38.89	426	2.316	39.291	355	2.2629
42.47	337	2.101	39.96	355	2.256	40.994	800	2.1727
44.10	822	2.026	41.69	800	2.166	41.988	733	2.1235
45.06	555	1.986	42.71	337	2.117	42.315	446	2.1079
46.63	408	1.923	43.04	644	2.102	43.603	822	2.0485
47.54	537	1.887	44.35	822	2.042	44.55	555	2.0071
47.85	248	1.876	45.32	555	2.001	44.862	266	1.9938
52.24	755	1.728	45.64	626	1.988	46.094	408	1.9434
54.48	737	1.662	46.89	408	1.938	47.001	537	1.9079
54.75	666	1.655	47.82	537	1.902	47.301	248	1.8965
			48.12	824	1.891	48.484	646	1.8529
			49.33	646	1.847	51.634	755	1.747
			50.22	913	1.817	53.841	737	1.6804
			51.68	844	1.769	54.112	666	1.6726
			52.54	755	1.742			
			53.96	268	1.699			
			54.79	737	1.675			

CH_4 hydrate was significantly expanded to higher temperature and lower pressure level. At a given pressure, the dissociation temperatures of the simple CH_4 hydrate (Adisasmito et al., 1991 and this work) were increased by nearly 9, 12, and 18 K due to the addition of ETHF, 12ECH, and 14ECH, respectively. In particular, the 14ECH + CH_4 hydrate did not dissociate up to room temperature (298 K), even under a moderate pressure of ∼60 bar. To compare the degree of the promotion clearly, we illustrate the equilibrium conditions of the CH_4 hydrates containing CH (as a moderately strong promoter) and THF (as a particularly strong promoter) as well in **Figure 4**. Comparing the promoters in similar molecular structures, the promotion effect of ETHF (black empty square) is much weaker than that of THF (Lee et al., 2012 and this work). On the other hand, compared to the CH + CH_4 hydrate (Sun et al., 2002), the 12ECH and 14ECH + CH_4 hydrates (blue and red hexagons, respectively) showed higher dissociation temperatures. Moreover, the thermodynamic stability of the 14ECH + CH_4 hydrate was found to be comparable to that of the THF + CH_4 hydrate. It is notable that the promotion performance of 14ECH is as strong as that of THF, to the best of our knowledge, because THF is known to be one of the most powerful promoters.

We also examined the equilibrium conditions of the three LGM + N_2 hydrates and listed the results in **Table 3**. The addition of the LGMs dramatically improved the dissociation conditions of the simple N_2 hydrate (van Cleeff and Diepen, 1960) to higher temperature and lower pressure levels. All promoters tended to be identical as the CH_4 hydrate systems in terms of the degree of the promotion (**Figure 5**). For the CH + N_2 and THF + N_2 hydrates, we correspondingly referred to Richon and Mohammadi (2011) and Seo et al. (2001). To verify the inclusion of N_2 in the solid hydrate phase, we utilized

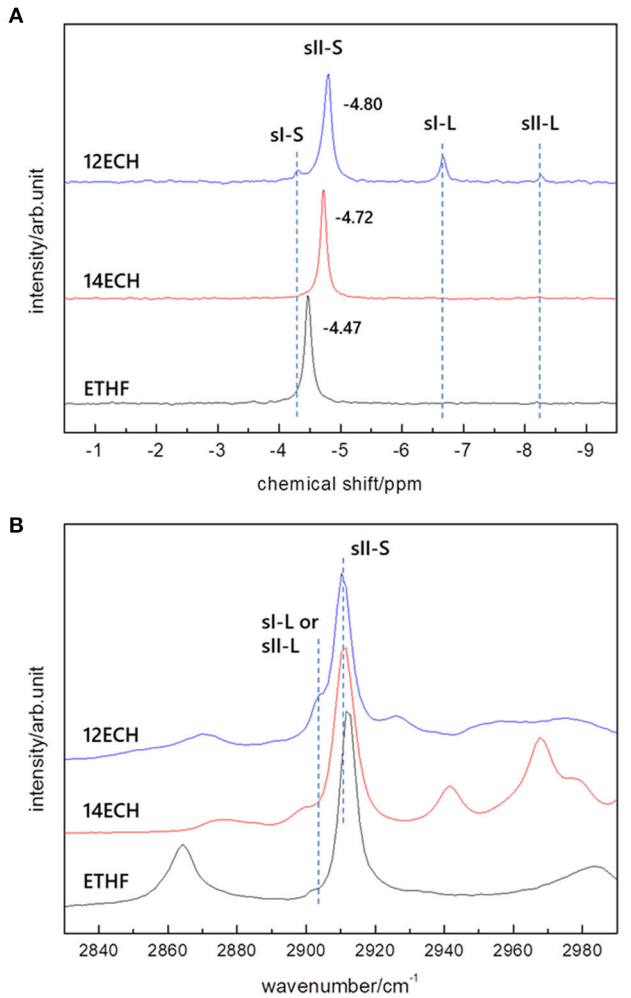

FIGURE 3 | (A) solid-state ^{13}C NMR and **(B)** Raman spectra of the ETHF, 14ECH, and 12 ECH + CH_4 hydrates.

TABLE 2 | Equilibrium P-T conditions of CH_4 hydrates containing three promoters.

ETHF		14ECH		12ECH	
T (K)	P (bar)	T (K)	P (bar)	T (K)	P (bar)
282.0	20.3	292.1	23.5	284.2	19.1
286.2	37.1	295.6	40.9	289.1	39.4
289.7	62.7	298.8	63.5	292.4	60.9
291.7	80.5	300.6	82.4	295.1	85.0

Raman spectroscopy. In **Figure 6**, the peaks near 2,324 cm^{-1} indicate that all LGM + N_2 hydrates were clearly formed. Accordingly, we can conclude that the three novel LGMs serve as promoters for gas hydrates of both spherical and cylindrical types of gaseous molecules.

To find clues by which to understand the powerful promotion of 14ECH, we examined samples that consist only of H_2O and LGMs. Each liquid mixture of LGM + H_2O was slowly cooled from the ambient temperature under continuous stirring to prepare a sufficiently homogeneous solid sample. According to crystallographic analyses, no hydrate phases were observed in the solid samples of ETHF + H_2O and 12ECH + H_2O. On the other hand, the PXRD pattern (**Figure 7** and **Table 4**) clearly

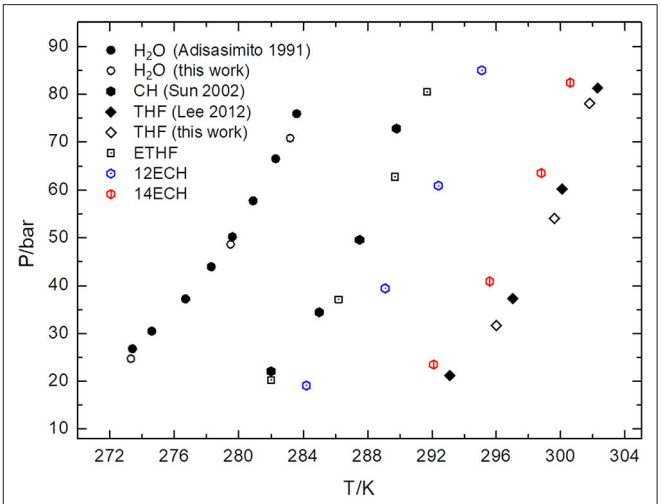

FIGURE 4 | Equilibrium P-T conditions of CH_4 hydrates containing various promoters (x_{LGM} = 0.0556).

TABLE 3 | Equilibrium P-T conditions of N_2 hydrates containing three promoters.

ETHF		14ECH		12ECH	
T (K)	P (bar)	T (K)	P (bar)	T (K)	P (bar)
279.3	68.6	278.4	30.8	279.2	49.3
281.2	90.2	286.9	56.2	281.5	69.3
282.7	110.1	289.5	80.2	283.0	84.1
		291.2	102.4	284.5	106.5

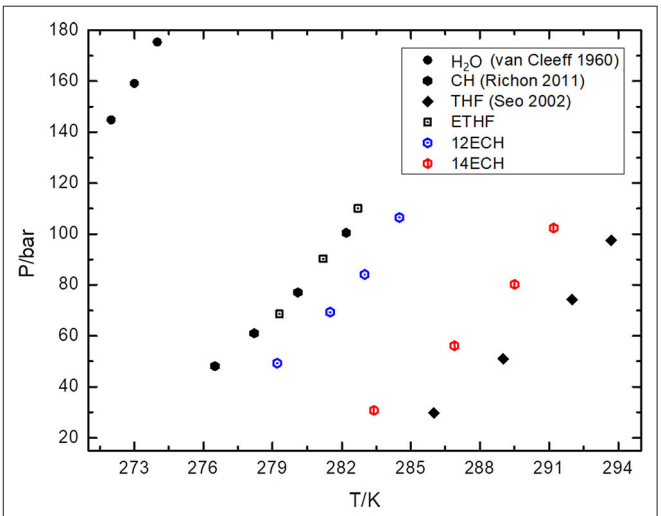

FIGURE 5 | Equilibrium P-T conditions of N_2 hydrates containing various promoters (x_{LGM} = 0.0556).

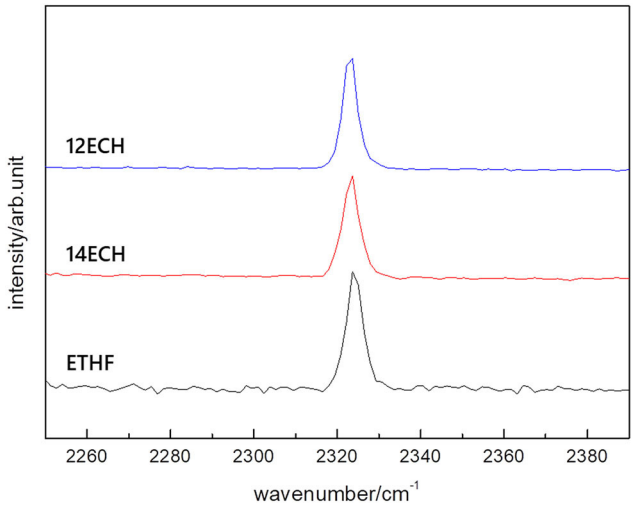

FIGURE 6 | Raman spectra of the LGM + N_2 hydrates measured at 123 K.

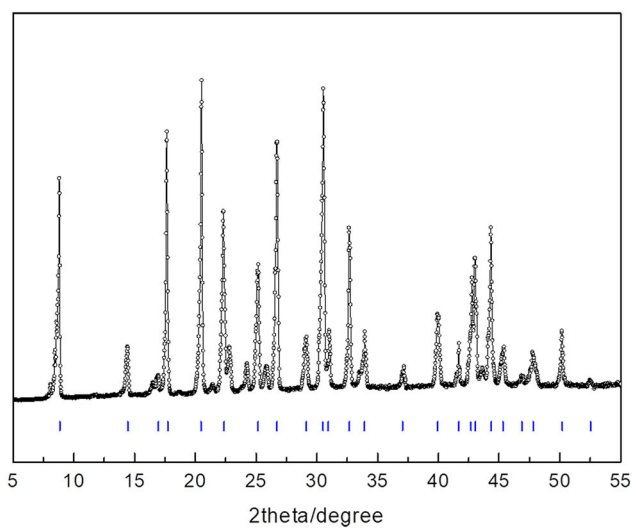

FIGURE 7 | PXRD pattern of the 14ECH + H_2O hydrate (gas-free) at 150 K.

TABLE 4 | Miller indices of the simple 14ECH hydrate shown in **Figure 7**.

Peaks	*hkl*	d_{hkl}
8.84	111	10.007
14.45	202	6.128
16.97	311	5.226
17.73	222	5.004
20.50	004	4.333
22.36	133	3.977
25.17	422	3.538
26.72	333	3.336
29.14	404	3.064
30.51	315	2.930
30.95	424	2.889
32.67	602	2.741
33.91	335	2.643
35.89	444	2.502
37.04	515	2.427
38.88	426	2.316
39.95	355	2.257
41.69	008	2.167
42.70	337	2.118
43.03	644	2.102
44.34	822	2.043
45.31	555	2.001
46.88	048	1.938
47.81	357	1.903
49.32	466	1.848
50.21	913	1.817
51.67	844	1.769
52.53	557	1.742

demonstrated that 14ECH + H_2O forms a simple sII hydrate even in the absence of additional gaseous components. The lattice parameter was determined to be 17.333 Å at 150 K, practically identical to that of the 14ECH + CH_4 hydrate. The inclusion of CH_4 molecules in the sII-S cages appears to have little effect on the lattice size.

To monitor the 14ECH molecules involved in the sII phase clearly, we analyzed the ^{13}C NMR and Raman spectra in detail. The ^{13}C NMR peaks of 14ECH molecules are shown in **Figure 8A**. For the 14ECH + CH_4 hydrate (blue), it was clearly found that the alpha carbons of 14ECH exhibited two separate peaks at 75.3 and 75.9 ppm. The minute peak at 75.9 ppm should be attributed to 14ECH excluded from the hydrate phase, as we introduced a slightly excessive amount of 14ECH compared to the stoichiometric composition (by ∼5%). Consequently, it can be seen that the main peak at 75.3 ppm, being also observed in the simple hydrate of 14ECH, originates from the 14ECH molecules entrapped in the sII-L cages. We also investigated the Raman spectra in detail, focusing on the vibration bands of the 14ECH molecules. In **Figure 8B**, several peaks near 850∼1,000 cm^{-1} are due to symmetric stretching vibrations of the COC group (Socrates, 2001). However, for a comparison with the bands from pure 14ECH (red), those from the 14ECH accommodated in the sII phase clearly appeared at higher wavenumbers. As a free 14ECH molecule becomes confined in the sII-L cage, the COC bonds would contract slightly to increase the force constant of the vibration. In addition, the shortened bond length would increase the electron density around the alpha carbon to provide a more shielded condition. Spectroscopic measurements have thus far been exclusively utilized to monitor the gaseous guest component. However, our outcomes demonstrate convincingly that NMR and Raman spectra are also informative when seeking to determine the behaviors of LGMs.

In addition, the temperatures for the 14ECH hydrate systems at which the principal phase transitions occur were identified by differential scanning calorimetry (DSC) measurements. As seen in **Figure 9A**, the simple 14ECH hydrate starts to

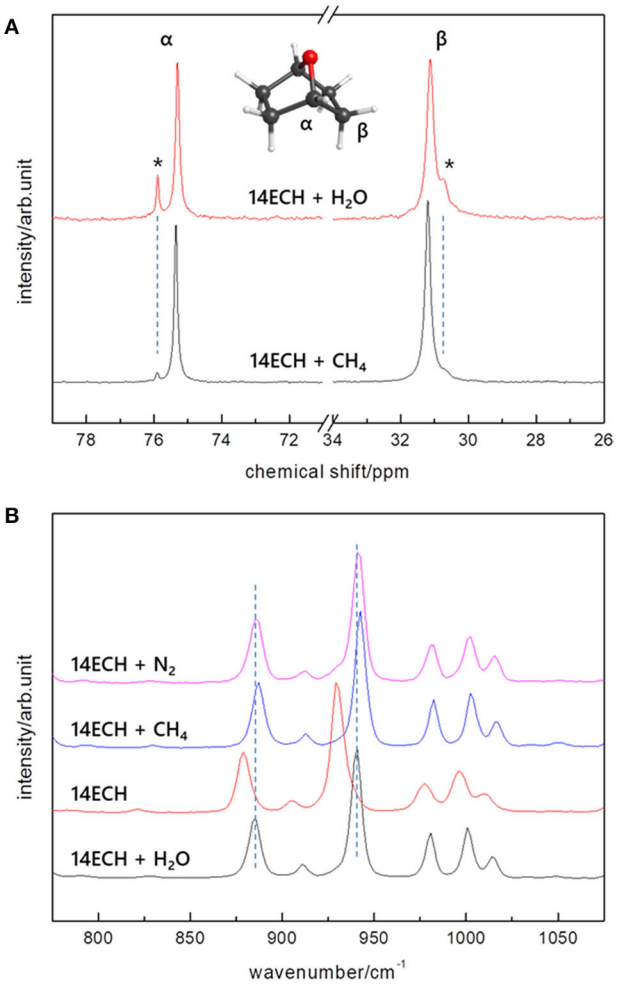

FIGURE 8 | (A) ^{13}C NMR peaks and **(B)** COC vibration bands of the 14ECH molecules.

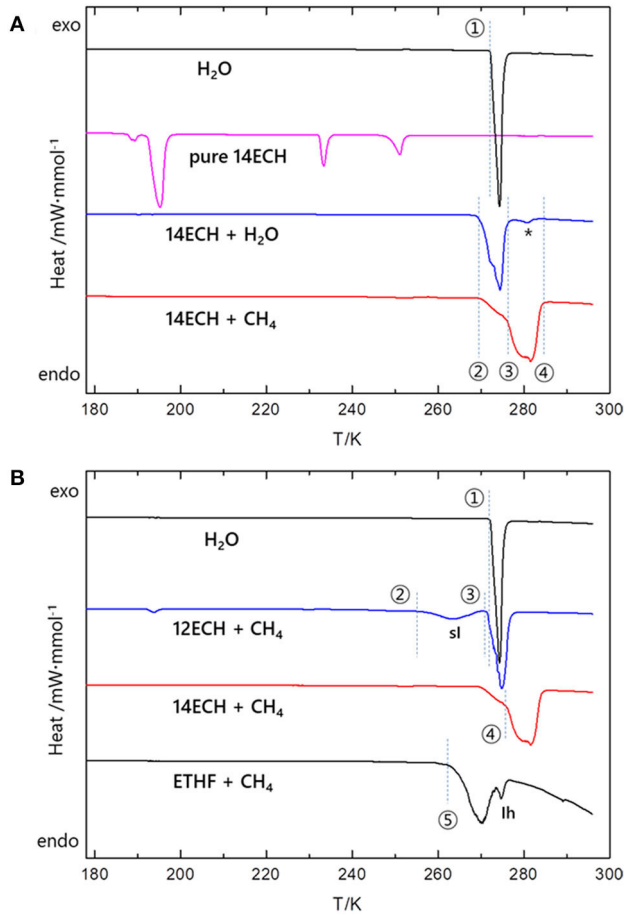

FIGURE 9 | Several principal phase transitions induced by temperature at ambient pressure. **(A)** Four points ①~④ are correspondingly 273, 270, 277, and 285 K. A small peak that may be attributed to the 14ECP + air hydrate (impurity) is denoted by asterisk (*). For clarity, y axis is shown in the same scale. The original heat flows measured in the unit of $mW{\cdot}mg^{-1}$ were normalized by the mole of H_2O (black, blue, and red). For pure 14ECH, the heat flow was normalized by the mole of 14ECH (magenta). **(B)** The five points ①~⑤ at which the phase transitions start to occur are correspondingly 273, 255, 271, 277, and 263 K. The heat flows were normalized by the mole of H_2O.

dissociate at 270 K and fully dissociates at 278 K. For the 14ECH + CH_4 hydrate sample, two phase transitions were mainly observed: (1) the dissociation of a small amount of the 14ECH simple hydrate that are unreacted with gaseous CH_4 (point ②); and (2) the dissociation of the 14ECH + CH_4 hydrate induced by gas release (point ③). Eventually, the 14ECH + CH_4 hydrate fully collapses at approximately 285 K (point ④). Meanwhile, the temperature-induced pattern of pure 14ECH is quite complex that we cannot determine its corresponding phase transitions at the present stage. However, the phase transitions induced by pure 14ECH were observed neither in the 14ECH + CH_4 hydrate nor in the 14ECH simple hydrate. It provides another clear evidence of complete enclathrations of 14ECH molecules in both simple and CH_4 hydrates. In addition, we can conclude that the simple 14ECH hydrate dissociates in the range of 270~278 K, whereas the 14ECH + CH_4 hydrate dissociates in the range of 277~285 K at ambient pressure. In **Figure 9B**, both the onset and end temperatures of gas hydrate dissociations are in the following order: ETHF + CH_4 < 12ECH + CH_4 < 14ECH + CH_4. This is fully consistent with the result of the phase equilibria shown in **Figure 4**.

Thus far, we have demonstrated that 14ECH acts as a simple sII former and that it appears to play a key role in the outstanding promotion effect. Out of the numerous LGMs proposed over the decades, simple hydrate formers are quite rare, except for CFCs. Furthermore, to the best of our knowledge, tetrahydropyran (THP) with a van der Waals diameter of 6.95 Å (Udachin et al., 2002) has been recorded as the largest simple sII former. However, on the basis of our calculation, 14ECH with the longest end-to-end distance of 7.10 Å is larger than THP. [Because the van der Waals radii are not included in **Figure 1**, to obtain the end-to-end distances we should add 1.09 and 1.56 Å to the H and O atoms, respectively (Rowland and Taylor, 1996)]. This is also

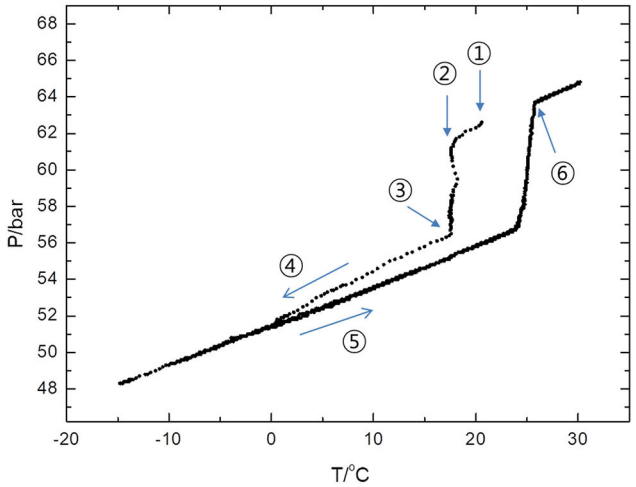

FIGURE 10 | P-T trajectory created by the formation and dissociation processes of the 14ECH + CH_4 hydrate. ① Upon the completion of the gas injection, the temperature inside the vessel was increased to 20°C by adiabatic compression. ② Within 10 min, the vessel was recovered to the ambient temperature (17.5°C) and CH_4 uptake was initiated at the same time. ③ After 40 min, the vessel was immersed in an ethanol bath. ④ The vessel was cooled with a rate of −20 K/h. ⑤ The vessel was heated at a rate of +0.3 K/h. ⑥ The hydrate was fully dissociated at 25.7°C and 63.5 bar.

supported by the fact that the lattice parameter of the 14ECH + H_2O hydrate is somewhat larger than that of the THP + H_2O hydrate (a = 17.289 Å at 153 K) (Takeya et al., 2018). Thus, we believe that this is the first finding of a simple sII former larger than THP.

Finally, we noted that CH_4 uptake takes place rapidly at a significantly high temperature by adding 14ECH. **Figure 10** shows a P-T trajectory created by the formation and dissociation processes of the 14ECH + CH_4 hydrate. It was clearly observed that the pressure began to drop sharply at the ambient temperature to form the hydrate phase. The high temperature of gas uptake may also be attributed to the capability of 14ECH to stabilize the simple hydrate. When the mixture of LGM + H_2O is pressurized with the desired gas, theoretically the hydrate must form just under the equilibrium temperature. Owing to kinetic limitations in most cases, however, one has to cool the systems far below the equilibrium temperature to initiate gas uptake. Accordingly, a sufficiently high temperature of formation is necessary for industrial applications, because the additional time, energy, and cost requirements for further cooling and mixing processes would become considerable. Because the kinetics outcomes strongly depend on the highly various conditions under which the hydrate is formed, including the cell dimensions, initial amounts of the liquid and gas, contact area, stirring rate, and cooling rate, among other factors, diverse studies must of course be further carried out to investigate the detailed kinetic behaviors. At the present stage, however, it is still noteworthy that one can form the 14ECH + CH_4 hydrate at ambient temperatures under a moderate pressure level.

CONCLUSIONS

In this study, CH_4 hydrates containing the three novel LGMs of ETHF, 14ECH, and 12ECH, were synthesized and characterized. According to the crystallographic and spectroscopic outcomes, all hydrates were identified to be sII (Fd-3m) double hydrates, of which the large and small cages were predominantly occupied by LGMs and gaseous molecules, respectively. The thermodynamic stability of each LGM + CH_4 (and N_2) hydrate was remarkably enhanced compared to that of the simple CH_4 (and N_2) hydrate. Particularly, 14ECH manifested several unique features compared to the other two promoters. First, on the basis of clear evidence from PXRD, NMR, Raman and DSC analyses, 14ECH was revealed to be a simple sII former with the largest size ever found. Second, 14ECH exhibited an excellent promotion effect, comparable to that of THF that is currently considered to be the most powerful promoter. In addition to the thermodynamic stability, the 14ECH + CH_4 hydrate presented a sufficiently high temperature of formation, requiring little additional cooling. Given these promising features, we believe that the 14ECH hydrate system can be employed to facilitate hydrate-based technologies. However, because the present study focused mainly on fundamental characterizations of the structure and stability of the materials, for industrial applications, a variety of key engineering points should be studied in future works, including the capacities of gas storage, the kinetics of the gas uptake/release process, the stability of the promoters themselves, optimization of the conditions, and related areas. Finally, we would like to emphasize that the LGMs introduced here have considerable potential to serve as alternates to conventional promoters and that they can be widely utilized in both engineering and scientific research fields. We also believe that the findings and outcomes reported here have extended the fundamentals of clathrate hydrate, especially in relation to functional ice materials.

DATA AVAILABILITY STATEMENT

All datasets presented in this study are included in the article/**Supplementary Material**.

AUTHOR CONTRIBUTIONS

JS planned and managed the entire experiment, prepared and measured samples, analyzed data, produced the figures, and wrote up the draft. JS and WS measured and discussed HRPD data together. JS and JP discussed the outcomes of the equilibrium measurements together. All authors contributed to the article and approved the submitted version.

FUNDING

This research was supported by the Basic Science Research Program through the National Research Foundation of Korea (NRF) funded by the Ministry of Education (2017R1D1A1B03033000).

ACKNOWLEDGMENTS

The HRPD experiments at PLS-II were supported in part by MSICT and POSTECH. The solid-state NMR experiments were conducted at the Bruker AVANCE II 400 MHz NMR system at the KBSI Seoul Western Center. High-resolution Raman and DSC data were acquired from Horiba LabRam HR Evolution and NETZSCH DSC 200 F3 Maia devices, respectively, at Ajou University.

SUPPLEMENTARY MATERIAL

The Supplementary Material for this article can be found online at: https://www.frontiersin.org/articles/10.3389/fchem.2020.00614/full#supplementary-material

REFERENCES

Adisasmito, S., Frank, R. J., and Sloan, E. D. (1991). Hydrates of carbon dioxide and methane mixtures. *J. Chem. Eng. Data* 36, 68–71. doi: 10.1021/je00001a020

Babu, P., Linga, P., Kumar, R., and Englezos, P. (2015). A review of the hydrate based gas separation (HBGS) process for carbon dioxide pre-combustion capture. *Energy* 85, 261–279. doi: 10.1016/j.energy.2015.03.103

Cai, L., Pethica, B. A., Debenedetti, P. G., and Sundaresan, S. (2016). Formation of cyclopentane methane binary hydrate in brine solutions. *Chem. Eng. Sci.* 141, 125–132. doi: 10.1016/j.ces.2015.11.001

Florusse, L. J., Peter, C. J., Schoonman, J., Hester, K. C., Koh, C. A., Dec, S. F., et al. (2004). Stable low-pressure hydrogen clusters stored in binary clathrate hydrate. *Science* 306, 469–471. doi: 10.1126/science.1102076

Frisch, M. J., Trucks, G. W., Schlegel, H. B., Scuseria, G. E., Robb, M. A., Cheeseman, J. R., et al. (2004). *Gaussian 03, Revision C.01*. Wallingford, CT: Gaussian Inc.

Lee, Y.-J., Kawamura, T., Yamamoto, Y., and Yoon, J.-H. (2012). Phase equilibrium studies of tetrahydrofuran (THF) + CH_4, THF + CO_2, CH_4 + CO_2, and THF + CO_2 + CH_4 hydrates. *J. Chem. Eng. Data* 57, 3543–3548. doi: 10.1021/je300850q

Li, L.-T., Chen, Y.-P., and Tang, M. (2020). Experimental measurements for the dissociation conditions of methane hydrate mixture with each additive of acetamide, cyclopentanol, or 1,3-dioxane. *J. Chem. Eng. Data* 65, 177–184. doi: 10.1021/acs.jced.9b00862

Nakajima, M., Ohmura, R., and Mori, Y. H. (2008). Clathrate hydrate formation from cyclopentane-in-water emulsions. *Ind. Eng. Chem. Res.* 47, 8933–8939. doi: 10.1021/ie800949k

Pahlavanzadeh, H., Khanlarkhani, M., and Mohammadi, A. H. (2016). Clathrate hydrate formation in (methane, carbon dioxide or nitrogen + tetrahydropyran or furan + water) system: thermodynamic and kinetic study. *J. Chem. Thermodyn.* 92, 168–174. doi: 10.1016/j.jct.2015.08.034

Park, Y., Dho, J., Seol, J., Yeon, S.-H., Cha, M., Jeong, Y. H., et al. (2009). Magnetic transition and long-time relaxation behavior induced by selective injection of guest molecules into clathrate hydrates. *J. Am. Chem. Soc.* 131, 5736–5737. doi: 10.1021/ja9009088

Park,. Y., Kim, D.-Y., Lee, J.-W., Huh, D.-G., Park, K.-P., Lee, J., et al. (2006). Sequestering carbon dioxide into complex structures of naturally occurring gas hydrates. *Proc. Nat. Acad. Sci. U.S.A.* 103, 12690–12694. doi: 10.1073/pnas.0602251103

Richon, D., and Mohammadi, A. H. (2011). Phase equilibria of binary clathrate hydrates of nitrogen + cyclopentane/cyclohexane/methyl cyclohexane and ethane + cyclopentane/cyclohexane/methyl cyclohexane. *Chem. Eng. Sci.* 66, 4936–4940. doi: 10.1016/j.ces.2011.06.014

Rowland, R. S., and Taylor, R. (1996). Intermolecular nonbonded contact distances in organic crystal structures: comparison with distances expected from van der Waals radii. *J. Phys. Chem.* 100, 7384–7391. doi: 10.1021/jp953141+

Seo, Y., Lee, J.-W., Kumar, R., Moudrakovski, I. L., Lee, H., and Ripmeester, J. A. (2009). Tuning the composition of guest molecules in clathrate hydrates: NMR identification and its significance to gas storage. *Chem. Asian J.* 4, 1266–1274. doi: 10.1002/asia.200900087

Seo, Y.-T., Kang, S.-P., and Lee, H. (2001). Experimental determination and thermodynamic modeling of methane and nitrogen hydrates in the presence of THF, propylene oxide, 1,4-dioxane and acetone. *Fluid Phase Equilib.* 189, 99–110. doi: 10.1016/S0378-3812(01)00580-5

Seo, Y.-T., Moudrakivski, I. L., Ripmeester, J. A., Lee, J.-W., and Lee, H. (2005). Effective recovery of CO_2 from flue gas by clathrate hydrate formation in porous silica gels. *Environ. Sci. Technol.* 39, 2315–2319. doi: 10.1021/es049269z

Seol, J., Shin, W., Koh, D.-Y., Kang, H., Sung, B., and Lee, H. (2012). Spectroscopic observation of Na cations entrapped in small cages of sII propane hydrate. *J. Phys. Chem. C* 116, 1439–1444. doi: 10.1021/jp207450e

Shin, K., Cha, J.-H., Seo, Y., and Lee, H. (2009). Physicochemical properties of ionic clathrate hydrates. *Chem. Asian J.* 5, 22–34. doi: 10.1002/asia.200900219

Shin, W., Park, S., Ro, H., Koh, D.-Y., Seol, J., and Lee, H. (2012). Phase equilibrium measurements and the tuning behavior of new sII clathrate hydrates. *J. Chem. Thermodyn.* 44, 20–25. doi: 10.1016/j.jct.2011.08.018

Shin,. K., Park, Y., Cha, M., Park, K.-P., Huh, D.-G., Lee, J., et al. (2008). Swapping phenomena occurring in deep-sea gas hydrates. *Energy Fuel* 22, 3160–3163. doi: 10.1021/ef8002087

Socrates, G. (2001). *Infrared and Raman Characteristic Group Frequencies: Tables and Charts, 3rd Edn*. Chichester, UK: John Wiley and Sons Ltd.

Sun, Z.-G., Fan, S.-S., Guo, K.-H., Shi, L., Guo, Y.-K., and Wang, R.-Z. (2002). Gas hydrate phase equilibrium data of cyclohexane and cyclopentane. *J. Chem. Eng. Data* 47, 313–315. doi: 10.1021/je0102199

Takeya, S., Alavi, S., Hashimoto, S., Yasuda, K., Yamauchi, Y., and Ohmura, R. (2018). Distortion of the large cages encapsulating cyclic molecules and empty small cages of structure II clathrate hydrates. *J. Phys. Chem. C* 122, 18134–18141. doi: 10.1021/acs.jpcc.8b05314

Udachin, K. A., Ratcliffe, C. I., and Ripmeester, J. A. (2002). Single crystal diffraction studies of structure I, II and H hydrates: structure, cage occupancy and composition. *J. Supramol. Chem.* 2, 405–408. doi: 10.1016/S1472-7862(03)00049-2

van Cleeff, A., and Diepen, G. A. M. (1960). Gas hydrates of nitrogen and oxygen. *Recl. Trav. Chim. Pays Bas.* 79, 582–586. doi: 10.1002/recl.19600790606

Veluswamy, H. P., Wong, A. J. H., Babu, P., Kumar, R., Kulprathipanja, S., Rangsunvigit, P., et al. (2016). Rapid methane hydrate formation to develop a cost effective large scale energy storage system. *Chem. Eng. J.* 290, 161–173. doi: 10.1016/j.cej.2016.01.026

Yeon, S.-H., Seol, J., and Lee, H. (2006). Structure transition and swapping pattern of clathrate hydrates driven by external guest molecules. *J. Am. Chem. Soc.* 128, 12388–12389. doi: 10.1021/ja062937r

Yeon, S.-H., Seol, J., Park, Y., Koh, D.-Y., Kang, Y. S., and Lee, H. (2008). Spectroscopic observation of atomic hydrogen radicals entrapped in icy hydrogen hydrate. *J. Am. Chem. Soc.* 130, 9208–9209. doi: 10.1021/ja802952p

Conflict of Interest: WS and JP were employed by the company Hyundai Oilbank Co., Ltd. and Daewoo Shipbuilding and Marine Engineering Co., Ltd., respectively.

The remaining author declares that the research was conducted in the absence of any commercial or financial relationships that could be construed as a potential conflict of interest.

frontiers in Chemistry

MINI REVIEW
published: 06 October 2020
doi: 10.3389/fchem.2020.526101

Promotion of Activated Carbon on the Nucleation and Growth Kinetics of Methane Hydrates

Guodong Zhang[1,2], *Xiaoyun Shi*[1], *Runcheng Zhang*[1], *Kun Chao*[1] *and Fei Wang*[1]*

[1] College of Electromechanical Engineering, Shandong Engineering Laboratory for Preparation and Application of High-Performance Carbon-Materials, Qingdao University of Science and Technology, Qingdao, China, [2] Key Laboratory of Unconventional Oil & Gas Development [China University of Petroleum (East China)], Ministry of Education, Qingdao, China

Due to the hybrid effect of physical adsorption and hydration, methane storage capacity in pre-adsorbed water-activated carbon (PW-AC) under hydrate favorable conditions is impressive, and fast nucleation and growth kinetics are also anticipated. Those fantastic natures suggest the PW-AC-based hydrates to be a promising alternative for methane storage and transportation. However, hydrate formation refers to multiscale processes, the nucleation kinetics at molecule scale give rise to macrohydrate formation, and the presence of activated carbon (AC) causes this to be more complicated. Although adequate nucleation sites induced by abundant specific surface area and pore texture were reported to correspond to fast formation kinetics at macroperspective, the micronature behind that is still ambiguous. Here, we evaluated how methane would be adsorbed on PW-AC under hydrate favorable conditions to improve the understanding of hydrate fast nucleation and growth kinetics. Microbulges on AC surface were confirmed to provide numerous nucleation sites, suggesting the contribution of abundant specific surface area of AC to fast hydrate nucleation and growth kinetics. In addition, two-way convection of water and methane molecules in micropores induced by methane physical adsorption further increases gas–liquid contact at molecular scale, which may constitute the nature of confinement effect of nanopore space.

Keywords: methane hydrates, activated carbon, nucleation and growth kinetics, confinement effect, hydrate fibers, two-way convection mechanism

OPEN ACCESS

Edited by:
Sotiris Sotiropoulos, Aristotle University of Thessaloniki, Greece

Reviewed by:
Jianyang Wu, Xiamen University, China
Chungang Xu, Guangzhou Institute of Energy Conversion (CAS), China

***Correspondence:**
Fei Wang
elliot_wang@qust.edu.cn

Specialty section:
This article was submitted to Physical Chemistry and Chemical Physics, a section of the journal Frontiers in Chemistry

Received: *12 January 2020*
Accepted: *08 September 2020*
Published: *06 October 2020*

Citation:
Zhang G, Shi X, Zhang R, Chao K and Wang F (2020) Promotion of Activated Carbon on the Nucleation and Growth Kinetics of Methane Hydrates. Front. Chem. 8:526101. doi: 10.3389/fchem.2020.526101

INTRODUCTION

As one of the most promising energy resources, natural gas hydrates gradually get more and more attention, which are stored in permafrost and marine with huge reserves (Sloan, 2003). Unfortunately, such a big piece of cake is not easy to enjoy because of potential tremendous risks, such as seabed geological disasters and greenhouse effect. Hydrates are clathrate structures bonded by water molecules with hydrogen bonds, while guest molecules are captured under demanding conditions (high pressure and low temperature) (Sloan and Koh, 2007). For methane hydrate crystal, a non-stoichiometric composition of $8CH_4{\cdot}46H_2O$ usually forms with theorical methane storage capacity of ca. 172 m^3 under standard condition, and this fantastic nature anticipates hydrates to be a promising alternative for the storage and transportation of natural gas, i.e., solid natural gas (SNG), especially in the point of view of cost saving and safety. However, there are technical limits toward industrial application of the SNG technology as a consequence of slow

hydrate formation kinetics and low methane storage capacity, so various promoters were employed to overcome such limits, which generally fall into two categories, thermodynamic promoters and kinetic ones (Mech et al., 2016; He et al., 2019).

Hydrate formation is governed by heat and mass transfer, which are improved by interface areas (Clarke and Bishnoi, 2000; Mohebbi et al., 2012), and the presence of solid surfaces can also enhance heterogeneous nucleation (Kvamme et al., 2007; Walsh et al., 2009). Therefore, due to high specific surface area and abundant pore texture, various porous media were reported to significantly enhance hydrate formation kinetics. Typical examples include molecular sieves (Zhou et al., 2005a; Zhong et al., 2016; Liu et al., 2018; Zhao et al., 2018), carbon nanotubes (Park et al., 2010; Zhao et al., 2014), graphite nanoparticles (Zhou et al., 2014; Yu et al., 2016, 2018), MOFs (Mu et al., 2012; Casco et al., 2016), and activated carbon (Zhou et al., 2002, 2005b, 2010; Perrin et al., 2004; Sun et al., 2007; Babu et al., 2013; Borchardt et al., 2018). Impressively, when AC was used, a short or even no induction period was commonly observed (Casco et al., 2015; Borchardt et al., 2016; Cuadrado-Collados et al., 2018), and water can be completely converted to hydrates within 2 h, accompanied with high methane storage capacity (∼200 V/V) (Zhang et al., 2020). These fantastic characteristics suggest the possibility of the PW-AC-based SNG technology. However, the fast nucleation and growth mechanisms of methane hydrates loaded by AC have remained, for the most part, unanswered. Keeping this in mind, here we report how methane would be absorbed on PW-AC under hydrate-favorable conditions and evaluate potential micromechanisms behind the fast nucleation and growth kinetics.

HOW METHANE WOULD BE ADSORBED ON PW-AC

When PW-AC is used to store methane under hydrate favorable conditions, impressive phenomena are commonly observed, giving rise to hybrid adsorption mechanisms of physical adsorption and hydrate formation. A typical adsorption isotherm (Casco et al., 2017) is shown in **Figure 1A**, indicating a discrete three-stage adsorption. Apparently, methane physical adsorption in micropores contributes to methane uptake in the first stage, which is almost nil because of steric restriction. However, it significantly depends on the chemical properties of the AC surface, and since strong water molecule–AC surface interaction enhances steric restriction, hydrophobic carbon materials were known as adsorbing more methane (Casco et al., 2019), and some porous materials were even reported to have no influence on methane physical adsorption (Casco et al., 2016). Subsequently, when pressure exceeds a threshold value, i.e., equilibrium pressure, drastic methane uptake occurs that associates with hydrate formation at large pores or pore mouths. It is worth to note that the pressure is higher than that in bulk water because of capillary action (Zhou et al., 2002; Perrin et al., 2004; Liu et al., 2011; Casco et al., 2017), and the extra driving force to overcome capillary action is even higher than 1.5 MPa (see in **Table 1**). Interestingly, another fast methane consumption stage is observed at higher pressure, which was reported to correspond to hydrate formation in micropores or small mesopores (Casco et al., 2015; Cuadrado-Collados et al., 2018). In addition, it is also worth to note that when hydrate formation kinetics are taken into account by evaluating pressure evolution, new information with more details is observed. We found a three-stage kinetic behavior during hydrate formation as shown in **Figure 1B**, methane physical adsorption occurs soon after the experimental pressure is reached, followed by a hydration induction period, and eventually hydrates form causing methane quick consumption. This observation constitutes clear evidence on the hybrid effect of methane physical adsorption and hydrate formation on methane storage in PW-AC under hydrate-favorable conditions, so it is not surprising that high methane storage capacity is commonly reported as shown in **Table 1**.

Another promising finding for PW-AC-based hydrates is that the presence of AC significantly enhances hydrate nucleation and growth kinetics. Because of the stochastic nature of hydrate nucleation, it is anticipated that the process of qualitative change caused by quantitative change governs hydrate nucleation and growth, so adequate nucleation sites are paramount corresponding to fast formation kinetics at macroperspective. As for activated carbon, abundant specific surface area and pore texture are well-known, which significantly enhance gas–liquid contract and provide tremendous potential nucleation sites, and this constitutes the macromechanisms contributing to fast hydrate nucleation and growth. However, because of complicated surface properties and pore texture, the micronature behind the macromechanisms is still unclear. One of the most appreciated factors was reported to be the chemical properties of AC surface, e.g., surface defect (Pirzadeh and Kusalik, 2013) and hydrophobic or hydrophilic properties (Casco et al., 2017, 2019; Nguyen et al., 2017), which can change the interaction between water molecules and AC surface. Water molecules are known to assemble at the sites which are occupied by surface-deflecting and oxygen-containing functional groups to form clusters, which may provide potential nucleation sites and constitute a hydrate precursor. However, some researchers argued that hydrophobic surface is more efficient, where water molecular clusters occupy the center of inner pores, while methane molecules enrich on the surface (Billemont et al., 2011; Nguyen et al., 2017). In addition, abundant pore texture of AC was also reported to promote hydrate nucleation and growth, i.e., confinement effect, which is considered to remarkably accelerate hydrate nucleation, even within minutes (Casco et al., 2015; Cuadrado-Collados et al., 2018). It is interesting to note that when water and methane molecules exist in a nanopore space, they exhibit a different behavior compared to those out of such confined space under the same conditions. It is well-known that the nanoconfinement effect equals high pressure, the so-called quasi-high-pressure effect (Urita et al., 2011; Fujimori et al., 2013), so solid water was observed in such a pore space because of low activity of water molecules, presenting an ice-like structure, which are thought to enhance hydrate nucleation. Nevertheless, non-freezing water was also reported in a confined nanopore space, which cannot contribute to hydrate formation (Casco et al., 2019; Cuadrado-Callados et al., 2019). Therefore, how the confined pore space

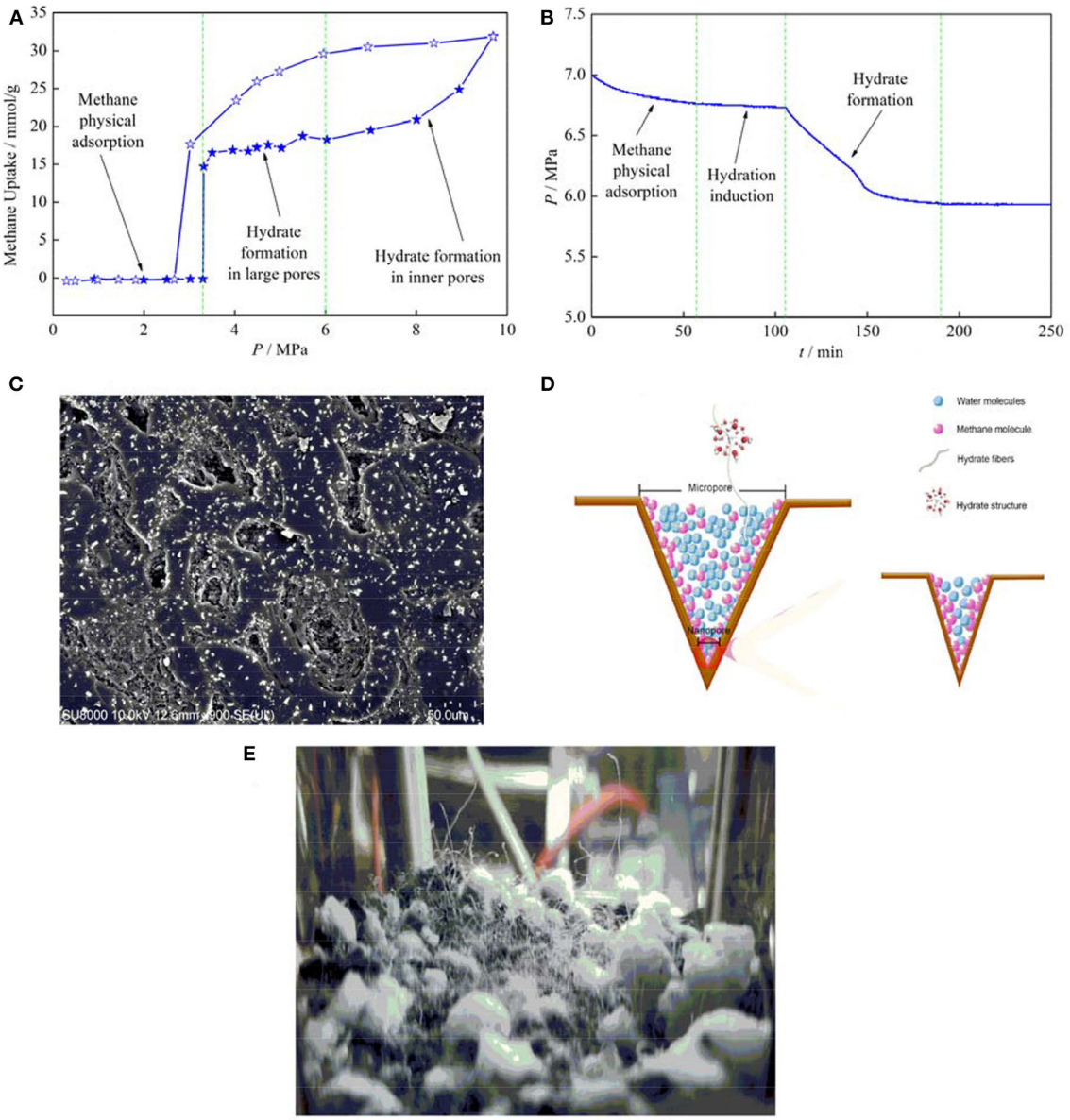

FIGURE 1 | (A) Adsorption isotherm, filled pentagrams refer to an adsorption curve, while open ones indicate a desorption curve (Casco et al., 2017) [reproduced with permission from Casco et al. (2017), copyright 2017 Elsevier]. **(B)** Pressure evolution during hydrate formation. **(C)** SEM picture of activated carbon (AC) surface; white substance covering on microbulges refers to NaCl. **(D)** Schematic of two-way convection of water and methane molecules in pore space induced by methane physical adsorption in micropores. **(E)** Hydrate fibers on AC bed.

influences hydrate nucleation and growth is still unclear due to lack of effective characterization methods at a molecular scale.

Hydrate formation refers to a multiscale process. The nucleation kinetics at a molecule scale give rise to hydrate formation at a macroscale, and the presence of AC causes this to be more complicated. However, the point one should keep in mind is that regardless of what the nature of fast nucleation and growth kinetics of hydrates loaded by AC is, the reason behind that at macroperspective must depend on the increased tremendous potential nucleation sites caused by abundant specific surface area and pore texture. The SEM picture of AC particles is given in **Figure 1C**. The AC particles were first mixed with a small amount of NaCl solution (unsaturated, only little water remains on AC surfaces) and then quickly frozen to −50°C. Finally, the AC particles were dried by vacuuming, so NaCl would remain on the surface of the AC particles. It is clear from **Figure 1C** that there are many microbulges (<5 μm) on the surface of AC particles, which are covered by NaCl and show white, indicating that water used to concentrate at these locations, where they would provide nucleation sites for hydrates.

TABLE 1 | Gas storage capacity in preadsorbed water activated carbon (AC).

Activated carbon	Equilibrium condition	Experimental condition	Gas storage capacity/g·g^{-1}	R_w †	References
PP-AC	3.0 MPa, 2°C	10 MPa, 2°C	0.63	4.1	Casco et al., 2015
PP-AC_Ox	3.3 MPa, 2°C	10 MPa, 2°C	0.36	4.1	Casco et al., 2017
C_{meso-2}	2.49 MPa, −9°C	8.3 MPa, −9°C	0.34	2.46	Borchardt et al., 2016
Coconut-based AC	4.6 MPa, 1.85°C	10 MPa, 1.85°C	0.32	1.4	Zhou et al., 2002
Corncob-based AC	4.23 MPa, ca. 2°C	9.4 MPa, ca. 1.85°C	0.63	3.35	Liu et al., 2011
CMK_3_1.25	3.27 MPa, ca. 2°C	11.8 MPa, 1.85°C	0.66	3.86	Liu et al., 2006
NC120	3.99 MPa, 4°C	8.5 MPa, 4°C	0.28	1.0	Najibi et al., 2008
NC120	3.49 MPa, 2°C	8 MPa, 2°C	0.35	1.0	Perrin et al., 2004
Picazine	3.7 MPa, 2°C		0.57	ca. 1.0	

† *Mass ratio of water to activated carbon used in hydrate formation experiments.*

Since surface bulges are small and densely distributed on the surface of AC particles, this finding constitutes clear evidence that AC-abundant specific surface area contributes to hydrate fast nucleation and growth kinetic. The last but not the least, it is also worth to note that hydrates usually nucleate during the physical adsorption stage, and we have not observed an induction period in more than 80% of the hydrate formation experiments loaded by AC (Zhang et al., 2020), so it is safe to speculate that there should be a potential relationship between methane physical adsorption and hydrate nucleation. For hydrophobic AC, water molecules commonly occupy the center of a pore space, so the adsorbed methane molecules penetrate into the inner pore through the channel between the pore wall and the water molecules. In addition, methane adsorption in micropores was reported to induce an outward migration of water molecules (Casco et al., 2019), so two-way convection of water and methane molecules in a pore space occurs as shown in **Figure 1D**, and the enhanced molecular fluidity in a confined pore space significantly increases gas–liquid contact at the molecular scale, which further drastically increases nucleation sites. More details can be found in Zhang et al. (2020). Interestingly, it is clear from **Figure 1E** that a lot of hydrate fibers form, which grow out from inner pores. This suggests that part of hydrates nucleate in inner pores, and the promotion of confinement effect on hydrate nucleation and growth is also confirmed. To end up, despite the effective characterization methods at the molecular scale required to evaluate hydrate nucleation and growth kinetics loaded by AC, these findings open new perspective to understand the nature behind fast hydrate nucleation and growth kinetics.

DISCUSSION

The PW-AC-based SNG technology was thought to overcome all the drawbacks of ANG (Zhou et al., 2004), giving rise to higher methane storage capacity and full reversibility of methane, providing this technology is one of the most promising alternatives, but effort is still needed to pay to promote its industrial application. Despite the fast nucleation and growth kinetics commonly observed, one reason behind that is that a tiny amount of AC was usually used, but the scenario changes completely at the industrial scale, where large AC beds retard methane dispersion and decreases gas–liquid contact. Therefore, AC packing density should be carefully considered and optimized (Perrin et al., 2003), which is one of the paramount factors that influence methane storage, transportation, and hydrate formation kinetics. Generally, a dynamic crystallizer may be more efficient to overcome this retardation effect, which may further enhance hydrate formation kinetics. In addition, since the hybrid effect, the total methane storage capacity can be enhanced by improving methane uptake in physical adsorption and hydrate separately, which depends on the physical and chemical properties of AC surface, pore size, and the contents of pre-adsorbed water, etc. As abovementioned, despite hydrophilic surface is considered to correspond to fast hydrate formation kinetics, hydrophobic carbon materials usually associate with higher methane storage capacity, so AC surface modification should be carefully carried out. Furthermore, the contents of pre-adsorbed water can significantly affect the accessibility of inner pores, so an optimal water–AC mass ratio (R_w) exists, corresponding to the maximum methane storage capacity and depending on the chemical properties of the AC surface (Celzard and Marêché, 2006; Mahboub et al., 2012; Zhang et al., 2014). Other than that, it is worth to note that R_w also affects hydrate nucleation and growth kinetics, hydrate density, and morphologies, so the optimal R_w should be addressed by taking all those factors into account. The last but not the least, hydrate nucleation and growth kinetics also notably depends on the physical properties of AC, especially the distribution of AC size and pore size. Small AC was reported to correspond to fast nucleation and growth kinetics because of more abundant specific surface area, while larger AC provides adequate interstitial pore space, giving rise to higher methane storage capacity (Siangsai et al., 2015). Moreover, because the lattice size of SI hydrate crystal is ca. 1.2 nm, the minimum pore size for hydrate nucleation was reported to be 1.6 nm (Liu et al., 2011), while the optimal pore size was evaluated to be ca. 25 nm (Borchardt et al., 2016). Ultimately, each kind of AC is unique, so its physical and chemical properties must be evaluated in detail before application, and more efficient AC with appropriate size distribution, pore width, surface properties, etc., should be

designed and fabricated to improve hydrate formation kinetics and methane storage capacity (Borchardt et al., 2018).

CONCLUSION

Although slow nucleation and growth kinetics limit the industrial application of the SNG technology, the introduction of activated carbon sheds light on it, accompanied with fast hydrate formation kinetics and high methane storage capacity, whereas the mechanisms behind that has not been clearly discussed. The promotion of surface defect, oxygen-containing functional groups, surface physical and chemical properties, and confinement effect have been commonly presented, but they seem not to constitute the essence of fast hydrate formation kinetics. Generally, because of the stochastic nature of hydrate nucleation, it is anticipated that the qualitative change (macro formation) caused by quantitative change (micro multisite nucleation) governs hydrate formation kinetics. Therefore, the increased tremendous potential nucleation sites caused by abundant specific surface area and pore texture should correspond to fast hydrate formation kinetics at macroperspective, and the nature behind them may be numerous microbulges on the surface of AC particles and two-way convection of methane/water molecules induced by methane physical adsorption in micropores.

AUTHOR CONTRIBUTIONS

FW prepared the manuscript. GZ wrote the manuscript. XS, RZ, and KC reviewed the manuscript and provided comments, suggestions, and edits. All authors contributed to the article and approved the submitted version.

FUNDING

This study was supported by the Natural Science Foundation of Shandong Province, China (Grant No. ZR2018BEE005), National Natural Science Foundation of China (Grant Nos. 51804175, 21706269, and 21978142), the Youth Innovation Talent Development Project for Universities of Shandong Province, the Taishan Scholar Project of Shandong Province, the Opening Fund of Key Laboratory of Unconventional Oil & Gas Development [China University of Petroleum (East China)], the Ministry of Education, and the Fundamental Research Funds for the Central Universities.

REFERENCES

Babu, P., Yee, D., Linga, P., Palmer, A., Khoo, B. C., Tan, T. S., et al. (2013). Morphology of methane hydrate formation in porous media. *Energy Fuels* 27, 3364–3372. doi: 10.1021/ef4004818

Billemont, P., Coasne, B., and De Weireld, G. (2011). An experimental and molecular simulation study of the adsorption of carbon dioxide and methane in nanoporous carbons in the presence of water. *Langmuir* 27, 1015–1024. doi: 10.1021/la103107t

Borchardt, L., Casco, M. E., and Silvestre-Albero, J. (2018). Methane hydrate in confined spaces: an alternative storage system. *ChemPhysChem* 19, 1298–1314. doi: 10.1002/cphc.201701250

Borchardt, L., Nickel, W., Casco, M., Senkovska, I., Bon, V., Wallacher, D., et al. (2016). Illuminating solid gas storage in confined spaces-methane hydrate formation in porous model carbons. *Phys. Chem. Chem. Phys.* 18, 20607–20614. doi: 10.1039/C6CP03993F

Casco, M. E., Cuadrado-Collados, C., Martínez-Escandell, M., Rodríguez-Reinoso, F., and Silvestre-Albero, J. (2017). Influence of the oxygen-containing surface functional groups in the methane hydrate nucleation and growth in nanoporous carbon. *Carbon* 123, 299–301. doi: 10.1016/j.carbon.2017.07.061

Casco, M. E., Rey, F., Jordá, J. L., Rudić, S., Fauth, F., Martínez-Escandell, M., et al. (2016). Paving the way for methane hydrate formation on metal-organic frameworks (MOFs). *Chem. Sci.* 7, 3658–3666. doi: 10.1039/C6SC00272B

Casco, M. E., Silvestre-Albero, J., Ramírez-Cuesta, A. J., Rey, F., Jordá, J. L., Bansode, A., et al. (2015). Methane hydrate formation in confined nanospace can surpass nature. *Nat. Commun.* 6:6432. doi: 10.1038/ncomms7432

Casco, M. E., Zhang, E., Grätz, S., Krause, S., Bon, V., Wallacher, D., et al. (2019). Experimental evidence of confined methane hydrate in hydrophilic and hydrophobic model carbons. *J. Phys. Chem. C* 123, 24071–24079. doi: 10.1021/acs.jpcc.9b06366

Celzard, A., and Marêché, J. F. (2006). Optimal wetting of active carbons for methane hydrate formation. *Fuel* 85, 957–966. doi: 10.1016/j.fuel.2005.10.019

Clarke, M., and Bishnoi, P. R. (2000). Determination of the intrinsic rate of ethane gas hydrate decomposition. *Chem. Eng. Sci.* 55, 4869–4883. doi: 10.1016/S0009-2509(00)00137-8

Cuadrado-Callados, C., Majid, A. A., Martínez-Escandell, M., Daemen, L. L., Missyul, A., Koh, C. A., et al. (2019). Freezing/melting of water in the confined nanospace of carbon materials: effect of an external stimulus. *Carbon* 158, 346–355. doi: 10.1016/j.carbon.2019.10.081

Cuadrado-Collados, C., Fauth, F., Such-Basañez, I., Martínez-Escandell, M., and Silvestre-Albero, J. (2018). Methane hydrate formation in the confined nanospace of activated carbons in seawater environment. *Microporous Mesoporous Mater.* 255, 220–225. doi: 10.1016/j.micromeso.2017.07.047

Fujimori, T., Morelos-Gómez, A., Zhu, Z., Muramatsu, H., Futamura, R., Urita, K., et al. (2013). Conducting linear chains of sulphur inside carbon nanotubes. *Nat. Commun.* 4:2162. doi: 10.1038/ncomms3162

He, Y., Sun, M. T., Chen, C., Zhang, G. D., Chao, K., Lin, Y., et al. (2019). Surfactant-based promotion to gas hydrate formation for energy storage. *J. Mater. Chem. A* 7, 21634–21661. doi: 10.1039/C9TA07071K

Kvamme, B., Graue, A., Buanes, T., Kuznetsova, T., and Ersland, G. (2007). Storage of CO_2 in natural gas hydrate reservoirs and the effect of hydrate as an extra sealing in cold aquifers. *Int. J. Greenhouse Gas Control.* 1, 236–246. doi: 10.1016/S1750-5836(06)00002-8

Liu, J., Zhou, Y., Sun, Y., Su, W., and Zhou, L. (2011). Methane storage in wet carbon of tailored pore sizes. *Carbon* 49, 3731–3736. doi: 10.1016/j.carbon.2011.05.005

Liu, X., Liu, D., Xie, W., Cui, X., and Chen, Y. (2018). Methane hydrate uptake of MCM-41 mesoporous molecular sieves with preadsorbed water. *J. Chem. Eng. Data* 63, 1767–1772. doi: 10.1021/acs.jced.8b00060

Liu, X., Zhou, L., Li, J., Sun, Y., Su, W., and Zhou, Y. (2006). Methane sorption on ordered mesoporous carbon in the presence of water. *Carbon* 44, 1386–1392. doi: 10.1016/j.carbon.2005.11.018

Mahboub, M. J. D., Ahmadpour, A., and Rashidi, H. (2012). Improving methane storage on wet activated carbons at various amounts of water. *J. Fuel Chem. Technol.* 40, 385–389. doi: 10.1016/S1872-5813(12)60017-6

Mech, D., Gupta, P., and Sangwai, J. S. (2016). Kinetics of methane hydrate formation in an aqueous solution of thermodynamic promoters (THF and TBAB) with and without kinetic promoter (SDS). *J. Nat. Gas Sci. Eng.* 35, 1519–1534. doi: 10.1016/j.jngse.2016.06.013

Mohebbi, V., Naderifar, A., Behbahani, R. M., and Moshfeghian, M. (2012). Investigation of kinetics of methane hydrate formation during isobaric and isochoric processes in an agitated reactor. *Chem. Eng. Sci.* 76, 58–65. doi: 10.1016/j.ces.2012.04.016

Mu, L., Liu, B., Liu, H., Yang, Y., Sun, C., and Chen, G. (2012). A novel method to improve the gas storage capacity of ZIF-8. *J. Mater. Chem.* 22, 12246–12252. doi: 10.1039/c2jm31541f

Najibi, H., Chapoy, A., and Tohidi, B. (2008). Methane/natural gas storage and delivered capacity for activated carbons in dry and wet conditions. *Fuel* 87, 7–13. doi: 10.1016/j.fuel.2007.03.044

Nguyen, N. N., Nguyen, A. V., Steel, K. M., Dang, L. X., and Galib, M. (2017). Interfacial gas enrichment at hydrophobic surfaces and the origin of promotion of gas hydrate formation by hydrophobic solid particles. *J. Phys. Chem. C.* 121, 3830–3840. doi: 10.1021/acs.jpcc.6b07136

Park, S. S., Lee, S. B., and Kim, N. J. (2010). Effect of multi-walled carbon nanotubes on methane hydrate formation. *J. Ind. Eng. Chem.* 16, 551–555. doi: 10.1016/j.jiec.2010.03.023

Perrin, A., Celzard, A., Marêché, J. F., and Furdin, G. (2004). Improved methane storage capacities by sorption on wet active carbons. *Carbon* 42, 1249–1256. doi: 10.1016/j.carbon.2004.01.039

Perrin, A., Celzard, A., Maréché, J. F., and Furdin, G. (2003). Methane storage within dry and wet active carbons: a comparative study. *Energy Fuels* 17, 1283–1291. doi: 10.1021/ef030067i

Pirzadeh, P., and Kusalik, P. G. (2013). Molecular insights into clathrate hydrate nucleation at an ice-solution interface. *J. Am. Chem. Soc.* 135, 7278–7287. doi: 10.1021/ja400521e

Siangsai, A., Rangsunvigit, P., Kitiyanan, B., Kulprathipanja, S., and Linga, P. (2015). Investigation on the roles of activated carbon particle sizes on methane hydrate formation and dissociation. *Chem. Eng. Sci.* 126, 383–389. doi: 10.1016/j.ces.2014.12.047

Sloan, E. D. (2003). Fundamental principles and applications of natural gas hydrates. *Nature* 426, 353–359. doi: 10.1038/nature02135

Sloan, E. D., and Koh, C. A. (2007). *Clathrate Hydrates of Natural Gases, 3rd Edn*. Boca Raton, FL: Taylor and Francis. doi: 10.1201/9781420008494

Sun, Y., Wang, Y., Zhang, Y., Zhou, Y., and Zhou, L. (2007). CO_2 sorption in activated carbon in the presence of water. *Chem. Phys. Lett.* 437, 14–16. doi: 10.1016/j.cplett.2007.02.008

Urita, K., Shiga, Y., Fujimori, T., Iiyama, T., Hattori, Y., Kanoh, H., et al. (2011). Confinement in carbon nanospace-induced production of KI nanocrystals of high-pressure phase. *J. Am. Chem. Soc.* 133, 10344–10347. doi: 10.1021/ja202565r

Walsh, M. R., Koh, C. A., Sloan, D. E., Sum, A. K., and Wu, D. T. (2009). Microsecond simulations of spontaneous methane hydrate nucleation and growth. *Science* 5956, 1095–1098. doi: 10.1126/science.1174010

Yu, Y. S., Xu, C. G., and Li, X. S. (2018). Evaluation of CO_2 hydrate formation from mixture of graphite nanoparticle and sodium dodecyl benzene sulfonate. *J. Ind. Eng. Chem.* 59, 64–69. doi: 10.1016/j.jiec.2017.10.007

Yu, Y. S., Zhou, S. D., Li, X. S., and Wang, S. L. (2016). Effect of graphite nanoparticles on CO_2 hydrate phase equilibrium. *Fluid Phase Equilib.* 414, 23–28. doi: 10.1016/j.fluid.2015.12.054

Zhang, G., Sun, M., Liu, B., and Wang, F. (2020). Adsorption-induced two-way nanoconvection enhances nucleation and growth kinetics of methane hydrates in confined porespace. *Chem. Eng. J.* 396:125256. doi: 10.1016/j.cej.2020.125256

Zhang, X. X., Liu, H., Sun, C. Y., Xiao, P., Liu, B., Yang, L. Y., et al. (2014). Effect of water content on separation of CO_2/CH_4 with active carbon by adsorption-hydration hybrid method. *Sep. Purif. Technol.* 130, 132–140. doi: 10.1016/j.seppur.2014.04.028

Zhao, J., Zhao, Y., Liang, W., Song, S., and Gao, Q. (2018). Semi-clathrate hydrate process of methane in porous media-mesoporous materials of SBA-15. *Fuel* 220, 446–452. doi: 10.1016/j.fuel.2018.01.010

Zhao, W., Wang, L., Bai, J., Francisco, J. S., and Zeng, X. C. (2014). Spontaneous formation of one-dimensional hydrogen gas hydrate in carbon nanotubes. *J. Am. Chem. Soc.* 136, 10661–10668. doi: 10.1021/ja5041539

Zhong, D. L., Li, Z., Lu, Y. Y., Wang, J. L., Yan, J., and Qing, S. L. (2016). Investigation of CO_2 capture from a $CO_2 + CH_4$ gas mixture by gas hydrate formation in the fixed bed of a molecular sieve. *Ind. Eng. Chem. Res.* 55, 7973–7980. doi: 10.1021/acs.iecr.5b03989

Zhou, L., Liu, J., Su, W., Sun, Y., and Zhou, Y. (2010). Progress in studies of natural gas storage with wet adsorbents. *Energy Fuels* 24, 3789–3795. doi: 10.1021/ef100315t

Zhou, L., Liu, X., Sun, Y., Li, J., and Zhou, Y. (2005a). Methane sorption in ordered mesoporous silica SBA-15 in the presence of water. *J. Phys. Chem. B.* 20, 883–888. doi: 10.1021/jp0546002

Zhou, L., Sun, Y., and Zhou, Y. (2002). Enhancement of the methane storage on activated carbon by preadsorbed water. *AIChE J.* 48, 2412–2416. doi: 10.1002/aic.690481030

Zhou, S. D., Yu, Y. S., Zhao, M. M., Wang, S. L., and Zhang, G. Z. (2014). Effect of graphite nanoparticles on promoting CO_2 hydrate formation. *Energy Fuels* 28, 4694–4698. doi: 10.1021/ef5000886

Zhou, Y., Dai, M., Zhou, L., Sun, Y., and Su, W. (2004). Storage of methane on wet activated carbon: influence of pore size distribution. *Carbon* 42, 1855–1858. doi: 10.1016/j.carbon.2004.02.009

Zhou, Y., Wang, Y., Chen, H., and Zhou, L. (2005b). Methane storage in wet activated carbon: studies on the charging/discharging process. *Carbon* 43, 2007–2012. doi: 10.1016/j.carbon.2005.03.017

Conflict of Interest: The authors declare that the research was conducted in the absence of any commercial or financial relationships that could be construed as a potential conflict of interest.

frontiers in Chemistry

ORIGINAL RESEARCH
published: 14 October 2020
doi: 10.3389/fchem.2020.550862

Promoting the Insertion of Molecular Hydrogen in Tetrahydrofuran Hydrate With the Help of Acidic Additives

The Thuong Nguyen[1], *Claire Pétuya*[1,2], *David Talaga*[1] *and Arnaud Desmedt*[1]*

[1] Groupe Spectroscopie Moléculaire, ISM, UMR5255 CNRS—University, Bordeaux, France, [2] Jet Propulsion Laboratory, California Institute of Technology, Passadena, CA, United States

Among hydrogen storage materials, hydrogen hydrates have received a particular attention over the last decades. The pure hydrogen hydrate is generated only at extremely high-pressure (few thousands of bars) and the formation conditions are known to be softened by co-including guest molecules such as tetrahydrofuran (THF). Since this discovery, there have been considerable efforts to optimize the storage capacities in hydrates through the variability of the formation condition, of the cage occupancy, of the chemical composition or of the hydrate structure (ranging from clathrate to semi-clathrate). In addition to this issue, the hydrogen insertion mechanism plays also a crucial role not only at a fundamental level, but also in view of potential applications. This paper aims at studying the molecular hydrogen diffusion in the THF hydrate by *in-situ* confocal Raman microspectroscopy and imaging, and at investigating the impact of strong acid onto this diffusive process. This study represents the first report to shed light on hydrogen diffusion in acidic THF-H_2 hydrate. Integrating the present result with those from previous experimental investigations, it is shown that the hydrogen insertion in the THF hydrate is optimum for a pressure of *ca.* 55 bar at 270 K. Moreover, the co-inclusion of perchloric acid (with concentration as low as 1 acidic molecules per 136 water molecules) lead to promote the molecular hydrogen insertion within the hydrate structure. The hydrogen diffusion coefficient—measured at 270 K and 200 bar—is improved by a factor of 2 thanks to the acidic additive.

Keywords: strong acid, hydrogen storage, tetrahydrofuran, hydrates, clathrates, Raman spectroscopy

OPEN ACCESS

Edited by:
Amadeu K. Sum, Colorado School of Mines, United States

Reviewed by:
Kyuchul Shin, Kyungpook National University, South Korea
Ryo Ohmura, Keio University, Japan

***Correspondence:**
Arnaud Desmedt
arnaud.desmedt@u-bordeaux.fr

Specialty section:
This article was submitted to Physical Chemistry and Chemical Physics, a section of the journal Frontiers in Chemistry

Received: *10 April 2020*
Accepted: *03 September 2020*
Published: *14 October 2020*

Citation:
Nguyen TT, Pétuya C, Talaga D and Desmedt A (2020) Promoting the Insertion of Molecular Hydrogen in Tetrahydrofuran Hydrate With the Help of Acidic Additives. Front. Chem. 8:550862. doi: 10.3389/fchem.2020.550862

INTRODUCTION

Hydrogen is the most abundant element on Earth and is considered as a clean and potential energy vector in the future. H_2 storage and transportation are the subject of numerous studies. Among gas storage materials, hydrogen clathrate hydrates (also called hydrates) have received a particular attention over the last decades (Florusse et al., 2004; Veluswamy et al., 2014). Gas hydrates are crystalline inclusion compounds of hydrogen bonded water molecules forming cages encapsulating guest molecules (Sloan and Koh, 2008; Broseta et al., 2017; Ruffine et al., 2018). The pure H_2 clathrate hydrate is generated only at extremely high-pressure (few thousands of bars) and at low temperature (~240 K) (Dyadin et al., 1999; Mao et al., 2002). The hydrate is then formed with H_2 molecular species located in the small cages (SC) and in the large cages (LC) of the so-called sII hydrate (consisting of 16 SCs and 8 LCs) (Mao et al., 2002). To enable the storage of H_2 under softer conditions (typically 50 bars and 280 K), the method consists in co-including H_2 molecules

with a second guest such as tetrahydrofuran (THF), to form a mixed THF-H_2 sII hydrate (Florusse et al., 2004; Lee et al., 2005). However, THF molecules occupy the LC and H_2 molecules are only in the SC, which leads to low hydrogen storage (<2 wt%) (Strobel et al., 2006; Mulder et al., 2008) and limits the potential applications (Nakayama et al., 2010). Since this discovery, there have been considerable efforts to optimize the storage capacities of H_2 in clathrate hydrates through the variability of the formation condition, of the cage occupancy, of the chemical composition (by changing the promoter and its concentration) or of the cage structure (from clathrate to semi-clathrate) (Veluswamy et al., 2014).

Beyond the problematic of H_2 storage capacity for potential applications, the H_2 insertion mechanism plays is of fundamental interest. When H_2 gas pressure is applied onto a powdered THF hydrate, the formation mechanism involves two steps: hydrogen adsorption onto the clathrate particle surface, followed by subsequent diffusion of hydrogen into the clathrate hydrate particle. The inter-cage diffusion represents the limiting step (timescale of the order of days), involving high activation energy (78.7 kJ/mol) (Nagai et al., 2008), confirmed by electronic structure calculations (Alavi and Ripmeester, 2007). To improve the storage capability of H_2 in hydrates, one issue concerns the possibility of modifying the water cage relaxation. The dynamic properties of various hydrates have been investigated and water molecules reorients on a millisecond timescale (Sloan and Koh, 2008). Recently, it has been shown that water molecules relax on a nanosecond timescale in strong acid clathrate hydrates (Desmedt et al., 2004, 2013; Bedouret et al., 2014). Moreover, THF clathrate hydrate may be prepared by co-including strong acid molecules (Desmedt et al., 2015). Such chemical modification has an impact onto the lattice dynamics of the cages and on the melting points of the hydrates (Desmedt et al., 2015). However, to the best of our knowledge, no studies have been performed until now to investigate the H_2 storage in such THF clathrate hydrates co-including strong acid species.

The description of the H_2 insertion mechanism outlines the key role played by dynamical processes met in clathrate hydrates (Desmedt et al., 2012, 2017). At atmospheric pressure, only intra-cage diffusion of H_2 is experimentally observed in the THF-H_2 hydrate stability region (i.e., below *ca.* 270 K) (Pefoute et al., 2012). At higher pressure (typically several tens of bars), studies of molecular hydrogen diffusion into THF hydrates have been performed by means of NMR method (Okuchi et al., 2007), *in situ* neutron diffraction (Mulder et al., 2008), volumetric measurements (Nagai et al., 2008), theoretical calculations (Alavi and Ripmeester, 2007) and molecular dynamics simulations (Cao et al., 2013). These measurements, performed in various P-T thermodynamics conditions, lead to diffusion coefficient ranging from *ca.* 10^{-6} cm^2/s to *ca.* 10^{-12} cm^2/s. These results outline the importance of using an experimental method allowing the direct investigation of the spatial and time characteristics of the H_2 diffusion within the hydrate. In this issue, confocal Raman microspectroscopy is a non-destructive approach and is particularly adapted for *in situ* investigation of transport process in nanoporous systems (Marti-Rujas et al., 2004, 2006, 2007). This vibrational technique is an interesting label-free tool to access the molecular composition, the molecular selectivity, the structural and dynamical information in gas hydrates (Chazallon et al., 2017; Petuya et al., 2017, 2018a,b; Petuya and Desmedt, 2019). Raman spectroscopy has been performed to study the hydrogen storage in hydrates (Florusse et al., 2004; Ogata et al., 2008; Strobel et al., 2009; Grim et al., 2012) and it has been shown that THF hydrates may act as a molecular sieving for hydrogen-containing gas mixtures (Zhong et al., 2017). This paper aims at studying the H_2 diffusion mechanism in the THF clathrate hydrate by *in situ* confocal Raman microspectroscopy and imaging, and at investigating the impact of strong acid onto this diffusive process at 200 bar pressure. To address this issue, we use two different sII hydrogen hydrate formed with THF promoter: THF-H_2 hydrate (non-acidic) and the THF-$HClO_4$-H_2 hydrate (acidic).

EXPERIMENTAL DETAILS

Samples

Two solutions were prepared with the following molar ratio $8THF{\cdot}136H_2O$ (melting at 277 K) and $7THF^{-}1HClO_4{\cdot}136H_2O$ (melting at 271 K) using ultra-pure water (Milli-Q quality) and commercially available chemicals (70% $HClO_4$ aqueous solution and 99.9% THF from Sigma-Aldrich). They were transferred under inert atmosphere in the lab-made high-pressure optical cell used for the Raman spectroscopic analysis. According to a procedure previously published (Desmedt et al., 2015), the hydrates have been formed under stirring conditions by cooling the sample temperature to 270 K and maintaining this temperature for 24 h with the help of a modified cryogenic stage (Linkam Scientific Instruments Ltd., UK). Once the hydrate is formed, hydrogen gas (99.9999% Air Liquide) was then applied at constant pressure (200 bar) with a PM High Pressure pump (Top Industrie, Vaux-le-Penil, France) which contains 100 cm^3 of gas.

Raman Scattering and Imaging

Raman data were collected with a Labram microspectrometer (Horiba Jobin Yvon, Villeneuve d'Ascq, France) and using a 514 nm laser source (10 mW power at the sample). A 50X objective (NA = 0.45, Olympus) permitted to focus the incident laser beam and to collect the Raman scattering. The Raman scattering was dispersed with a holographic grating of 1,800 g/mm and analyzed with a Peltier-cooled CCD detector (Andor, Belfast, UK), which permitted to measure the Raman spectra with a spectral resolution of 1 cm^{-1}. The data was collected on a spectral range from 2,700 to 4,300 cm^{-1} to monitor the hydrogen stretching modes. To probe the H_2 diffusion into the preformed hydrate as a function of time, micro-Raman spectra and imaging were collected *in situ* under the 200 bar H_2 pressure at 270 K in the hydrate stability zone (Hashimoto et al., 2007). The measurement has been started simultaneously with the application of H_2 pressure (corresponding to time $t = 0$ h in the following). For recording the spectral images, a motorized stage was used to map the sample in a point-by-point mode using a 20 μm step size in the two XZ plane perpendicular to the gas-hydrate interface contained in the XY plane (**Figure 1**). For each

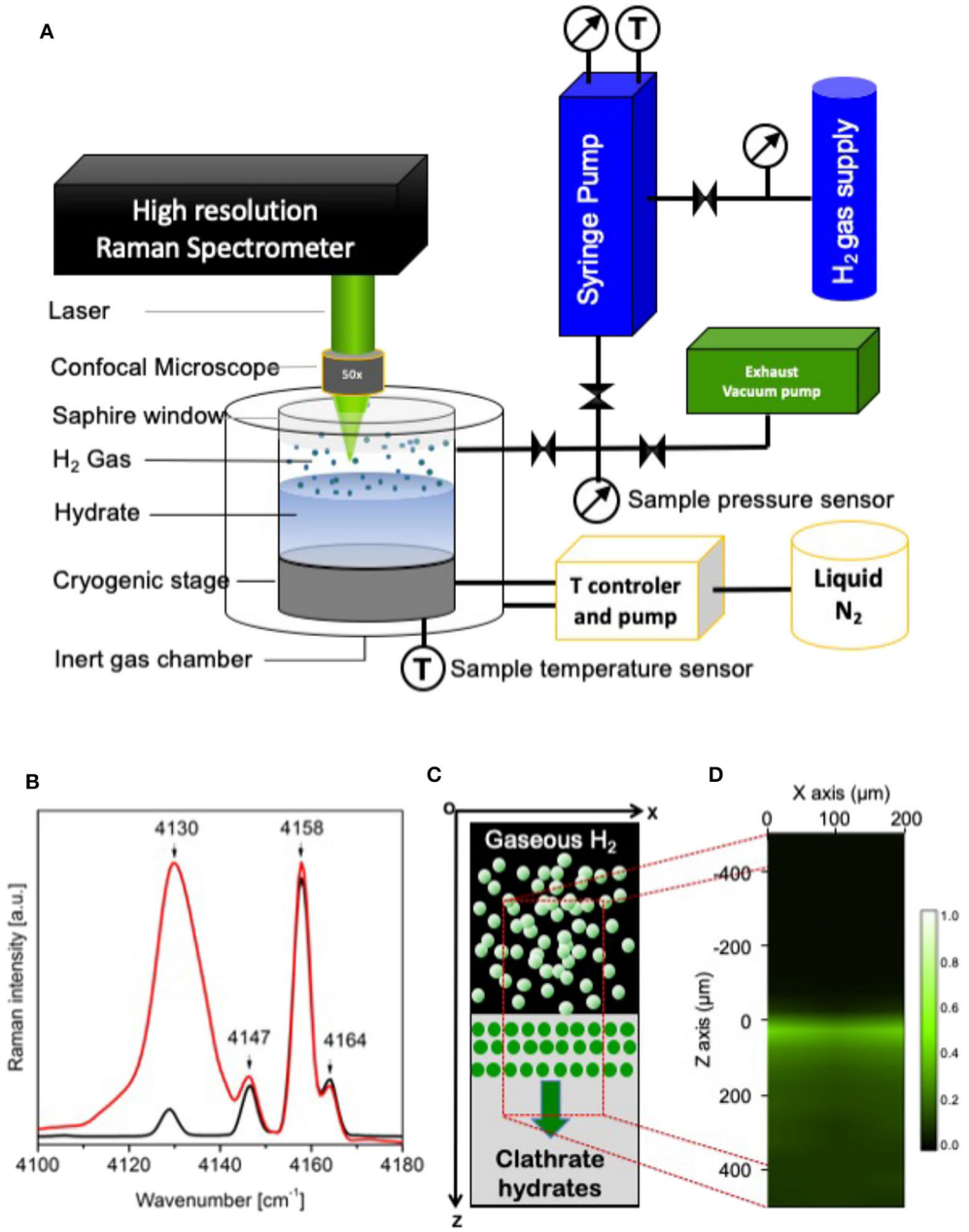

FIGURE 1 | (A) Schematic representation of the experimental set-up used to monitor the insertion of molecular hydrogen within the THF hydrate. **(B)** Raman spectra of H_2 gaseous (black, **A**) and of confined H_2 in THF hydrate (red, **A**) at 270 K and 200 bar; **(C)** Schematic illustration of experimental measurement. The microraman imaged region is shown with red dashed lines; **(D)** Spectral image constructed using the integrated intensities of Raman bands at 4,130 cm^{-1} (encapsulated H_2). Green color indicates inserted H_2 in the hydrate and black color indicates no H_2 inserted.

sample, an area of about 200 × 1,200 μm^2 from the H_2/hydrate interface to 1,000 μm depths in the hydrate by Raman micro-imaging. In the following, $Z = 0\,\mu m$ corresponds to the gas-hydrate interface. Raman intensity depth profiles of inserted H_2 were corrected from the refraction by using standard procedure (Everall, 2000; Desmedt et al., 2007) with a refraction index $n = 1{,}33$ (Sloan and Koh, 2008) for the hydrate.

RESULTS AND DISCUSSION

In the present investigation, two hydrates have been considered: the THF hydrate (formed with a THF·17H_2O solution) and the mixed THF-$HClO_4$ hydrate (formed with a 0.875THF-0.125$HClO_4$·17H_2O solution). In these sII hydrates, the SCs are empty to welcome H_2 molecules, the THF molecules occupy the

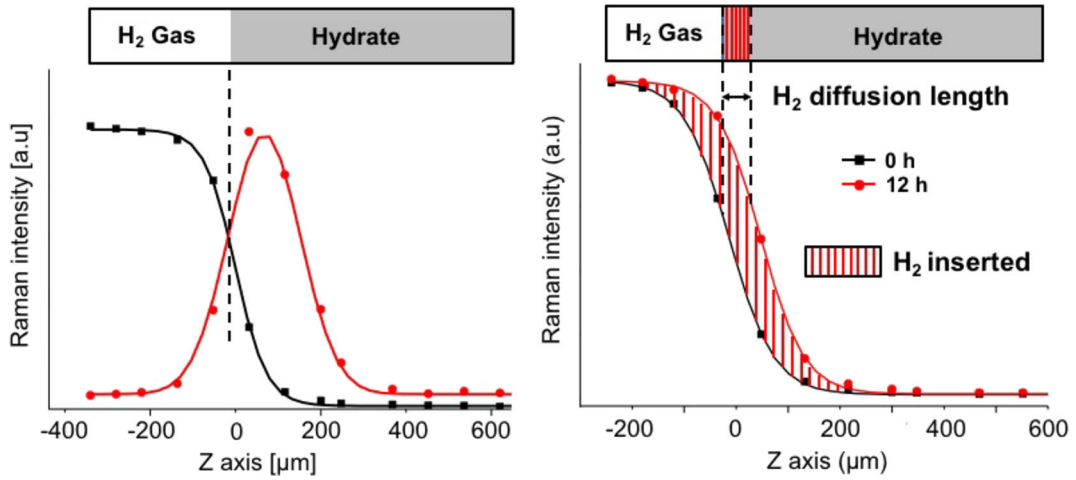

FIGURE 2 | Left: H_2 (black) and OH (red) Raman integrated intensity profiles (normalized) of the THF-$HClO_4$-H_2 hydrate at t = 0 h, 200 bar and 270 K. Negative Z values corresponds at the gaseous phase within the high-pressure optical cell, while positive Z values corresponds to the hydrate phase. **Right**: H_2 Raman intensity profiles of the THF-$HClO_4$-H_2 hydrate at 0 h (black) and after 12 h (red) of 200 bar H_2 pressure.

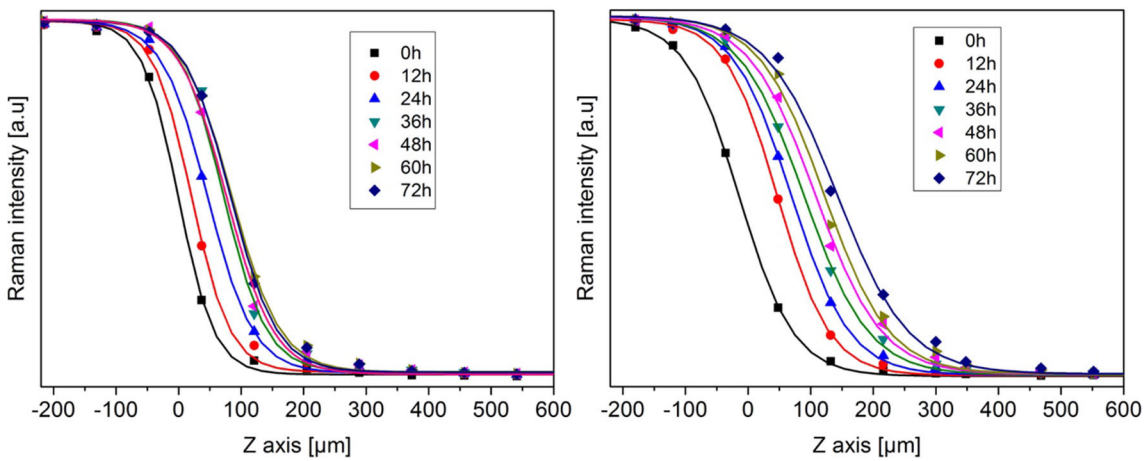

FIGURE 3 | Time evolution of the H_2 Raman intensity profiles for THF-H_2 **(left)** and THF-$HClO_4$-H_2 **(right)** hydrates obtained at 270 K and 200 bar. The continuous lines are the sigmoidal functions fitted on the experimental points (see text for details).

LC and the acidic additive $HClO_4$ is inserted within the LC by replacing one THF per unit cell in average (Desmedt et al., 2015). The insertion of molecular hydrogen within these two preformed hydrates has been probed thanks to real-time Raman imaging. An example of the spectral region corresponding to the gaseous H_2 and confined H_2 signatures is shown in **Figure 1A** for the THF-H_2 hydrate formed within the lab-made high-pressure optical cell after 1 day at 200 bars and 270 K. The rotation-vibration coupled bands of gaseous H_2 are observed at 4,130, 4,147, 4,155, and 4,164 cm^{-1}. In the case of the THF-H_2 hydrate, the band at 4,130 cm^{-1} is assigned to the Raman signal of H_2 confined in the sII hydrate SCs (Ogata et al., 2008; Strobel et al., 2009; Grim et al., 2012). To monitor the insertion of hydrogen within the hydrate, Raman imaging has been performed in the plane perpendicular to the gas/hydrate interface (see **Figure 1B**). An example of visualization of the H_2 molecules confined in the hydrate is shown in **Figure 1C** through the Raman mapping of the ratio of the band intensity at 4,130 cm^{-1} and of the one at 4,155 cm^{-1}. The Raman intensity being proportional to the encapsulated species concentration (Zhong et al., 2017), such a Raman image is a direct signature of the spatial H_2 distribution within the preformed THF hydrate; after 1 day of pressurization, one can observe that H_2 has mainly be inserted within few tens of micrometers below the hydrate surface. In order to spatially analyse the extension of H_2 insertion, one needs to locate the gas/hydrate interface at a micrometric scale. In this purpose, the intensity profiles of the H_2 vibron and of the OH stretching modes have been measured with the help of

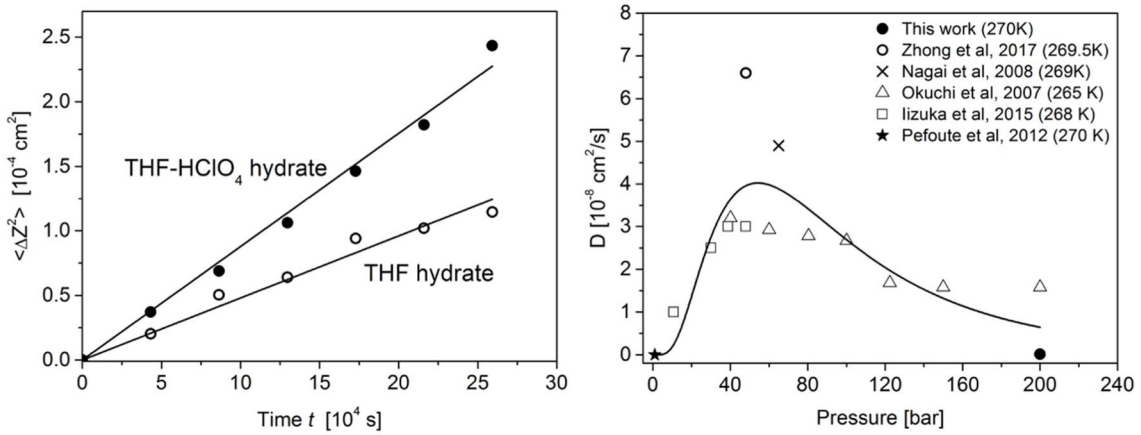

FIGURE 4 | Left: H_2 diffusion length of the THF-$HClO_4$-H_2 (filled symbols) and THF-H_2 (open symbols) hydrates measured at 270 K and 200 bar. The lines represent the fitted Fick model (see text for details). **Right**: Pressure dependence of the H_2 diffusion coefficient integrating data from various experimental investigations in the 265–270 K region (Okuchi et al., 2007; Nagai et al., 2008; Pefoute et al., 2012; Iizuka et al., 2015; Zhong et al., 2017). The line represents a guide-to-the-eyes showing that the diffusion coefficient goes through a maximum at *ca.* 55 bar.

the projection of the acquired Raman spectra in the XZ plane along the Z axis (see **Figure 1B**). An example of such averaged profiles is shown in **Figure 2** (left) for the measurement at initial stage ($t = 0$ h) of H_2 pressurization at 200 bar and at T = 270 K. A pseudo-Voigt function has been used to reproduce the experimental data of the OH integrated intensity profile and the H_2 intensity profile has been fitted with a sigmoidal function. The fitted functions reproduce with a good agreement the experimental data (the residual error between experimental and modeled curves reached a value of 10^{-3}). The gas/hydrate interface is then clearly identified at the intersection of these two curves: it corresponds to the Z coordinate of the inflection point of the H_2 sigmoidal curve. This procedure allows to accurately determine the Z position of the gas/hydrate interface and is set as the reference distance $Z = 0\,\mu$m. Moreover, the H_2 vibron intensity profile can be used as a signature of the H_2 diffusion front position as a function of time. This is shown in **Figure 2** (right): the H_2 intensity profiles of THF-$HClO_4$-H_2 hydrate after 12 h of pressurization is clearly Z-shifted with respect to the profile at initial time $t = 0$ h. This Z difference of the H_2 diffusion front is the signature of the insertion of H_2 molecule within the hydrate sample; it is defined as the mean H_2 diffusion length, $\Delta Z\,(t)$:

$$\left\langle \Delta Z(t) \right\rangle = Z\,(t) - Z\,(0) \tag{1}$$

where $Z\,(t)$ corresponds to the inflection point of the H_2 sigmoidal curve at time t. To subsequently analyse the time-evolution of the H_2 insertion, such H_2 Raman intensity profiles have been recorded every 12 h over a period of 3 days. In order to evaluate the impact of the strong acid $HClO_4$ additive, these measurements have been performed onto the preformed THF hydrate and onto the preformed THF-$HClO_4$ hydrate, both pressurized with H_2 gas at 270 K and 200 bar. The time evolution of the H_2 intensity profiles is shown in **Figure 3** for the THF-$HClO_4$-H_2 hydrate and for the THF-H_2 hydrate. It can be observed a marked difference between these time evolutions: the H_2 diffusion front extend over a wider range in the case of the THF-$HClO_4$ hydrates compared to the case of the THF hydrate, i.e., without acidic additives. In order to quantitatively analyse the time evolution of the H_2 diffusion front within the hydrates, each intensity profile has been fitted by using the sigmoidal function as previous described, allowing to measure the position of the H_2 diffusion front as a function of time. Such procedure allows to measure the H_2 diffusion lengths (Equation 1) as a function of time. Their mean-squared values $\left\langle \Delta Z(t)^2 \right\rangle$ are reported in **Figure 4**. These curves show clearly the improvement of the H_2 insertion when acidic additive are included in the THF hydrate: the values are higher for the THF-$HClO_4$ hydrate than for the THF hydrate.

Furthermore, such curves provide the opportunity to investigate the H_2 insertion mechanism. Such diffusive mechanism may include various elementary processes including the inter-cage diffusion and possible contributions associated with grain boundaries, chemical and structural defects. Let first consider two principal diffusive models by analogy with nanoporous systems (Marti-Rujas et al., 2007): conventional diffusion or single-file-like diffusion. The conventional diffusion corresponds to the Fick law for which the mean-squared H_2 diffusion length is given by the Einstein diffusion model in a three-dimensional system:

$$\left\langle \Delta Z(t)^2 \right\rangle = 6Dt \tag{2}$$

where D is the H_2 diffusion coefficient. The Fick behavior may reproduce not only the inter-cage diffusion, but also the diffusion associated with grain boundaries and structural defects. The single-file-like diffusive model may be considered for the H_2 inter-cage diffusion. Indeed, the H_2 molecule dimension is

comparable to the diameter of the polygonal faces of the water cages. In such a model, H_2 molecule diffusion within a water cage may proceed under the condition that there is a vacant guest site in the neighboring cage—unlike in the case of Fick behavior for which H_2 molecules can overtake each other in the cages. This phenomenon involves correlations between the H_2 displacements within the hydrate and thus the time-dependence of $\left\langle \Delta Z(t)^2 \right\rangle$ differs from the Fick diffusion:

$$\left\langle \Delta Z(t)^2 \right\rangle = 6Mt^{1/2} \quad (3)$$

where M correspond to the H_2 mobility in the three-dimensional hydrate system. The time dependence of $\left\langle \Delta Z(t)^2 \right\rangle$ exhibit a clear linear behavior (it has not been possible to reproduce the experimental data with the single-file-like model). It thus implies that H_2 molecules can overtake each other in a cage and mainly follows a fick behavior. such a diffusive behavior is in full agreement with NMR (Okuchi et al., 2007), *in situ* neutron diffraction (Mulder et al., 2008), volumetric measurements (Nagai et al., 2008), Raman (Zhong et al., 2017), and molecular dynamics (Cao et al., 2013). The Fick law given by Equation (2) have been fitted to the experimental data with an excellent agreement (see **Figure 4**-Left). The fitted diffusion coefficients are of $7.98 \pm 0.03\ 10^{-11}$ cm^2/s for the THF hydrate and $1.46 \pm 0.03\ 10^{-10}$ cm^2/s for the THF-$HClO_4$ hydrate at 270 K and 200 bar. The obtained diffusion coefficient for the H_2 insertion in the THF-H_2 hydrate is within the broad range of values obtained by various experimental methods and reported in **Figure 4**-Right. The present study confirms the trend of an optimum pressure for promoting the hydrogen diffusion at *ca.* 55 bar. Such a behavior reflects a trend regarding the transport of hydrogen molecules between the cages: the inter-cage diffusion is slower when a large fraction of the small cage is already filled, or even doubly filled with H_2 as reported from Molecular Dynamics simulations (Cao et al., 2013). Once the small cage of the sII THF hydrate are filled, structural or chemical defects and grain boundaries should play a key-role for insuring the Fickian H_2 diffusion through and within the sII THF hydrate. Indeed, the behavior observed with the THF-$HClO_4$ hydrate confirms the importance of such defects: a clear quantitative enhancement of the H_2 diffusion in the THF hydrate is measured thanks to the co-inclusion of $HClO_4$ in the sII structure (**Figure 4**-Left). As reported in previous studies (Desmedt et al., 2015), the inclusion of $HClO_4$ into the THF hydrate lead to generate perchlorate anions confined in the LC and acidic protons delocalized within the water cage structure (this delocalization is at the origin of the super-protonic conductivity met in strong acid hydrates; Desmedt et al., 2004, 2013). In such a case, the cages are constituted not only of water molecules, but also of hydronium ions. The energy barrier related to H_2 molecules diffusion through the water cage being higher for SC than for LC (Okuchi et al., 2007), the inclusion of such ionic defects in the hydrate lead to modify the flexibility of the cage, as reported from Raman measurements of the water cage phonons (Desmedt et al., 2015). This increased flexibility of the water cage—especially of the SCs welcoming the H_2—may lead to decrease the energy barrier required for an H_2 molecule to cross the faces of the water cage and thus to facilitate the inter-cage diffusion, as reflected by the enhanced diffusion coefficient measured in the THF-$HClO_4$.

CONCLUSION

The present investigation represents the first report to shed light on the impact of ionic defects onto the hydrogen insertion within hydrate. This study has been realized by comparing the H_2 diffusion within the THF hydrate and the mixed THF-$HClO_4$ hydrate, both being sII structure. Raman confocal microspectroscopy and imaging has been a powerful tool. It yields the measurement of the H_2 Fickian diffusion coefficients within the two hydrates at 270 K and 200 bar: $7.98 \pm 0.03\ 10^{-11}$ cm^2/s for the THF hydrate and $1.46 \pm 0.03\ 10^{-10}$ cm^2/s for the THF-$HClO_4$ hydrate. In the case of the THF hydrate, it is shown that the H_2 diffusion within the hydrate is optimum for a pressure of *ca.* 55 bar by compiling this result with those from the literature. Moreover, this investigation clearly shows the enhancement of the H_2 insertion within the THF hydrate thanks to the co-inclusion of acidic additive: it acts as a "flexibilizer" of the water cage through the addition of chemical water H-bond defects (Desmedt et al., 2015) promoting the H_2 inter-cage diffusion. Such results are particularly exciting and promising for applications in storage of hydrogen and open new routes for developing efficient hydrate-based hydrogen storage materials with new type of promoter.

DATA AVAILABILITY STATEMENT

The original contributions presented in the study are included in the article/supplementary material, further inquiries can be directed to the corresponding author/s.

AUTHOR CONTRIBUTIONS

TN and CP have performed the sample preparation, the Raman scattering experiments, and data acquisition. DT has contributed to the Raman spectrometer configuration and data management. TN and AD has analyzed, interpreted the data, and has written the manuscript. All authors contributed to the article and approved the submitted version.

FUNDING

This work falls in the frame of the project ANR 2011-JS08-002-01, funded by the French ANR Agence Nationale de la Recherche. The Raman scattering experiments have been performed on equipment of the Vibrational Spectroscopy and Imaging platform (SIV at ISM), funded by the Conseil Régional de Nouvelle Aquitaine and Europe (FEDER programme).

REFERENCES

Alavi, S., and Ripmeester, J. A. (2007). Hydrogen-gas migration through clathrate hydrate cages. *Angew. Chem. Int. Ed.* 46, 6102–6105. doi: 10.1002/ange.200790242

Bedouret, L., Judeinstein, P., Ollivier, J., Combet, J., and Desmedt, A. (2014). Proton diffusion in the hexafluorophosphoric acid clathrate hydrate. *J. Phys. Chem. B* 118, 13357–13364. doi: 10.1021/jp504128m

Broseta, D., Ruffine, L., and Desmedt, A. (2017). *Gas Hydrates 1: Fundamentals, Characterization and Modeling*. London: Wiley–ISTE.

Cao, H., English, N. J., and MacElroy, J. M. D. (2013). Diffusive hydrogen intercage migration in hydrogen and hydrogen-tetrahydrofuran clathrate hydrates. *J. Chem. Phys*. 138:094507. doi: 10.1063/1.4793468

Chazallon, B., Noble, J., and Desmedt, A. (2017). "Spectroscopy of gas hydrates: from fundamental aspects to chemical engineering, geophysical and astrophysics applications," in *Gas Hydrates 1: Fundamentals, Characterization and Modeling*, eds D. Broseta, L. Ruffine, and A. Desmedt (London, UK: Wiley–ISTE), 63–112.

Desmedt, A., Bedouret, L., Ollivier, J., and Petuya, C. (2017). "Neutron scattering of clathrate and semi-clathrate hydrates," in *Gas Hydrates 1: Fundamentals, Characterization and Modeling*, eds D. Broseta, L. Ruffine, and A. Desmedt (London, UK: Wiley–ISTE), 1–62. doi: 10.1002/9781119332688.ch1

Desmedt, A., Bedouret, L., Pefoute, E., Pouvreau, M., Say-Liang-Fat, S., and Alvarez, M. (2012). Energy landscape of clathrate hydrates. *Eur. Phys. J. Special Topics* 213, 103–127. doi: 10.1140/epjst/e2012-01666-3

Desmedt, A., Lechner, R. E., Lassègues, J. C., Guillaume, F., Cavagnat, D., and Grondin, J. (2013). Hydronium dynamics in the perchloric acid clathrate hydrate. *Solid State Ion.* 252, 19–25. doi: 10.1016/j.ssi.2013.06.004

Desmedt, A., Martin-Gondre, L., Nguyen, T. T., Petuya, C., Barandiaran, L., Babot, O., et al. (2015). Modifying the flexibility of water cages by co-including acidic species within clathrate hydrate. *J. Phys. Chem. C* 119, 8904–8911. doi: 10.1021/jp511826b

Desmedt, A., Stallmach, F., Lechner, R. E., Cavagnat, D., Lassègues, J. C., Guillaume, F., et al. (2004). Proton dynamics in the perchloric acid clathrate hydrate $HClO_4$-5.5H_2O. *J. Chem. Phys*. 121, 11916–11926 doi: 10.1063/1.1819863

Desmedt, A., Talaga, D., and Bruneel, J. L. (2007). Enhancement of the raman scattering signal due to a nanolens effect. *Appl. Spectroscop*. 61, 621–623. doi: 10.1366/000370207781269837

Dyadin, Y. A., Larionov, E. G., Aladko, E. Y., Manakov, A. Y., Zhurko, F. V., Mikina, T. V., et al. (1999). Clathrate formation in water-noble gas (Hydrogen) systems at high pressures. *J. Struct. Chem*. 40, 790–795. doi: 10.1007/BF02903454

Everall, N. J. (2000). Modeling and measuring the effect of refraction on the depth resolution of confocal raman microscopy. *Appl. Spectrosc*. 54:773. doi: 10.1366/0003702001950382

Florusse, L. J., Peters, C. J., Schoonman, J., Hester, K. C., Koh, C., Dec, S. F., et al. (2004). Stable low-pressure hydrogen clusters stored in a binary clathrate hydrate. *Science* 306:469–471. doi: 10.1126/science.1102076

Grim, R. G., Kerkar, P. B., Shebowich, M., Arias, M., Sloan, E. D., Koh, C. A., et al. (2012). synthesis and characterization of sI clathrate hydrates containing hydrogen. *J. Phys. Chem. C* 116, 18557–18563. doi: 10.1021/jp307409s

Hashimoto, S., Sugahara, T., Sato, H., and Ohgaki, K. (2007). Thermodynamic stability of H_2 + tetrahydrofuran mixed gas hydrate in nonstoichiometric aqueous solutions. *J. Chem. Eng. Data* 52, 517–520. doi: 10.1021/je06 0436f

Iizuka, A., Hayashi, S., Tajima, H., Kiyono, F., Yanagisawa, Y., and Yamasaki, A. (2015). Gas separation using tetrahydrofuran clathrate hydrate crystals based on the molecular sieving effect. *Sep. Purif. Technol*. 139, 70–77. doi: 10.1016/j.seppur.2014.10.023

Lee, H., Lee, J., Kim, D. Y., Park, J., Seo, Y.-T., Zeng, H., et al. (2005). Tuning clathrate hydrates for hydrogen storage. *Nature* 434, 743–746. doi: 10.1038/nature03457

Mao, W. L., Mao, H. K., Goncharov, A. F., Struzhkin, V. V., Guo, Q. Z., Hu, J. Z., et al. (2002). Hydrogen clusters in clathrate hydrate. *Science* 297, 2247–2249. doi: 10.1126/science.1075394

Marti-Rujas, J., Desmedt, A., Harris, K. D. M., and Guillaume, F. (2004). Direct time-resolved and spatially resolved monitoring of molecular transport in a crystalline nanochannel system. *J. Am. Chem. Soc*. 126, 11124–11125. doi: 10.1021/ja040117d

Marti-Rujas, J., Desmedt, A., Harris, K. D. M., and Guillaume, F. (2007). Kinetics of molecular transport in a nanoporous crystal studied by confocal raman microspectrometry: single-file diffusion in a densely filled tunnel. *J. Phys. Chem. B. (Letter)* 111, 12339–12344. doi: 10.1021/jp076532k

Marti-Rujas, J., Harris, K. D. M., Desmedt, A., and Guillaume, F. (2006). Significant conformational changes associated with molecular transport in a crystalline solid. *J. Phys. Chem. B* 110, 10708–10713. doi: 10.1021/jp060738o

Mulder, F. M., Wagemaker, M., van Eijck, L., and Kearley, G. J. (2008). Hydrogen in porous tetrahydrofuran clathrate hydrate. *Chem. Phys. Chem*. 9, 1331–1337. doi: 10.1002/cphc.200700833

Nagai, Y., Yoshioka, H., Ota, M., Sato, Y., Inomata, H., Smith, J. R., et al. (2008). Binary hydrogen-tetrahydrofuran clathrate hydrate formation kinetics and models. *AiChE J*. 54, 3007–3016. doi: 10.1002/aic.11587

Nakayama, T., Tomura, S., Ozaki, M., and Mori, H. M. (2010). Engineering investigation of hydrogen storage in the form of clathrate hydrates: conceptual design of hydrate production plants. *Energy Fuels* 24, 2576–2588. doi: 10.1021/ef100039a

Ogata, K., Hashimoto, S., Sugahara, T., Moritoki, M., Sato, H., and Ohgaki, K. (2008). Storage capacity of hydrogen in tetrahydrofuran hydrate. *Chem. Eng. Sci*. 63, 5714–5718. doi: 10.1016/j.ces.2008.08.018

Okuchi, T., Moudrakovski, I. L., and Ripmeester, J. A. (2007). Efficient storage of hydrogen fuel into leaky cages of clathrate hydrate. *Appl. Phys. Lett*. 91:171903. doi: 10.1063/1.2802041

Pefoute, E., Kemner, E., Soetens, J. C., Russina, M., and Desmedt, A. (2012). Diffusive motions of molecular hydrogen confined in THF clathrate hydrate. *J. Phys. Chem. C* 116, 16823–16829. doi: 10.1021/jp3008656

Petuya, C., Damay, F., Chazallon, B., Bruneel, J. L., and Desmedt, A. (2018a). Guest partitioning and metastability of the nitrogen gas hydrate. *J. Phys. Chem. C* 122, 566–573. doi: 10.1021/acs.jpcc.7b10151

Petuya, C., Damay, F., Desplanche, S., Talaga, D., and Desmedt, A. (2018b). Selective trapping of CO_2 gas and cage occupancy in CO_2-N_2 and CO_2-CO mixed gas hydrates. *Chem. Comm*. 54, 4290–4293. doi: 10.1039/C8CC00538A

Petuya, C., Damay, F., Talaga, D., and Desmedt, A. (2017). Guest partitioning in carbon monoxide hydrate by raman spectroscopy. *J. Phys. Chem. C* 121, 13798–13802. doi: 10.1021/acs.jpcc.7b04947

Petuya, C., and Desmedt, A. (2019). Revealing CO-preferential encapsulation in the mixed CO-N_2 clathrate hydrate. *J. Phys. Chem. C* 123, 4871–4878. doi: 10.1021/acs.jpcc.8b11680

Ruffine, L., Broseta, D., and Desmedt, A. (2018). *Gas Hydrates 2: Geoscience Issues and Potential Industrial Applications*. London: Wiley–ISTE.

Sloan, E. D., and Koh, C. A. (2008). *Clathrate Hydrates of Natural Gases*. Boca Raton, FL: CRC Press.

Strobel, T. A., Sloan, E. D., and Koh, C. A. (2009). Raman spectroscopic studies of hydrogen clathrate hydrates. *J. Chem. Phys*. 130:014506. doi: 10.1063/1.3046678

Strobel, T. A., Taylor, C. J., Hester, K. C., Dec, S. F., Koh, C. A., Miller, K. T., et al. (2006). Molecular hydrogen occupancy in binary THF–H_2 clathrate hydrates by high resolution neutron diffraction. *J. Phys. Chem. B* 110, 14024–14027. doi: 10.1021/jp062139n

Veluswamy, H. P., Kumar, R., and Linga, P. (2014). Hydrogen storage in clathrate hydrates: current state of the art and future directions. *Appl. Energ.* 122, 112–132. doi: 10.1016/j.apenergy.2014.01.063

Zhong, J. R., Chen, L. T., Liu, T. C., Zeng, X. Y., Sun, Y. F., Sun, C. Y., et al. (2017). Sieving of hydrogen-containing gas mixtures with tetrahydrofuran hydrate. *J. Phys. Chem. C* 121, 27822–27829. doi: 10.1021/acs.jpcc.7b08945

Conflict of Interest: The authors declare that the research was conducted in the absence of any commercial or financial relationships that could be construed as a potential conflict of interest.

Advantages of publishing in Frontiers

OPEN ACCESS
Articles are free to read for greatest visibility and readership

FAST PUBLICATION
Around 90 days from submission to decision

HIGH QUALITY PEER-REVIEW
Rigorous, collaborative, and constructive peer-review

TRANSPARENT PEER-REVIEW
Editors and reviewers acknowledged by name on published articles

Frontiers
Avenue du Tribunal-Fédéral 34
1005 Lausanne | Switzerland

Visit us: www.frontiersin.org
Contact us: frontiersin.org/about/contact

REPRODUCIBILITY OF RESEARCH
Support open data and methods to enhance research reproducibility

DIGITAL PUBLISHING
Articles designed for optimal readership across devices

FOLLOW US
@frontiersin

IMPACT METRICS
Advanced article metrics track visibility across digital media

EXTENSIVE PROMOTION
Marketing and promotion of impactful research

LOOP RESEARCH NETWORK
Our network increases your article's readership